

Plasma-based Electroacoustic Actuator for Broadband Sound Absorption

Présentée le 23 septembre 2022

Faculté des sciences et techniques de l'ingénieur
Laboratoire de traitement des signaux 2
Programme doctoral en génie électrique

pour l'obtention du grade de Docteur ès Sciences

par

Stanislav SERGEEV

Acceptée sur proposition du jury

Prof. O. Martin, président du jury
Prof. P. Vanderghenst, Dr H. Lissek, directeurs de thèse
Dr Ph. Béquin, rapporteur
Dr J. Hargreaves, rapporteur
Prof. R. Fleury, rapporteur

Главное в физике — это умение пренебрегать.

Lev Landau

To my family and friends...

Acknowledgements

This paragraph refers to the ones without whose guidance and support this thesis would not have been possible.

First of all, I would like to express my heartfelt gratitude to Dr Hervé Lissek, my main thesis supervisor. It must be said that you invested in a risky research topic which finally led to a completely new yet successful research direction for the laboratory. Thank you for inviting me to work on this fascinating project and guiding me along this thorny path. I appreciate your positive attitude and cordial relationship. I strongly believe that at some point our work will undermine the calmness of electroacoustic society and bring fresh air to active metamaterials research. I would also like to thank Prof. Pierre Vanderghelynst for providing me with the opportunity to carry out my doctoral studies as a part of LTS2 laboratory.

I would like to acknowledge the jury members of my thesis defence for reviewing the thesis. Merci to Dr Philippe Béquin for his own work, which influenced my research, valuable comments and suggestions. Big thanks to Dr Jonathan Hargreaves and Prof. Romain Fleury for the constructive criticism, insightful discussions, and bright ideas. Special thanks to Prof. Olivier Martin for presiding over the committee.

I am very thankful to my numerous colleagues from the ARTEM project for letting us develop a plasma-based noise reduction solution within its framework. I thank European Commission which has financially supported my research.

I express my profound gratitude to my colleagues from Swiss Plasma Center for introducing me to experimentation with plasmas. My sincere thanks to Prof. Ivo Furno and Dr Alan Howling for engagement in my research, for providing the instrumentation for experimental work, and for multiple discussions. Thank you, Dr Gennady Plyushchev, for your support and incredible engineering skills in building various demonstrators. My deepest thanks to Dr Penelope Leyland for her scientific intuition and immense help during my first days at EPFL.

My warmest acknowledgements go to my lab colleagues: Maxime Volery, Thach Pham Vu, Xinxin Guo, Vincent Grimaldi, Mathieu Padlewski, and Rahim Vesal. Thank you for creating the best possible atmosphere at work. I appreciate your time commitment and genuine willingness to help with challenging tasks. The countless discussions and mutual aid are the

Acknowledgements

distinguishing traits of our lab whose value I cannot express in words. Thank you also for all the great moments spent together outside the lab. I wish you all the best in your future careers and personal lives. I thank all the previous and present colleagues of LWE, MAG and LTS2 laboratories for all the daily chats and lunches together.

I would like to express my gratitude to my immediate and extended families in Russia. Thank you for always supporting my decisions and staying close to me, no matter how far we are. I am very grateful for your encouragement and trust in me. Lastly, this period of life would never remain so positive in mind without my love, wife, and best friend. Thank you for sharing with me all the enjoyable moments and supporting me in difficult times. Спасибо тебе за твоё терпение, заботу и бесконечную веру в меня.

Stanislav Sergeev

Abstract

Environmental noise, mostly related to human activities, has an immense impact on public health. The development of noise reduction technologies is paramount in addressing this problem. Because of practical and economic reasons, a compact, broadband, lightweight, and mechanically robust solution is often compulsory. Existing noise reduction methods typically fall short meeting these requirements. Passive absorbers are bulky and inefficient in the low frequency range or present only a narrowband performance. Active noise reduction methods, including active noise cancellation and acoustic impedance control, appear more promising as they allow extending the bandwidth of operation and remain small compared to a wavelength. An electrodynamic loudspeaker is conventionally a favourable choice for a controlled transducer. However, it limits efficient technology application due to its fragile diaphragm, relatively high weight, and inherent resonant nature, bounding the bandwidth of control.

This thesis is devoted to the development of a fundamentally different plasma-based electroacoustic transducer for active sound control applications. The acoustic field is manipulated by the partial ionisation of a thin air layer with an atmospheric corona discharge and its further control with an alternating electrical field. The transducer consists of a set of high voltage wires, separated with a grounded mesh by an air gap. Analytical and numerical models are first developed to design and characterise the corona discharge actuator. Several feedback impedance control strategies are adapted and implemented with the corona discharge actuator, resulting in achieving broadband impedance and sound absorption. A prototype of a plasma-based active acoustic liner for noise reduction under grazing sound incidence is proposed and assessed experimentally in laboratory facilities. A model-based feedforward approach for broadband control of acoustic impedance is then developed. Exploiting the unique physics of the corona discharge actuator with the help of the analytical model, perfect sound absorption and tunable acoustic reflection under normal incidence are achieved over two frequency decades, from several Hz to the kHz range. Such unprecedented bandwidth and compactness of the developed system, along with the simplicity of construction, lightweight, and flexible design, opens new doors in noise control applications, and acoustic metamaterials, among others.

Key words: Active absorption, plasma actuator, corona discharge, electroacoustic transducer, acoustic impedance control, active acoustic liner, target impedance.

Résumé

Le bruit ambiant, principalement lié aux activités humaines, a un impact considérable sur la santé publique. Le développement de technologies de réduction du bruit est primordial pour faire face à ce problème émergent. Ces solutions doivent être opérationnelles sur une large bande de fréquences, mais pour des raisons pratiques et économiques, elles doivent être compactes, légères et robustes mécaniquement. Les méthodes de réduction du bruit existantes ne répondent généralement pas à toutes ces exigences. Les absorbeurs passifs sont encombrants et inefficaces dans la gamme des basses fréquences, ou ne présentent qu'une performance à bande étroite. Les méthodes actives de réduction du bruit, notamment l'annulation active du bruit et le contrôle de l'impédance acoustique, semblent plus prometteuses car elles permettent d'étendre la bande passante de fonctionnement et restent petites par rapport à une longueur d'onde. Le haut-parleur électrodynamique reste le transducteur le plus souvent utilisé dans les applications de contrôle actif. Cependant, la fragilité de son diaphragme, ainsi que son poids relativement élevé et sa nature résonante, qui limite la largeur de bande du contrôle, restreignent son application à certaines applications pratiques.

Cette thèse est consacrée au développement d'un transducteur électroacoustique à base de plasma, fondamentalement différent du haut-parleur électrodynamique, pour des applications de contrôle actif du son. Le champ acoustique est manipulé par l'ionisation partielle d'une fine couche d'air avec une décharge corona atmosphérique et son contrôle ultérieur avec un champ électrique alternatif. Le transducteur est constitué d'un ensemble de fils mis à un potentiel électrique très élevé, ainsi que d'une grille métallique mise à la terre, les deux électrodes étant séparées par un espace d'air. Des modèles analytiques et numériques sont développés pour concevoir et caractériser l'actionneur à décharge corona, évalué dans un premier temps comme source acoustique. Ensuite, plusieurs stratégies de contrôle d'impédance acoustique par rétroaction sont adaptées et mises en œuvre avec l'actionneur à décharge corona, ce qui permet d'obtenir une impédance et une absorption acoustique, effective sur une large bande de fréquences. Un prototype de « liner » acoustique actif à base de plasma pour la réduction du bruit sous incidence rasante du son est ensuite proposé. Une approche de contrôle alternative basée sur un modèle du transducteur pour le contrôle à large bande de l'impédance acoustique est enfin développée. En exploitant la physique unique de l'actionneur à décharge corona à l'aide du modèle analytique, une absorption acoustique parfaite et

une réflexion acoustique accordable sont obtenues sur deux décades de fréquence, comprises entre quelques Hz et quelques kHz. Cette bande passante sans précédent et la compacité du système développé, ainsi que la simplicité de construction, la légèreté et la souplesse de conception, ouvrent de nouvelles portes dans les applications de contrôle du bruit et les métamatériaux acoustiques, entre autres.

Contents

Acknowledgements	i
Abstract	iii
List of Figures	xi
List of Tables	xvii
Introduction	1
1 Noise reduction methods	7
1.1 Passive sound absorption	7
1.1.1 Passive absorption with compact treatment	8
1.2 Active sound control	9
1.2.1 ANC versus impedance control	9
1.2.2 Sound absorption through impedance control	11
1.3 Conclusions	13
2 Plasma-based transducers	15
2.1 Introduction	15
2.1.1 Hot-plasma transducers	16
2.1.2 Cold-plasma transducers	16
2.2 Application to active sound control	17
2.3 Corona discharge actuator	21
2.3.1 Mechanism of corona discharge	22
2.3.2 Sound generation with corona discharge	23
2.3.3 Voltage-current characteristics	23
2.3.4 Positive versus negative corona discharge	25
2.4 Conclusions	26
3 Development of corona discharge actuator for sound control	29
3.1 Introduction	29
3.2 Geometry of the corona discharge actuator	29
3.3 Analytical model for sound sources in corona discharge	30
3.3.1 Governing equations	31

3.3.2	Force and heat sources	33
3.4	Numerical model for a corona discharge design	36
3.4.1	Electrostatics modelling	37
3.4.2	Acoustics modelling	39
3.4.3	Implementation in COMSOL	39
3.4.4	Maximising the output power	40
3.4.5	Simulation capabilities	42
3.5	Conclusions	46
4	Electroacoustic characterisation of the corona discharge actuator	47
4.1	CD actuator prototype	47
4.2	Experimental setup	48
4.3	Voltage-current characteristics	49
4.4	On-axis frequency response	50
4.5	Directivity patterns	52
4.6	Total harmonic distortion	54
4.7	Conclusions	56
5	Feedback impedance control of corona discharge actuator	59
5.1	Introduction	59
5.2	Hybrid passive-active impedance control	60
5.2.1	Principle of the hybrid absorption	60
5.2.2	Control design with FxLMS algorithm	61
5.2.3	Experimental setup	62
5.2.4	Achieved acoustic impedance and sound absorption	64
5.3	Pressure-velocity feedback impedance control	65
5.3.1	Methods to estimate particle velocity in front of corona discharge	65
5.3.2	Control design	67
5.3.3	Experimental setup	68
5.3.4	Achieved acoustic impedance and sound absorption	68
5.4	Application to acoustic liners	70
5.4.1	Noise reduction under grazing incidence	71
5.4.2	Prototype design and flow duct facility	72
5.4.3	Performance without mean flow	74
5.4.4	Performance in presence of mean flow	77
5.4.5	Influence on the flow noise	78
5.5	Conclusions	79
6	Feedforward model-based impedance control of corona discharge actuator	81
6.1	Introduction	81
6.2	Development of electroacoustic analytical model of corona discharge for control	82
6.3	Analytical derivation of control transfer function	83
6.4	Modelling absorption performance	88

CONTENTS

6.4.1	Influence of control delay on performance	91
6.5	Experimental setup and implementation	93
6.5.1	Experimental setup	93
6.5.2	Time delay of control system	94
6.6	Broadband sound absorption	95
6.7	Targeting different resistances	97
6.8	Acoustic mirror with various levels of reflection under normal incidence	99
6.8.1	Target impedance to control magnitude and phase of reflection	99
6.8.2	Experimental results	100
6.9	Conclusions	101
Conclusions		103
A Simple high voltage amplifier		111
B Additional figures and data		115
Bibliography		130
Curriculum Vitae		131

List of Figures

1.1	Sound absorption of a 35 mm layer of a fiberglass backed with a hard wall (blue line), and of a matched Helmholtz resonator with a similar depth. Models are taken from [19].	8
1.2	Conventional liner structure with face sheet 1, honeycomb core 2, and a back plate 3. Source [25].	9
1.3	Long finite duct with the sound source of constant flow velocity u_s and controlled source with velocity u_c	10
1.4	Bode plots of specific acoustic impedance from (1.6) and corresponding absorption coefficient. Data is taken from [45].	13
2.1	Schematic of a flat plate surface dielectric barrier discharge.	18
2.2	Time series of acoustic pressure signal and its power spectral density when DBDs are excited with 200 ns pulses with frequency 1 kHz and magnitude of 8 kV. . .	20
2.3	Time series of acoustic pressure signal and its power spectral density when DBDs are excited with AC sinusoidal signal at 1 kHz and magnitude of 8 kV.	21
2.4	Mechanism of a positive corona discharge operation. The direction of movement of the charged particles is illustrated with arrows. E - emitter electrode, C - collector electrode. Schematic, not to scale.	22
2.5	Voltage-current characteristics of a corona discharge actuator in a wire-to-mesh geometry measured experimentally and its approximation with a Townsend formula.	24
2.6	Sound pressure spectra of a corona discharge actuator powered with positive and negative polarity. Constant voltage level $U_{DC} = \pm 8.2$ kV, alternating sinusoidal voltage component u_{AC} equals to 200 Vrms for positive polarity, 150 Vrms for negative polarity at frequency 1 kHz. Background noise - the actuator is not powered.	26
3.1	Schematic view of a CD actuator in a wire-to-mesh geometry. Not to scale. . . .	30
3.2	CD actuator electrical current dependence on the number of emitter wires. Constant voltage U_{DC} is applied.	42
3.3	Three dimensional directivity pattern of the corona discharge actuator at 8000 Hz. $U_{DC} = 8.2$ kV, $u_{AC} = 300$ Vrms. The sound pressure level on the colour bar corresponds to the magnitude at the distance of 1 m.	43

3.4	Acoustic pressure in the vicinity of the electrodes at an arbitrary time moment. Actuator is biased with $U_{DC} = 8.2$ kV with applied sinusoidal signal at 1 kHz with amplitude $u_{AC} = 425$ V. The distribution is shown in the horizontal plane.	43
3.5	a) Electric field magnitude with equipotential lines; b) Space charge density; c) Current density magnitude. The actuator is supplied with constant voltage $U_{DC} = 8.2$ kV. The magnitude ranges indicated on the figures correspond to “min-max” colourbar, but do not represent the highest values calculated in the simulation.	44
3.6	a) Heat power density b) Force density magnitude. The actuator is supplied with constant voltage $U_{DC} = 8.2$ kV. The magnitude ranges indicated on the figures correspond to “min-max” colourbar, but do not represent the highest values calculated in the simulation.	45
4.1	Photo of the corona discharge actuator designed in a wire-to-mesh geometry. The top-right magnified picture highlights the high voltage electrode formed by the nichrome wire segments.	48
4.2	Schematic of the CD actuator measurements setup. Not to scale.	49
4.3	Voltage-current characteristics of the corona discharge actuator from Figure 4.1. Blue dots - measurements; red curve - least-squares fit of the experimental data with formula $I = CU(U - U_0)$, $C = 1.69e - 11$ A/V ² , $U_0 = 6190$ V; green curve - numerical simulation.	50
4.4	On-axis sound pressure levels of the corona discharge actuator in the frequency range 100 - 10000 Hz, measured at 1 m with $U_{DC} = 8.2$ kV, $u_{AC} = 300$ Vrms in blue. The data is compared with the analytical model (red curve) and numerical model (green curve).	51
4.5	Directivity patterns of the corona discharge actuator at frequencies 250, 500, 1000, 2000, 4000, 8000 Hz. Magnitude is in dB normalised to 20 uPa. $\theta = 0^\circ$ corresponds to the frequency response case. $U_{DC} = 8.2$ kV, $u_{AC} = 300$ Vrms.	53
4.6	Total harmonic distortion in percents of the CD actuator at frequencies 250, 500, 1000, 2000, 4000, 8000 Hz. The actuator is biased with $U_{DC} = 8.2$ kV.	55
4.7	Total harmonic distortion in percents of the CD actuator at frequencies 250, 500, 1000, 2000, 4000, 8000 Hz, calculated with the analytical model from Equations (4.2). The actuator is biased with $U_{DC} = 8.2$ kV, the needed parameters are taken from Table 3.1, and Figure 4.3.	56
5.1	Flow resistance of the layer made of porous material.	61
5.2	Block scheme of the adaptive algorithm for hybrid sound absorption.	62
5.3	Schematic of the experimental setup for the measurements of sound absorption under normal incidence. Hybrid sound absorption method with the CD actuator is implemented.	63
5.4	Acoustic impedance and absorption coefficient measurements of a system in passive and hybrid mode. The impedance is normalised by ρc	64

LIST OF FIGURES

5.5	Block diagram of the pressure-velocity feedback control of the corona discharge actuator. a) the particle velocity is estimated based on Euler equation. b) particle velocity is estimated with the use of a known resistive layer.	67
5.6	Schematic of the experimental setup for the measurements of sound absorption under normal incidence. Pressure-velocity feedback impedance control of the CD actuator is implemented.	68
5.7	Real and imaginary parts of the measured acoustic impedance in passive and active modes. Number 1 corresponds to configuration with velocity estimation according to Equation (5.6), 2 - according to Equation (5.7) with resistive material between microphones. Values are normalised by ρc	69
5.8	Measured absorption coefficient of the CD actuator with a pressure-velocity feedback control.	70
5.9	Scheme of the rectangular flow duct for measuring the liner absorption under grazing incidence. The second control microphone (M_{c12} and M_{c22}) is only used for direct feedback impedance control. The depth of the cavity is different for hybrid absorption and direct impedance control methods.	72
5.10	Test section with the plasma-based liner prototype mounted on a side wall. Left - two active cells comprising the liner (one is partially disassembled for illustrative purpose). Right - view from the duct inside, top cover is removed.	73
5.11	Transmission loss (left) and normalised acoustic impedance (right) of hybrid absorption system in comparison to passive behaviour without mean flow. + sign corresponds to measurement with the upstream source on, – with the downstream source on. Blue curves of passive measurements coincide. The Cremer impedance is calculated for a duct height of 40 mm.	74
5.12	Transmission loss (left) and normalised acoustic impedance (right) of direct impedance control system in comparison to passive behaviour without mean flow. The Cremer impedance is calculated for a duct height of 40 mm.	75
5.13	Transmission loss (left) and normalised acoustic impedance (right) of direct impedance control system in comparison to passive behaviour in a mean flow with $M = 0.05$. The Cremer impedance is calculated for a duct height of 40 mm.	77
5.14	Sound pressure levels of broadband noise created by the flow in the duct. Passive – actuators are off, active – actuators are on with pressure-velocity feedback. Signals are recorded by 2 closest downstream microphones M_4 and M_5	78
6.1	The principle of sound absorption with the corona discharge closed in a box. In passive regime (a) the actuator behaves as a rigid termination with electrode grids transparent to sound. In active regime (b) heat H and force F sound sources are operating in order to suppress reflected wave. Shape of the sinusoidal wave from the heat source (red) and force source (blue) represents the monopolar and dipolar property correspondingly.	82
6.2	One dimensional schematics of acoustic sources and boundaries positions.	84

6.3	Bode plots of transfer functions $\theta(\omega)$ from (6.7) and $\theta(s)$ from (6.9) with target impedance $Z_{tg} = \rho c$. The light blue filled area shows the change in phase of $\theta(s)$ if time delay in control is introduced.	87
6.4	Geometry of the two dimensional waveguide terminated with the enclosed corona discharge actuator. The triangular mesh is denser towards the rectangular zone which imitates the discharge (highlighted in violet). The microphone position is a blue dot with coordinates (-0.01, 0.025).	88
6.5	Simulated achieved normalised impedance and sound absorption coefficient of the CD actuator in 3 cases: control off (blue); ideal control transfer function according to Equation (6.7) (orange); simplified control transfer function as in Equation (6.8). Solid lines on the impedance graph represent the real part of achieved impedance, dashed lines - imaginary part. $Z_{tg} = \rho c$	90
6.6	Simulated performance if the active system is controlled with transfer function from Equation (6.9) with the time delay 0-80 μs . Left: achieved sound absorption coefficient; right: achieved normalised acoustic impedance. Solid line - real part of impedance, dashed line - imaginary part of impedance.	91
6.7	Absorption coefficient map as a function of frequency and the introduced delay. The active system is controlled with transfer function from Equation (6.9). Note, that the minimal value in legend is set to 0.95, but blue colored zones contain data with lower absorption coefficient (down to 0.66).	92
6.8	Schematics of experimental setup, including the impedance tube, block scheme of active control and signal acquisition.	93
6.9	Frequency response of the high voltage amplifier TREK 615-10 loaded with the CD actuator introduced in Section 4.1. The signal is recorded from the embedded voltage probe, so the voltage magnitude is reduced by a factor of 1000.	94
6.10	Phase difference between the measured response of the controller, which runs the discretised version of the transfer function (6.9) with a sampling frequency of 50 kHz, and the transfer function (6.9).	95
6.11	Experimentally achieved performance of the CD-based active sound absorber in the duct with $Z_{tg} = \rho c$ and comparison with a numerical model. Top row - passive operation of the absorber; middle row - active operation with control time delay $\approx 30 \mu s$; bottom row - active operation with control time delay $\approx 50 \mu s$. Blue lines - numerical simulation, red lines - measurements. Transfer function (6.9) is implemented. On impedance graphs: solid line - real part of impedance, dashed line - imaginary part of impedance.	96
6.12	Left: bode plots of transfer functions $\theta(\omega)$ (6.7) and $\theta(s)$ (6.9) with $Z_{tg} = 0.5\rho c$ and $Z_{tg} = 2\rho c$ without time delay. Right: achieved acoustic impedances for the corresponding control cases control cases with $Z_{tg} = 0.5\rho c$ and $Z_{tg} = 2\rho c$, 30 μs delay is set in the simulation. On the impedance graph: solid line - real part of impedance, dashed line - imaginary part of impedance.	98

LIST OF FIGURES

6.13	Demonstration of a tunable various levels of sound reflection with the CD actuator. By varying the target impedance after Equation (6.11), reflection coefficient of 40, 70, 90 percent is achieved.	100
6.14	At a fixed reflection level, the linear roll-off of the reflection phase is controlled, artificially introducing a constant reflection time delay. Delays of 0.22, 0.56, 0.85 ms correspond to virtual elongations of the device by 3.7, 9.7, 14.7 cm, respectively.	101
A.1	Block scheme of the high voltage amplifier for a corona discharge (single amplification channel is illustrated).	112
A.2	Photo of two channel high voltage amplifier for a corona discharge actuator. . .	113
A.3	Frequency response of the amplifier from Figure A.2, when it is connected to the CD actuator.	114
B.1	A- and Z- weighted noise levels over octave bands produced by a positive and negative corona discharges. Constant voltage level $U_{DC} = \pm 8.2$ kV is applied. Microphone is placed at 1 m in front of the actuator.	115
B.2	Three dimensional directivity of the corona discharge actuator at 1000 Hz. $U_{DC} = 8.2$ kV, $u_{AC} = 300$ Vrms.	116
B.3	Electric field magnitude with equipotential lines of the CD actuator, where the emitter electrode is composed of two wires. A constant voltage of $U_{DC} = 8.2$ kV is applied.	116
B.4	Total harmonic distortion in percents of the CD actuator at frequencies 250, 500, 1000, 2000, 4000, 8000 Hz. The actuator is biased with $U_{DC} = -8.2$ kV.	117
B.5	Test section with the plasma-based liner prototype mounted on a side wall. Left - two active cells comprising the liner (one is partially disassembled for illustrative purpose). Right - view from the duct inside, top cover is removed. The liner is assembled for the pressure-velocity feedback configuration.	117
B.6	Transmission loss measurement with active impedance control method. No mean flow, sound pressure level of acoustic signal is 90 dB. Only $TL+$ curves are illustrated.	118
B.7	Transmission loss measurement with active impedance control method. Mean flow with $M=0.03$, sound pressure level of acoustic signal is 95 dB. Only $TL+$ curves are illustrated	118
B.8	Bode plots of transfer functions $\theta(\omega)$ from (6.7) and $\theta(s)$ from (6.9) with target impedance $Z_{tg} = \rho c$. The response is shown in the frequency range 10-50000 Hz.	119
B.9	Voltage-current characteristics of the corona discharge actuator measured for Chapter 6. Blue dots - measurements; red curve - least mean square fit of experimental data with formula $I = CU(U - U_0)$, $C = 2.31e - 11$ A/V ² , $U_0 = 6190$ V.	119

List of Tables

3.1	Physical and geometrical parameters of the CD.	40
5.1	Parameters for pressure-velocity feedback impedance control with target impedance from equation 5.10. $M = 0.044 \text{ kg}\cdot\text{m}^{-2}$, $R = 35 \text{ Pa}\cdot\text{s}\cdot\text{m}^{-1}$, $C = 4.3\text{e-}7 \text{ m}\cdot\text{Pa}^{-1}$. . .	76
6.1	CD actuator model parameters for a definition of a control transfer function. .	89

Introduction

Context

In the contemporary urban environment, the population is constantly exposed to acoustic noise. The current technological progress rapidly increases the presence of noisy machinery in our lives. The growing noise levels negatively impact physical and psychological health of the population [1]. In response to this, modern rigorous regulations get adopted to constrain the emerging problem. Therefore, noise reduction methods have to progressively increase efficiency and be suitable for the new needs.

On the other hand, noise becomes more difficult to tackle in various industry sectors. Aircraft noise is considered to be one of the most annoying and harmful, especially in the vicinity of airports [2, 3]. Aircraft noise is mainly emanated from the aerodynamic frame and the engine. Recent research found novel aircraft configurations with promising low frame noise characteristics [4]. However, the problem with the engine noise remains. Novel engine developments have been focusing on reducing fuel consumption by increasing the by-pass ratio that lowers down the fan's rotation speed. As a result, the frequency range of the tonal noise decreases compared to previous generations. This poses a challenge to the acoustic treatment to be installed in the engine nacelle due to the limited space [5]. Indeed, the available space for noise reduction treatment is limited in depth by several centimetres. It should host a noise reduction solution capable of tackling the waves of much longer lengths. Although the engine noise is tonal, the central frequency can considerably shift depending on the regime. In addition, the total weight of the treatment and its compliance with the harsh environmental conditions are essential factors to consider. The scope of examples with potentially similar demands goes well beyond the aircraft sector. Increasing road traffic also requires noise reduction solutions. Although the transition towards electric vehicles is expected to bring benefits from the deliverance of a combustion system, the tire noise and the exposure of an electrical motor remain the strongest factors of annoyance [6]. Ventilation systems and machinery in workshops also emit low frequency but broadband noise. As its sources cannot be isolated from the environment, the noise should be reduced. Therefore, the need for a breakthrough in noise control technologies is now driving many industries and interdisciplinary research in acoustics. Unfortunately, in the number of applications, the state-

of-the-art methods cannot satisfy all the requirements, including compact size, broadband performance, and mechanical robustness, among others.

Motivation

The active noise cancellation technique can be used to remarkably reduce the sound pressure levels at a particular location with controlled electroacoustic sources. It was proven to decently work with simple geometries, such as in headphones or ducts, suppressing tonal and low frequency noises [7, 8, 9, 10]. However, three-dimensional spaces require a large number of controlled transducers and sensors and high computational costs [11]. Moreover, the method introduces additional acoustic energy in the acoustic volume and can make other locations louder than without treatment. Alternatively, sound absorption methods also help lowering down the noise in spaces.

Like any other sound, noise approaching a surface can be transmitted, absorbed, or reflected. The surface properties define in what proportions the acoustic energy divides among these three scenarios. Thus, a specifically engineered interface can reduce noise by absorbing its energy. No matter how strange it may sound, after years of noise control engineering development, the best sound absorber remains the bulk of a porous material. However, it is well known that the visco-thermal losses should be induced in a size comparable to the wavelength to efficiently absorb sound [12], which makes it impractical for space limited applications, especially at low frequencies. To advance in the low frequency problem, various resonator-based structures are proposed. They combine membranes, cavities, and resistive layers, which can be adjusted to absorb selected frequencies, but the performance is inherently narrowband. A relatively new research venue in passive acoustic meta-materials produces rather appealing progress. Although such absorbers may be highly compact compared to the wavelength of absorption [13], they still struggle to both hit the low frequency range and be broadband. Moreover, the design is very case-specific, and fabrication often requires the involvement of sophisticated additive manufacturing processes.

Sound absorption can be achieved by actively controlling the acoustic impedance in front of an electroacoustic transducer. Impedance matching is also proposed by combining passive and active approaches, where the active element acts as a sink for sound waves, inducing energy loss through a passive resistive layer [14]. If the acoustic impedance of a boundary is matched to the characteristic impedance of the medium, the incident energy can be absorbed, leading to a noise reduction in the volume. Impedance control was shown to be relatively simple to implement at a low computational cost [15, 16]. Its tunability and potential to treat complex sound fields complete our motivation for the strategies investigated in this thesis.

The majority of works utilise membrane-based electroacoustic transducers (mostly electrodynamic loudspeakers) as the controlled actuators to convert an electric command into an acoustic response. The dynamic behaviour of conventional loudspeakers can be well captured by simple lumped-element analytical models [17]. The prevalence of loudspeakers on the

market, their cost and electromagnetic properties make these transducers a favourable choice for many control applications. However, this solution can be less suitable in certain situations. For instance, when a large number of transducers is required to cover a surface, the weight of the total system can become unacceptable. Furthermore, active control solutions are likely to be required in harsh environments with high Sound Pressure Levels (SPL) and extreme climatic conditions. Since a loudspeaker membrane is typically composed of cellulose, it may not sustain extreme loads. Piezoelectric actuators are an alternative technology for active noise control. Despite a more robust and lightweight design, a relatively small bandwidth of operation limits their application. The passive impedance of these transducers is represented by the one of a single degree of freedom resonator. At higher frequencies, it is controlled by the mass, which limits the control of impedance due to its inertia. Decreasing the moving mass in the transducer can reduce the controllability problem and extend the bandwidth of the impedance control performance. Ideally, the way to control an air interface without any additional mass raises the highest interest. The air ionisation phenomenon, which can be classified as a partially ionised atmospheric plasma, and its control with an electric field can be imagined. Different types of atmospheric plasma discharges showed their capability to influence the air medium in the domain of flow control [18]. Moreover, a few works demonstrate the possibility of plasma actuators to affect the sound field and behave as a loudspeaker. The potential of plasma actuators for being actively controlled along with their robustness qualities opens an absolutely new research domain, which becomes a central core of this thesis.

Objectives

This thesis aims to develop an alternative electroacoustic actuator for use in active impedance control that does not present several shortcomings of the conventional transducers. For treatment of extended surfaces, a loudspeaker of a large radius is impractical due to the immense mass of the membrane. A large number of transducers increases weight, circular shape of the membrane cannot cover the surface efficiently. Thus, an alternative transducer should be more flexible in design. Besides, as discussed previously, the lower weight of the transducer is of high interest. The structural robustness and, more importantly, a large bandwidth complete the scope of specifications for active control transducers. We propose to leverage the inherently non-inertial dynamics of the plasma-based actuators to develop an electroacoustic transducer for fundamentally broadband impedance control, which is lightweight, can be scaled in size and mechanically robust. Specifically, this thesis focuses on designing a corona discharge type transducer and impedance control methods for it. Since, to the author's knowledge, it is the first work in this field, the identification of the most optimal basis for the transducer design is required, the physical model of its operation and control should be developed, along with the implementation of the impedance control techniques.

The work in this thesis was partially supported by the Horizon 2020 project ARTEM - Aircraft noise Reduction Technologies and related Environmental iMpact. However, the thesis is

written in a more general sense since the current research results target a much broader spectrum of potential applications and implementation.

Outline and contributions

This section summarises the composition and original contributions of the thesis chapters.

Chapter 1: Noise reduction methods

Description: The chapter provides a brief review of the state of the art of passive and active noise reduction methods. The difference between active noise cancellation and impedance control is illustrated. The key concepts of the active impedance control are presented together with the focus on analysis of the conventional transducers used. The primary limitations that constrain the acoustic performance of the conventional transducers are identified. The chapter justifies the need for an alternative type of electroacoustic transducer.

Chapter 2: Plasma-based transducers

Description: A review of plasma-based actuators and their electroacoustic dynamics is carried out. The application of these actuators to active sound control is discussed. The dielectric barrier discharge and corona discharge are considered in more detail, including their principles of operation and produced sound spectra. Corona discharge actuator is identified as the most promising. The relationship between applied voltage and current in a corona discharge is discussed. Positive and negative polarities of a corona discharge are compared in terms of produced background noise during the operation.

Original contribution: The analysis of existing plasma-based actuators in the view of active control application leads us to the consideration of the dielectric barrier discharge and corona discharge. Due to a strongly nonlinear electroacoustic response of the dielectric barrier discharge, the transducer operating on the principle of atmospheric corona discharge is identified as the most suitable for active control applications. The experimental voltage-current characteristics of the discharge can be approximated by a simple formula that allows developing an analytical model of the actuator. The direct comparison of the recorded sound pressure spectra disqualifies the negative polarity of the corona discharge due to significantly higher levels of background noise produced along with the useful signal.

Chapter 3: Development of a corona discharge actuator for sound control

Description: This chapter considers the wire-to-mesh geometry of the corona discharge actuator. For the transducer development, it is helpful to have a model that can substitute resource-consuming experimental work. Moreover, some details, such as the distribution of the electrical parameters between the electrodes of a plasma-based transducer are difficult to

measure. Therefore, this chapter presents two models for this purpose. First simple analytical model considers discharge as a small portion of the medium with acoustic sources that can be defined through the voltage and total current flowing through the actuator. It can describe the transducer's low frequency sound radiation in the far field approximation. Second numerical model considers the actuator's fine geometry. Along with the radiation data, it can provide the distribution of electrical field, current, charge, as well as the distribution of acoustic sources in the interelectrode volume. With the help of the numerical model, the final geometry is defined for further experimental testing.

Original contribution: Through the review of state of the art and requirements for active sound control, we justify the choice of the wire-to-mesh geometry for the corona discharge actuator. The developed analytical model does not require any sophisticated calibration procedure to fully define it. Instead, a simple measurement of voltage-current characteristics is sufficient to set up the model. A numerical model, in contrast to the analytical one, is self-sufficient and can be used to design the actuator completely without experimental part. Several simplifications in the model are proposed in order to avoid complete modelling of the ionisation phenomenon. The coupling with the acoustic domain gives access to the radiation properties of the transducer. The simulation data provides indirect validation of several assumptions made in the analytical model. The numerical simulation is used to optimise the arrangement of the high voltage wires in the actuator in order to maximise the electrical and acoustic output power.

Chapter 4: Electroacoustic characterisation of the corona discharge actuator

Description: The corona discharge actuator is evaluated as a sound source. A $5 \times 5 \text{ cm}^2$ prototype, which is used in all the experimental studies of this thesis, is presented. The voltage-current characteristics of the discharge is measured to set up the analytical model. The basic acoustic characteristics such as frequency response, directivity patterns, and total harmonic distortion are assessed. The experimental measurements are compared to the estimations given by the numerical and analytical models.

Original contribution: Good correspondence of the experimental measurements with the analytical and numerical estimations proves the validity of the models. The low frequency behaviour, which covers the frequency range of interest for control applications, can be well captured with the analytical model. The numerical simulation remains accurate at higher frequencies, because the size and shape of the actuator is taken into account. The analysis of the experimental data confirms the suitability of the developed actuator for sound control.

Chapter 5: Feedback impedance control of corona discharge actuator

Description: The chapter starts with the introduction of the feedback impedance control methods. Then it considers the hybrid passive-active and direct pressure-velocity feedback impedance control for implementation with a corona discharge transducer. The principle of

each control strategy is first presented. The experimental assessment under normal sound incidence is carried out when the system targets full absorption. The application of these feedback techniques under grazing incidence is also considered. The prototype of a plasma-based acoustic liner consisting of two adjacent transducers is tested under grazing incidence in a rectangular duct with the aim to induce maximal transmission losses in a broadband manner or focusing on a specific frequency range. The measurements without and with the presence of a mean flow are presented.

Original contribution: Feedback methods allow controlling the acoustic impedance of an arbitrary transducer with the use of external sensors. Hybrid passive-active method and direct pressure-velocity with a proportional feedback design are proposed. The study on the approaches to estimate the particle velocity in front of the corona discharge actuator is carried out. The control methods are simple to implement and the target impedance can be imposed in a broad frequency range. Broadband sound absorption can be achieved under normal sound incidence. The specifically designed impedance for grazing incidence in a duct can lead to broadband or selective transmission losses. The advantages and limitations of each method in the perspective of operation with the corona discharge actuator are analysed.

Chapter 6: Feedforward model-based impedance control of corona discharge actuator

Description: This chapter introduces an approach that relies on a physical model of a corona discharge transducer to control the acoustic impedance. The analytical model, which estimates the acoustic sources of the actuator in chapter 3, is further elaborated to derive a control transfer function. The influence of the time delay in a realistic controller on the performance at high frequencies is studied. The control approach is implemented experimentally. Various impedances are targeted to either induce a perfect broadband absorption, or partial sound energy reflection.

Original contribution: The model-based strategy is proposed resulting in usage of a single microphone sensor as the input for the controller. The sound absorber becomes significantly more compact and goes deep in a subwavelength scale down to $\lambda/1000$ ratio while operating over two frequency decades. The initially almost lossless system can be tuned to absorb partially or fully acoustic energy. The consideration of a real-life controller time delay is essential to improve the high frequency performance. The achieved performance represents a significant milestone in broadband control of sound.

Chapter: Conclusions

Description: The key findings of the present thesis are summarised in this chapter. It is followed by the analysis of the current limitations observed in work and the suggestions for potential improvement and further research.

1 Noise reduction methods

This chapter reviews the existing passive and active methods of noise reduction. Active noise cancellation (ANC) and active impedance control methods are compared in the example of noise reduction in a duct. The advantages and limitations of each method are discussed.

1.1 Passive sound absorption

One of the conventional methods for noise reduction is the use of porous materials such as mineral and organic wools, open pore foams, fibrous materials, etc. The incident sound propagates inside the material and dissipates its energy due to the thermoviscous interaction with the material structure. Among the acoustic applications in rooms and noisy environments, these materials are widely used in civil engineering since they serve in parallel as thermal insulators. When a rigid wall backs a porous material, the sound pressure is maximal, but particle velocity is close to zero near the boundary. As a result, the induced losses are minimal at the long sound wavelengths. To increase the absorption at low frequencies, a large layer of porous material comparable to the wavelength is needed. Thus, these absorbers become quite inefficient when a low frequency sound should be absorbed with a compact treatment. As an example, Figure 1.1 shows a normal incidence absorption coefficient of a 35 mm layer of fibreglass backed with a rigid wall (35 mm is a typical available size of treatment for acoustic liners used in aircraft engine noise reduction). The curve represents a typical absorption dynamics of a porous material with such thickness. It absorbs more than 80% of acoustic energy only above 1000 Hz. However, machinery and transportation noise often contains energy in the lower frequency range.

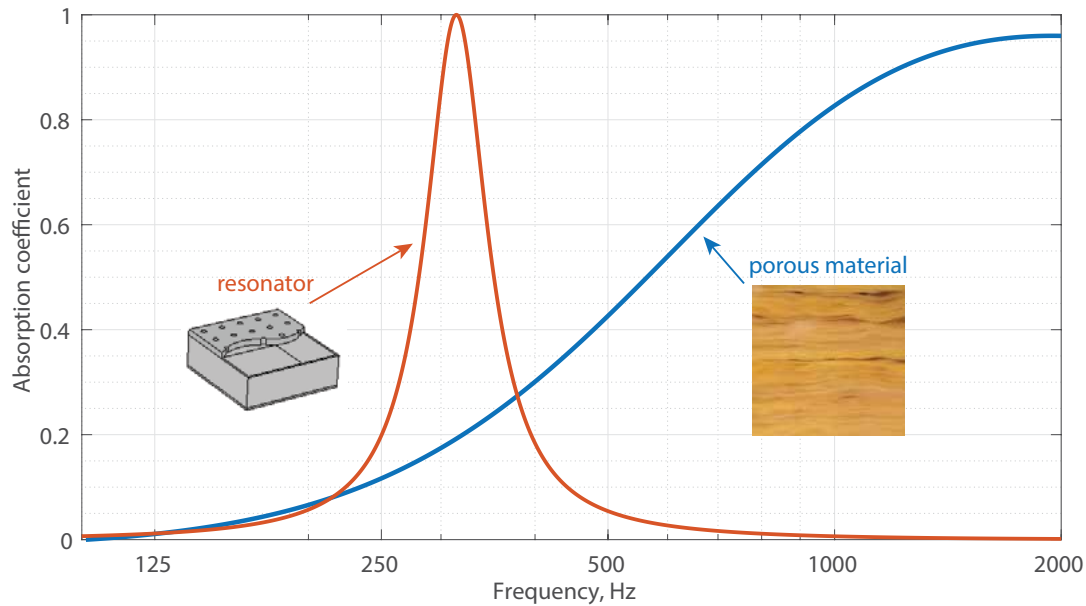


Figure 1.1: Sound absorption of a 35 mm layer of a fiberglass backed with a hard wall (blue line), and of a matched Helmholtz resonator with a similar depth. Models are taken from [19].

1.1.1 Passive absorption with compact treatment

To decrease the ratio of the treatment size to the absorbed wavelength, the resonating structures are employed [20, 21]. They include Helmholtz resonators, which consist of rigid cavities connected to the environment through thin air-filled necks. By varying the porosity, depth of the necks, and the cavity dimensions, the sound attenuation can be tuned to a specific frequency range [22]. This type of resonant absorbers is commonly used for the reduction of noise in the aircraft engine and is called an acoustic liner (Figure 1.2). The sound absorption induced by a Helmholtz resonator of a few centimetres depth is illustrated in Figure 1.1 with the orange curve. As can be seen, low frequency absorption can be achieved, but the peak is narrowband due to the high quality resonance. Such an absorber can suit well for a tonal signal at a fixed frequency. However, for instance, during the aircraft engine operation, the prevailing noise frequencies shift during take off and landing phases. Hence, multiple degrees of freedom resonators combining different diameters of holes and cavity sizes can be interconnected to increase the number of frequency regions that can be absorbed [23]. Despite the improved acoustic results, the greater thickness and weight of such absorbers limit their application. Alternatively, vibrating membrane absorbers can also address a low frequency sound [24]. The combination of Helmholtz resonators with membranes and porous materials increases the system damping and can slightly extend the absorption bandwidth [25, 26]. In the last decades, various acoustic metamaterial concepts have been proposed to manipulate sound. The metamaterials are also commonly constituted by an ensemble of subwavelength resonators. These structures are intricately designed to exhibit remarkable acoustic properties,

among which the low frequency perfect absorption can also be found [27, 28, 29, 30, 31, 32, 33]. However, the frequency regions over which they effectively operate are still either narrowband or located at relatively high frequencies.

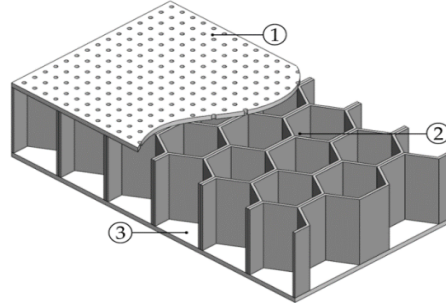


Figure 1.2: Conventional liner structure with face sheet 1, honeycomb core 2, and a back plate 3. Source [25].

Alternatively, the reciprocity of electroacoustic transducers can be utilised to absorb sound. In this control method named “shunt-based”, a passive electrical circuit connects the terminals of a transducer and introduces an electrical resonance. It is designed in a way to match at a certain frequency the impedance of a transducer to the optimal one for vibration damping or sound absorption. Such a control technique was studied to absorb low frequency sound with electrodynamic loudspeakers and piezoelectric transducers [34, 35, 36].

As can be seen from this short review, passive sound absorbing structures struggle to both hit the low frequency range and be broadband. Indeed, Kramer-Kronig relations constrain the response of any passive, linear, causal system. It can even be translated into unavoidable bounds between the device size and the bandwidth of operation [37].

1.2 Active sound control

Active control enables overpassing the limitations of passive materials and metamaterials [13]. By providing energy to a system, it is possible to expand the frequency range of operation with desirable properties and achieve new functionalities. Moreover, active approaches allow reconfiguring the materials in real-time, thus achieving various behaviour without structural modification [38]. Noise reduction can be realised using active noise cancellation (ANC) techniques and acoustic impedance control.

1.2.1 ANC versus impedance control

First, let us highlight the physical concepts and difference between active noise cancellation and impedance control strategies. For this purpose let us consider a finite air-filled duct as a propagation medium (Figure 1.3) with a velocity source u_s at the position $x = 0$. The total sound pressure and particle velocity at point x can be written as a sum of two plane waves

propagating in the directions shown in Figure 1.3:

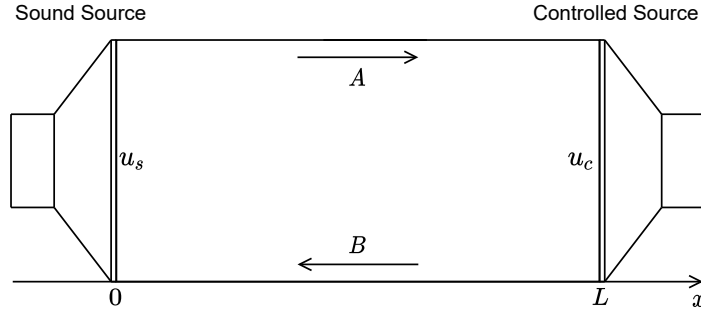


Figure 1.3: Long finite duct with the sound source of constant flow velocity u_s and controlled source with velocity u_c .

$$p(x) = Ae^{-jkx} + Be^{jkx}, \quad u(x) = \frac{1}{\rho c} [Ae^{-jkx} - Be^{jkx}], \quad (1.1)$$

where ρ is the medium density, c is sound speed, $k = \omega/c$ is a wavenumber at angular frequency ω . Here the time dependence is omitted. If a hard wall is present at the right end of the duct, the particle velocity at the position $x = L$ is zero. The velocity at $x = 0$ is controlled by the source and equals u_s . With these two boundary conditions, the amplitudes A and B of the incident and reflected waves can be derived and recover the pressure field in the whole duct. The resulting pressure field presents the resonance frequencies corresponding to $L/\lambda = 0, \frac{1}{2}, 1$, etc, that are associated with a closed-closed duct.

Suppose the controlled transducer with velocity u_c is placed at the right termination. In this case, the boundary conditions are the following: $u(0) = u_s$, $u(L) = -u_c$ (minus sign imitates the reversed position of the controlled transducer relative to the source). The resulting amplitudes of the incident and reflected waves are:

$$A = \rho c \frac{u_s + u_c e^{-jkL}}{1 - e^{-j2kL}}, \quad B = \rho c \frac{u_s + u_c e^{jkL}}{e^{j2kL} - 1}, \quad (1.2)$$

From this, the total pressure field along the duct in Equation (1.1) can be calculated. Now we can discuss the effect of each control strategy. The velocity u_c of the secondary source is a parameter that we are free to vary in order to obtain the desired result.

The first strategy is the cancellation of pressure at the target position. For example, to set the total pressure at the position of the secondary source to zero, one should satisfy the boundary condition at the right termination $p(L) = 0$. Using this condition for the pressure field with

wave amplitudes from Equation (1.2), the velocity of the controlled transducer should be the following:

$$u_c = -\frac{u_s}{\cos(kL)}. \quad (1.3)$$

Under this condition, the duct behaves as closed/open instead of closed/closed without control. It means, that despite a silent location at position L , the duct still resonates at the excitation frequencies $L/\lambda = \frac{1}{4}, \frac{3}{4}$, etc. leading to higher SPLs at some locations in a duct than in the no control case. Although we consider an example of a controlled termination in a duct, the same effect can be observed in more complex spaces. Creating a noise reduction locally does not mean the noise is reduced in the whole space. To achieve this, a more complex control with a greater number of transducers and sensors is needed. The complexity further increases if the control is needed at higher frequencies [39, 40, 41].

The second strategy relies on the controlled transducer's absorption of the incident pressure wave. In this case, the reflected wave amplitude B should equal zero. In Equation (1.2) it is achieved when:

$$u_c = -u_s e^{-jkL}. \quad (1.4)$$

This velocity of a controlled transducer makes the right termination of the duct fully absorbing. Finally, the sound pressure has a constant magnitude along a duct, which commonly leads to noise reduction and pressure equalisation in spaces because the energy does not accumulate in a system. If we define a specific acoustic impedance $Z(x) = p(x)/u(x)$, it can be found from Equations (1.1) and (1.3) with transducer velocity from Equation (1.4) that the impedance at the right termination equals to characteristic impedance of air ρc . In other words, it is possible to drive the secondary source in order to create an impedance matched condition, which leads to sound absorption. This method is referred to as impedance control and was found to be a powerful tool for sound absorption utilising electroacoustic transducers.

1.2.2 Sound absorption through impedance control

Impedance control can be considered as a local method, where the boundaries of the acoustic field are controlled in order to absorb sound power. Different approaches exist to assign a desired impedance to the transducer interface. If the transducer is reciprocal (can be used as a source and as a sensor), the abovementioned passive but also active electrical shunts can be connected to it and synthesise the needed impedance [42, 43]. Feedback control relies on the use of external sensors providing information from the acoustic field. For electrodynamic

transducers, the formal analogies are made, unifying the theory for passive shunts and active impedance control approaches [44]. The analytical model of the transducer can be integrated in the feedforward control design in order to reduce the number of used sensors [45]. The feedback and feedforward impedance control approaches are further discussed in more detail in Chapters 5 and 6 of the present thesis.

An electrodynamic loudspeaker is typically used as a controlled transducer. As was discussed in the introduction, these transducers are reasonably a favourable choice for many control cases. However, their large weight when assembled in arrays, fragile membrane and suspension, and a constraint on a bandwidth of control limit the use in certain cases. The problem of the constrained bandwidth originates again from the resonant nature of the transducer and should be commented more in detail.

A loudspeaker can be considered as a single degree of freedom resonator, which is actuated with a voice coil moving in a magnetic field. The mechanical part is represented by a mass-spring-damper system in the low frequency approximation. The passive specific acoustic impedance of a loudspeaker reflects the mechanical one and, in the case of the open circuit in the frequency domain, writes:

$$Z_s(\omega) = j\omega \frac{M}{S} + \frac{R}{S} + \frac{1}{j\omega CS}. \quad (1.5)$$

In this expression, M is a moving mass (primarily membrane and voice coil), C is the mechanical compliance taking into account suspension and the acoustic compliance of the enclosure, R is a mechanical resistance representing damping in the system, S is the diaphragm area. The additional term appears in Equation (1.5), if the loudspeaker is supplied with power. At low frequencies, the impedance is controlled by the compliance, and at high frequencies, by the mass. Thus, away from the resonance frequency, its magnitude is high because of the reactive terms. To obtain a constant resistive impedance with control, a loudspeaker driver would require the energy supply, which increases as the frequency furthers from the resonance. It happens due to the growing mismatch of passive and target impedances. Thus, targeting pure resistance can lead to unstable behaviour. In this sense, as the mass and compliance cannot be completely removed, the target impedance similar to the passive is proposed in [45].

$$Z_{st}(\omega) = j\omega \mu_M \frac{M}{S} + \mu_R \frac{R}{S} + \mu_C \frac{1}{j\omega CS}. \quad (1.6)$$

The weighting factors μ change the targeted impedance from the passive one. For a broadband absorption under normal incidence, the μ_R should be chosen to match the resistance to the characteristic medium impedance, and μ_C, μ_M should be reduced to the minimum, which is

defined by stability threshold. Figure 1.4 shows an example of the modelled target impedance response from Equation (1.6) and achieved sound absorption coefficient of Peerless SDS-P830657 driver in a 10 dm³ closed-box (data is taken from [45], case C) when the largest bandwidth of absorption is aimed. The absorber presents relatively broad but still band-pass performance due to the presence of reactive terms. With $\mu_C = \mu_M = 0.15$, the deviation from an ideal ρc impedance is seen away from the resonance frequency. Moreover, if a model-based control is used, it is typically susceptible to the quality of parameters estimation around the natural resonance frequency. It can cause artefacts in the achieved impedance and absorption and lead to loss of stability [46, 47]. Similar mechanical-acoustic analogies relate to the piezoelectric transducers, if their impedance is controlled [48, 49].

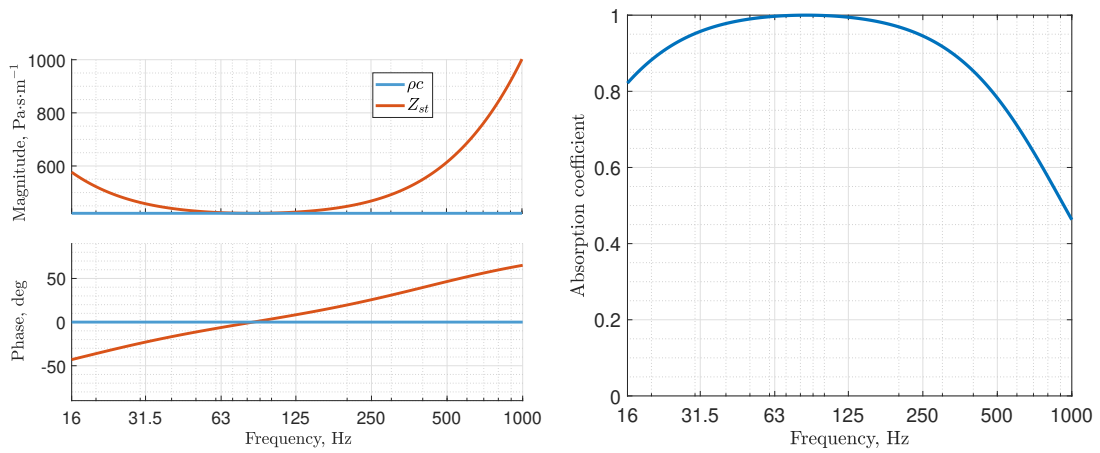


Figure 1.4: Bode plots of specific acoustic impedance from (1.6) and corresponding absorption coefficient. Data is taken from [45].

1.3 Conclusions

Finally, reactive components in the conventionally used transducers limit the bandwidth of impedance control. Therefore, controlling the air medium without any moving parts could significantly reduce the inertia and increase the bandwidth. This idea, together with the other abovementioned potential limitations of the conventional transducers, including the driver weight, and compliance to harsh environments, smoothly brings us to the considerations of plasma-based actuators. The next chapter guides through the domain of plasma actuators and focuses on a design of a specific type of plasma-based transducers most suitable for active control applications.

2 Plasma-based transducers

2.1 Introduction

Plasma in physics is one of the four fundamental states of matter. This name, which initially appeared due to some analogies with blood plasma, implies that a substance contains a significant proportion of charged particles: various ions and electrons. As a consequence, the electric and magnetic fields play a significant role in the particle interaction processes. This is a particularly fascinating aspect for the present work. Indeed, to manipulate the sound field with conventional transducers, one should apply an electrical signal to its terminals, which converts into a mechanical movement of a diaphragm and by this locally acts on the air bulk. This disturbance propagates then as an acoustic wave. An alternative electroacoustic process can be imagined with plasma. In the case of not fully ionised plasma, the charged particles are diluted together with neutrals. The movement of charged species can be controlled by an external electrical signal, which locally induces an electrical field. The energy gained in the electrical field by charged particles can be transported to the neutral particles through elastic and inelastic collisions. Therefore, if a neutral gas surrounds the plasma volume, it is possible to create a controllable movement that further propagates as a sound wave. In such a hypothesis, we can suppress the mechanical part of the transducer, which slows down the electroacoustic conversion due to its inertial response to an electrical signal. The time constants of interaction in atmospheric plasmas lay in the range $10^{-9} - 10^{-6}$. Thus, no resonant behaviour can be expected in the audible frequency range, which is particularly interesting for broadband control of sound.

Gas can be ionised in different ways. To ionise a particle, sufficient energy should be provided to it. This can be done by heating the gas (stars and some hot flames), extreme gas confinement (plasma in tokamaks), chemical ionisation (in organic gases), or by applying a strong electrical field (gas discharges). As the goal is to work in the atmospheric air close to normal conditions,

the gas discharge is the most reasonable option to produce a volume of ionised gas.

A gas discharge implies the electrical current flow in the gas gap between the electrodes. The ionisation process is triggered by the free electrons always present in the gas volume. If within a distance λ called free path length the electron can gain enough energy, at the collision with a particle the latter can lose its own electron. The process will continue exponentially, causing an electron avalanche and establishing a discharge in the electrode gap. At the atmospheric conditions in air, most of the discharges can be considered as the transducers, as they directly interact with the surrounding gas volume and transfer the energy in various forms. The sound waves can be produced and transmitted to the medium by applying a particular driving voltage signal. Further, in the context of this thesis, the atmospheric gas discharges will be often called plasma-based transducers or actuators to highlight their nature and difference from the conventional electroacoustic transducers. They can be classified into two distinctive categories by the dominating mechanism of interaction with the surrounding medium: hot-plasma and cold-plasma transducers.

2.1.1 Hot-plasma transducers

The transducers of this type involve an arc, streamer or high frequency discharge. These discharges form high density plasma regions or channels. As a result, due to intensive ionisation, recombination and other inelastic processes, most of the energy is lost into heat. The heat released in the discharge zone is further transferred to the surrounding gas. Local temperatures can reach thousands of degrees. Thus, the discharge is accompanied by an intensive glow. However, along with the past and present applications such as street lighting, welding and precise heating, these discharges are capable of manipulating the sound field [50, 51, 52, 53]. Indeed, modulation of the electrical current in the discharge produces the fluctuation of the heat release and its transfer. This causes the perturbation of the neutral gas density, which absorbs the power, and leads to the acoustic wave generation if the modulation is done in the audible frequency range. Typically, the discharge zone does not exceed a few centimetres in dimensions and acts as a point acoustic source.

2.1.2 Cold-plasma transducers

The most frequently used cold-plasma actuators are the dielectric barrier (DBD) and the corona type of discharge (CD). The common feature of such actuator types is the generation of so-called “ionic wind”. It constitutes a controllable movement of ions which interact with the neutral particles as a volumetric force. Close to the electrodes edges, in the zone of the most intensive ionisation, a heat release also takes place. The relative effect of the released heat and generated force on the medium depends on the discharge type and particular geometry [18, 54]. However, heat release is not a predominant mechanism, and the use of the actuators does not include any heating related applications. Hence, they are named cold.

The cold-plasma actuators are intensively studied in several research fields. Airflow control for aeronautic applications is one of them. High interest in a surface dielectric barrier discharge and surface corona discharge took place at the beginning of the 2000s. These actuators were studied to control a laminar-turbulent transition and a local drag reduction on the interface between solid media and airflow. This consequently attracted the strong attention of the aircraft industry. First, it was shown that both surface DBD and CD are capable of producing the airflow with velocities 0.1-10 ms in the area of several centimetres around the electrodes [55, 56]. The important aspect is that the air velocity is mostly induced in the region close to the surface, which belongs to the boundary layer. Therefore, the control of the transition from laminar to turbulent flow along the surface at low Reynolds numbers was studied [18, 57, 58]. As a consequence, an increase in the lift coefficient was observed when the surface discharge is mounted on the airfoil and subjected to the airflow [59, 58]. Moreover, flow laminarisation by the plasma actuators caused a new wave of research in the domain of aerodynamic noise reduction [60, 61, 62]. Ignition of the discharge on the surface of bluff bodies such as cylinders or aircraft wings has been shown to achieve a broadband noise reduction. DBD can also be applied for suppression of tonal noise created by the interaction between a cavity and the mean flow [63].

Another area of research relates to electrostatic propulsion. Since cold-plasma transducers are capable of generating volumetric forces acting on gas, they can be used as electrohydrodynamic thrusters, and pumps [64, 65, 66]. Due to the simplicity of construction and absence of moving parts, these actuators can be an interesting option to propel miniature objects and small aircrafts [67, 68, 69].

Finally, cold-plasma transducers can interact with the sound field. If an alternating signal is applied to the CD actuator along with the constant voltage difference that maintains the ionisation process, the sound waves are generated [70, 71, 72, 73]. The signal distortion can stay in reasonable bounds if an alternating signal is limited in amplitude [72]. DBD actuator was shown to generate the tonal signals at audible frequencies if a periodic signal is applied to its terminals [74].

2.2 Application to active sound control

As we saw in the previous paragraphs, plasma-based actuators present high interest in various engineering and research areas. What is particularly important for the work conducted in this thesis, all of them present physical mechanisms to interact with the acoustic field. The motivation of this work to develop a plasma-based transducer for active sound control is governed by their unique and distinctive property - interaction with the medium through a controllable ionised portion of initially the same medium. The absence of any intermediate moving mechanical parts facilitates the design and provides a fast acoustic response to an input electrical signal essential for real-time control. However, the application of some plasma transducers to sound control can present a considerable challenge. Hot-plasma transducers

clearly should not be placed close to the walls or objects due to the risk of the material overheating and damage. Moreover, as mentioned above, these discharges act as point acoustic sources, however, the most common active sound absorption methods require a surface distribution of sources over which the acoustic impedance can be controlled. On the contrary, cold-plasma transducers produce a moderate amount of heat that generally does not impact material integrity. In numerous examples from reviewed literature it can be seen, that these transducers can be arranged on any arbitrary surface and cover a certain area where the volumetric force can be generated. These qualities make such actuators preferable for active control applications. Therefore, dielectric barrier discharge and corona discharge principles can be potentially used in order to develop a dedicated to active sound control plasma-based actuator.

Electroacoustic transducers for active sound control have to obey most of the specifications for sound reproducing transducers. The signal distortion should be low in order to not generate higher harmonics while working with tonal noises. The transducer has to be able to generate the waves at audible frequencies, especially in the low frequency range up to several kilohertz, where most of the environmental noise is concentrated. Both DBD and CD actuators were shown to generate waves at frequencies around a few kilohertz. Relatively low distortion of some CD designs was also mentioned. However, there is no direct data available on the linearity of DBD transducers. The data from some studies indirectly indicates that the DBD actuators can produce higher harmonics along with the fundamental driving the electrodes [75, 61]. Thus, the physics of plasma formation in DBD actuators and its potential influence on the acoustic response should be investigated in more detail.

Dielectric barrier discharge

At atmospheric pressure with electrode gaps greater than approximately 1 cm, the discharge has a streamer form [76]. A streamer (microdischarge) is a thin ionised channel growing from a sharp electrode towards the other. Dielectric barrier discharge is one example of streamer discharges. The distinctive characteristic of a DBD is the separation of the electrodes by a solid dielectric material which does not allow a direct breakdown from one electrode to the other. As an example, let us consider a flat plate surface DBD (Figure 2.1).

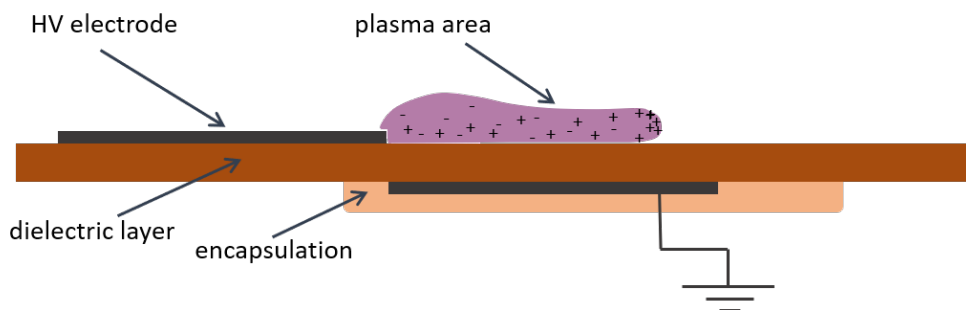


Figure 2.1: Schematic of a flat plate surface dielectric barrier discharge.

The actuator consists of 2 thin rectangular electrodes separated by a layer of dielectric material. To prevent plasma formation on the grounded electrode, the latter is commonly encapsulated. When a positive high voltage is applied to the upper electrode, electron avalanches appear in the area around the electrode edge. The electrons die on the anode leaving a cloud of positive space charge. The excited atoms provide energetic photons, which cause further photoionisation close to the positive cloud. New electrons that appear in the process are attracted to the anode. During their drift to the HV electrode, electrons excite atoms and mix with positive ions left from the primary avalanche forming quasi-neutral plasma. As a result, the positive volume charge (streamer head) shifts away from the electrode and leaves the quasi-neutral plasma behind (streamer body). Streamer formation and growth last approximately 10-50 nanoseconds [77]. A positive charge also covers the dielectric surface and then shields the external electrical field near the exposed electrode, which eventually stops the streamer development. After stopping, a few microseconds are needed for the electrical field to recover its breakdown value. Generally, many separated streamers develop simultaneously along the edge of the electrode. The length of the streamer does not exceed a few centimetres with applied voltage magnitudes of several kilovolts.

The DBD actuator can be powered in different ways. First, a high voltage pulse with a duration of 50-500 ns can be applied. During the pulse, only a single wave of streamers forms [77]. The pulse is repeated with a frequency of several kilohertz. Any other periodic high voltage signals such as sinusoids at audible frequencies can power DBD. In this case, during the half period of the signal, the number of microdischarges occur with time intervals of a few microseconds. The current signal consists of displacement current term and number of current pulses during the voltage rise and fall stages corresponding to the formation of microdischarges [78, 57]. Thus, the acoustic response to this signal should be principally different from the short pulse excitation. Two similar surface DBD prototypes were manufactured in order to assess this type of transducer.

The schematic of the prototypes is the same as in Figure 2.1. The prototypes are identical except for the dielectric material separating the electrodes: epoxy and ceramics were chosen to compare the influence of dielectric material on the response. First, the dielectric permittivity ϵ of epoxy and ceramic can impact plasma development. Second, the different stiffness of two dielectrics may affect the acoustic coupling between the actuator and the surrounding air. The electrodes are made of copper with a thickness of 50 μm . Kapton tape encapsulates the grounded electrodes. The length and width of electrodes are the same in both cases and equal to 90 mm and 10 mm, respectively. The high voltage and grounded electrodes are located in such a way that their edges are aligned vertically (as illustrated in Figure 2.1).

First, both DBD samples were powered with 200 ns duration and 8 kV in amplitude rectangular pulse signals at a frequency of 1 kHz. Then, a sinusoidal signal with an amplitude of 8 kV and 1 kHz frequency was supplied to the electrodes. The produced acoustic signals were recorded by the microphone at 1 m from the actuators. The time series of acoustic pressure and power spectral densities in the case of nanosecond pulse and sinusoidal excitation are presented in

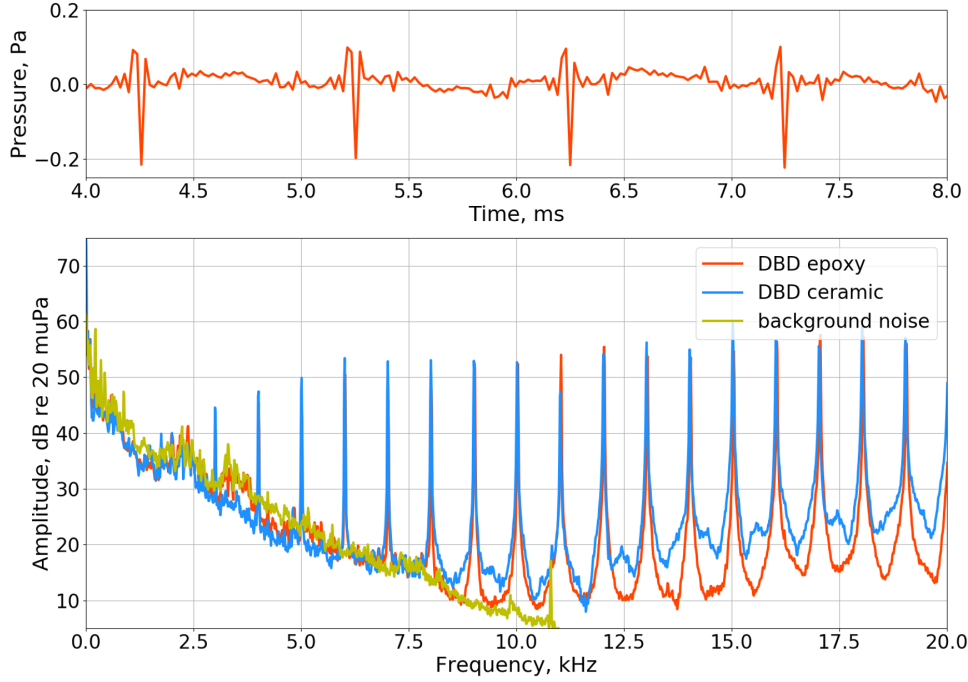


Figure 2.2: Time series of acoustic pressure signal and its power spectral density when DBDs are excited with 200 ns pulses with frequency 1 kHz and magnitude of 8 kV.

Figures 2.2 and 2.3.

In the case of nanosecond pulse excitation, the pressure pulses separated by 1 ms interval are clearly visible in the time series (Figure 2.2). On the power spectral density curve, the signal is represented by a set of harmonics with frequencies $F = n \times F_0, n \in \mathbb{Z}$, where the primary frequency $F_0 = 1$ kHz. The primary frequency and the first harmonic could be masked by external noise in the laboratory (see background line in Figure 2.2). Every voltage pulse induces a pressure shock wave that propagates in the air with a velocity close to the speed of sound in the air and is then detected by the microphone. The high amplitude of the shock wave is linked to the plasma development mechanism on the dielectric surface. As was already mentioned, in the case of nanosecond pulse excitation, only a single strong microdischarge forms and transfers part of its energy to the air volume. A rather different acoustic response can be obtained from DBD when excited with a sinusoidal signal (Figure 2.3). Although the voltage amplitude is the same as the nanosecond pulse, the time pressure signal does not contain any visible peaks since the microphone is not able to resolve the individual streamer response. As a result, a set of harmonics with lower amplitudes than in the first case is observed on the spectrum. As can be seen, the response of the actuator is indeed strongly nonlinear, which makes it inapplicable for the active control of sound. In the phase of the signal, when the voltage amplitude is low, the streamers are not generated. It means that the plasma is produced only during a portion of the period of a sinusoidal signal. With an understanding of the discontinuous dynamics of streamers, which constitutes the discharge, we can conclude

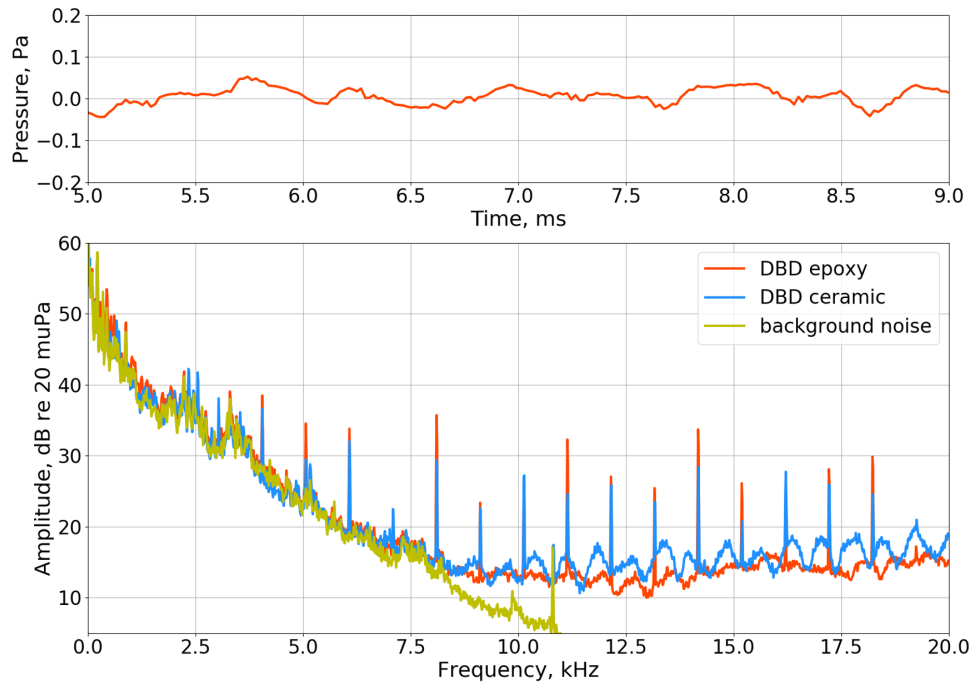


Figure 2.3: Time series of acoustic pressure signal and its power spectral density when DBDs are excited with AC sinusoidal signal at 1 kHz and magnitude of 8 kV.

that it cannot be used to reproduce continuous tonal signals needed for active sound control.

Although the acoustic responses are nonlinear, the nanosecond pulse excitation of a DBD transducer can still find some applications in acoustics. It provides triggered development of a microdischarge, which produces a sharp pressure pulse. This can be used as an acoustic trigger for measurements. The amplitude of such pressure shock wave and the interval between the pulses can still be controlled.

To sum up this section, the dielectric barrier discharge actuator cannot be employed for the active impedance control applications because of its inherent nonlinear response. The analysis continues with the physics and preliminary assessment of the CD-based actuator.

2.3 Corona discharge actuator

In this section, we discuss the mechanism of corona discharge operation and how the sound is produced. Then we discuss the shape of the voltage-current curve, which is a central element for analytical model development and will be referred to many times throughout the thesis. Finally, we make a choice on the polarity of the corona discharge based on the background acoustic noise level produced by the actuator.

2.3.1 Mechanism of corona discharge

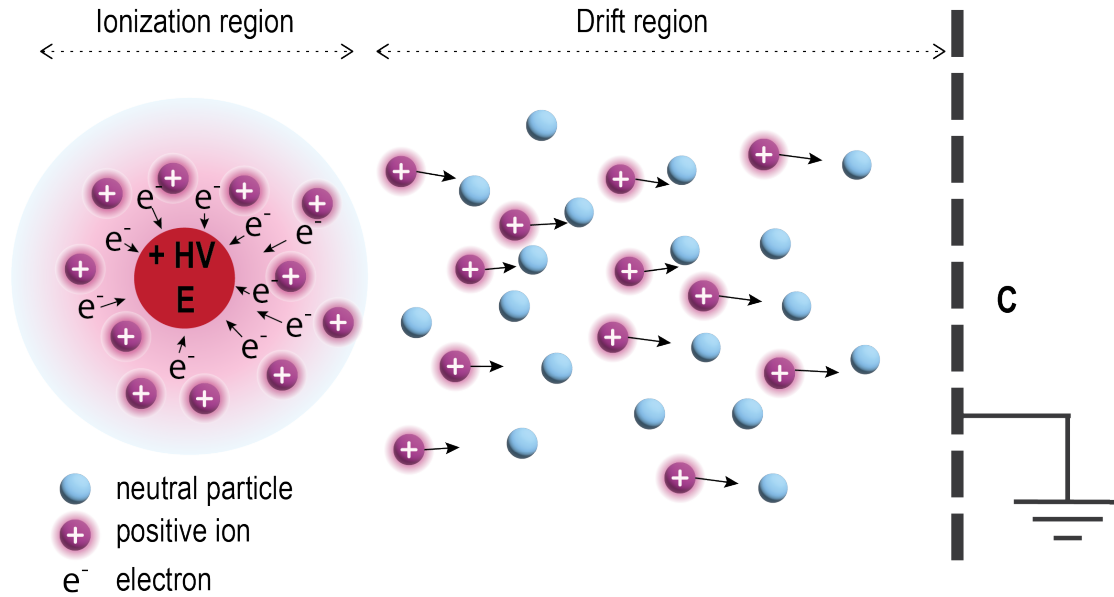


Figure 2.4: Mechanism of a positive corona discharge operation. The direction of movement of the charged particles is illustrated with arrows. E - emitter electrode, C - collector electrode. Schematic, not to scale.

A corona discharge actuator consists of two electrodes separated by an air gap. Its simplified mechanism of operation is illustrated in Figure 2.4. One of the electrodes (emitter, marked as E in Figure 2.4) is sharp with a small characteristic radius (in the range of 20 - 500 μm). It can be represented by a thin wire, needle or a sharp conducting edge. The other electrode (collector, marked as C in Figure 2.4) has larger dimensions with surfaces of considerably smaller curvature. For example, a metallic plate or a grid can be used. The air gap between the electrodes is also larger than the dimensions of the emitter. Such geometry allows establishing a corona type of discharge and improves its stability against arcing [18]. Here we discuss the mechanism of a positive corona discharge, but similar reasoning can be carried out in case of negative polarity.

If a positive constant high voltage (+HV) applied to the emitter increases and the collector electrode is connected to the ground, at some point, the electrical breakdown happens locally around the emitter, starting the ionisation process. The thickness of this ionisation region is of the order of the emitter radius and increases with applied voltage. Indeed, the electrical field magnitude close to the emitter electrode changes as $1/r$, with r being a distance from the emitter centre [79]. Therefore, it can exceed the breakdown threshold of approximately $3.1 \cdot 10^6 \text{ V/m}$ in air, although staying well below this value in most of the volume between the electrodes. The produced electrons are attracted by the emitter. Thus, the ionisation region accumulates a positive space charge. Then, positively charged ions drift towards the collector electrode in the external electric field. As the magnitude of the electric field in the

drift region is lower, the gained energy is not sufficient for further ionisation. As a result, the ions transfer their momentum in elastic collisions with neutral particles, which dominate in the interelectrode volume. Each ion transmits its energy thousands of times over a several millimetre path, since a mean free path in the air at atmospheric pressure is in the order of 100 nanometres. This process can be considered as an effective volumetric force that acts on neutral air. Finally, this force induces an airflow with velocities in the range of 0.1-5 m/s [80, 81]. The interesting feature of this flow is its homogeneity and low turbulence due to the absence of moving parts in the actuator in contrast to conventional fans [82, 83]. The speed of the airflow depends on the voltage difference on the electrodes.

2.3.2 Sound generation with corona discharge

Along with the constant voltage U_{DC} , one can apply a sinusoidal voltage at frequency ω with amplitude u_{AC} . The resulting signal has a form $U(t) = U_{DC} + u_{AC} \sin(\omega t)$. The alternating voltage component creates the fluctuation of the electric field, which, in turn, causes the change in the force acting on the air. It changes the velocity of the airflow that finally produces the sound waves. Alternatively, the ionisation region constantly releases heat due to inelastic processes. The variation in the mean electric field changes the volume of the ionisation region and, therefore, the amount of released heat, which finally acts as a second sound source in the discharge. However, since the ionisation volume is much smaller than the volume of the drift region, the heat sound source is weaker than the one from the fluctuation of the volumetric force. The ratio of sound pressure levels produced by the force-based and heat-based acoustic source depends on the particular actuator geometry, as was discussed earlier. From an acoustic viewpoint, the heat release conforms to a monopolar source. The volumetric force corresponds to a dipolar source and can be imagined as an intangible, transparent for air particles membrane. One important observation is that the position of these two sources does not coincide: the heat source is concentrated around the high voltage electrode, and the centre of the force source is located in the middle between the electrodes. However, in the actuator, which is designed in this thesis, the interelectrode distance is only 6 mm, so the location mismatch of 3 mm should not be noticeable at frequencies up to several kilohertz and will be verified further.

2.3.3 Voltage-current characteristics

Figure 2.5 illustrates the typical voltage-current characteristic of a corona discharge showing the averaged electrical current depending on applied constant voltage. It should be mentioned that the CD's current is composed of high frequency pulses with a nonzero mean value named after Trichel [84, 85]. The frequency of the pulses lays in the low MHz range and highlights more complex phenomena in the ionisation region than discussed in Section 2.3.1. Fortunately, for the active sound control applications, which stay well below this frequency range, we will consider the CD actuator as a constant current glow discharge.

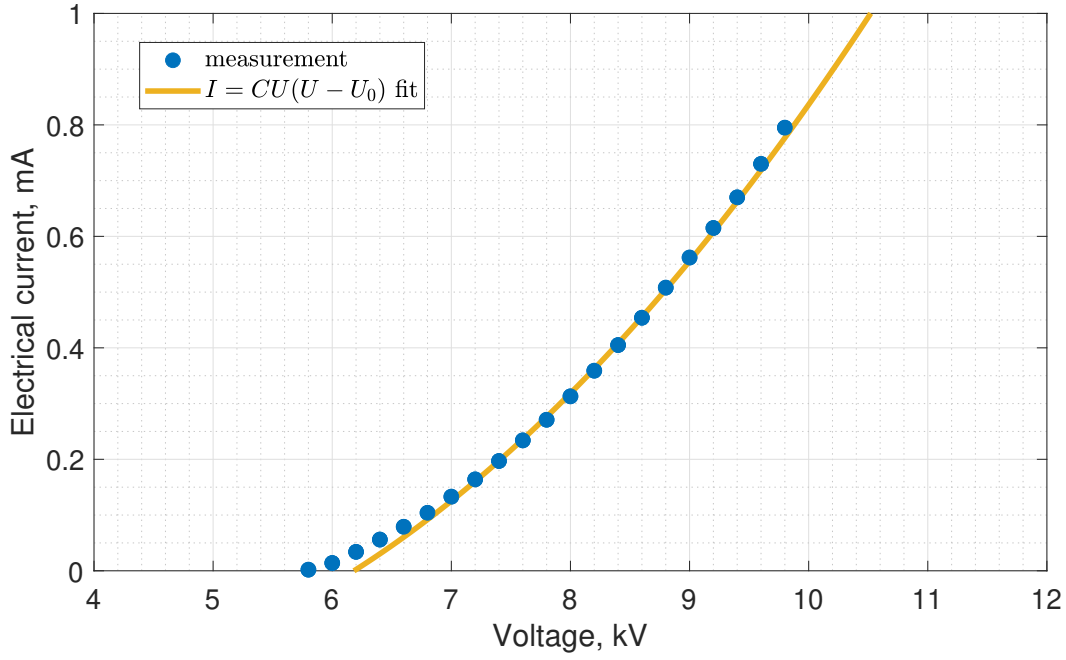


Figure 2.5: Voltage-current characteristics of a corona discharge actuator in a wire-to-mesh geometry measured experimentally and its approximation with a Townsend formula.

At low voltages, the electrical field magnitude does not exceed the breakdown value even in the vicinity of the emitter electrode. As a result, no plasma can be produced, and the discharge current is zero. The voltage U_0 , at which the electrical current appears, indicating the initiation of the discharge, is called the onset voltage of corona discharge. On the other side, too high voltage leads to an electrical arc between the electrodes. In this case, the electrical field exceeds the breakdown value in the drift region and shorts the electrodes with a conducting plasma channel, which can finally damage the thin emitter electrode. In practice, the electrical arc happens at lower voltages than in theory because of the presence of various microscopic surface defects on the electrodes, which create a local high electrical field regions. Therefore, corona discharge exists in a well-defined voltage range, between the state with no plasma and a transition to an electrical arc.

The cumulative electrical current in corona discharge has a nonlinear dependence on the applied voltage. Townsend analytically showed for coaxial geometry of a corona discharge (high voltage wire in the centre of a cylindrical collector) that the current-voltage characteristics follows the law [86]:

$$I = CU(U - U_0). \quad (2.1)$$

In Equation (2.1), C is a dimensional constant depending on the actuator geometry (inter-electrode distance, emitter curvature, etc.) and gas parameters (static pressure, ion mobility, etc.). Later it was shown empirically that Townsend's formula (2.1) approximates well voltage-current curves of corona discharges with various geometrical configurations of electrodes [76]. Figure 2.5 illustrates Equation (2.1) approximating a voltage-current characteristics of a corona discharge in a wire-to-mesh geometry. It suggests the quadratic evolution of current with respect to the applied voltage and its vanishing at voltages below U_0 . Various polynomial and more complex empirical formulas were suggested in the literature to describe more precisely the voltage-current evolution in particular geometries [87, 88, 89]. However, Townsend's formula captures well the nonlinear nature of the voltage-current relation with a low order polynomial, including the approximation of the onset voltage, and thus, containing the most necessary information from the curve. For these reasons, Townsend's formula (2.1) will be used in this work to analytically describe a voltage-current characteristics.

2.3.4 Positive versus negative corona discharge

The same CD actuator can be powered with both positive and negative polarities of high voltage. Different types of charged particles traverse a drift region in two cases: positive ions at positive polarity; negative ions with electrons at negative polarity. Both polarities are often used in the reviewed literature. This allows us to identify which polarity of the transducer is more suitable from the viewpoint of sound reproduction and sound control.

When a constant high voltage is applied to the emitter electrode, the discharge produces low intensity but still audible broadband noise. To compare the noise levels, the following measurement is carried out. A constant DC voltage $U_{DC} = \pm 8.2$ kV is applied to the actuator along with a sinusoidal waveform u_{AC} at frequency 1 kHz. The u_{AC} magnitude (200 Vrms for positive and 150 Vrms for negative polarities) is adjusted in order to match the sound pressures at the tested frequency of u_{AC} . The CD actuator used for this experiment is described further in Section 3.2. The measurement is carried out in the anechoic chamber with a low noise level. The microphone is placed at 1 m from the actuator on the axis of symmetry.

The sound pressure spectra obtained for positive and negative polarities of a corona discharge are shown in Figure 2.6. Additional data showing the octave integrated noise without a sinusoidal signal is presented in Figure B.1 in Appendix B. The sharp low amplitude peaks starting at frequency 150 Hz are visible on both spectra as well as on the reference noise signal and relate to the electrically induced noise. One can see that although the main frequency and its higher harmonics have similar magnitudes, the noise floor is significantly higher across the whole frequency range in case of negative corona discharge. The difference is slightly higher at lower frequencies of measured spectra, which are of the most importance for active sound control. Since a microphone is required to be placed closely in front of the actuator in most of the active control methods [90, 91], the stability of the system can be affected by the additional noise. Therefore, positive polarity is a preferred mode of the CD operation.

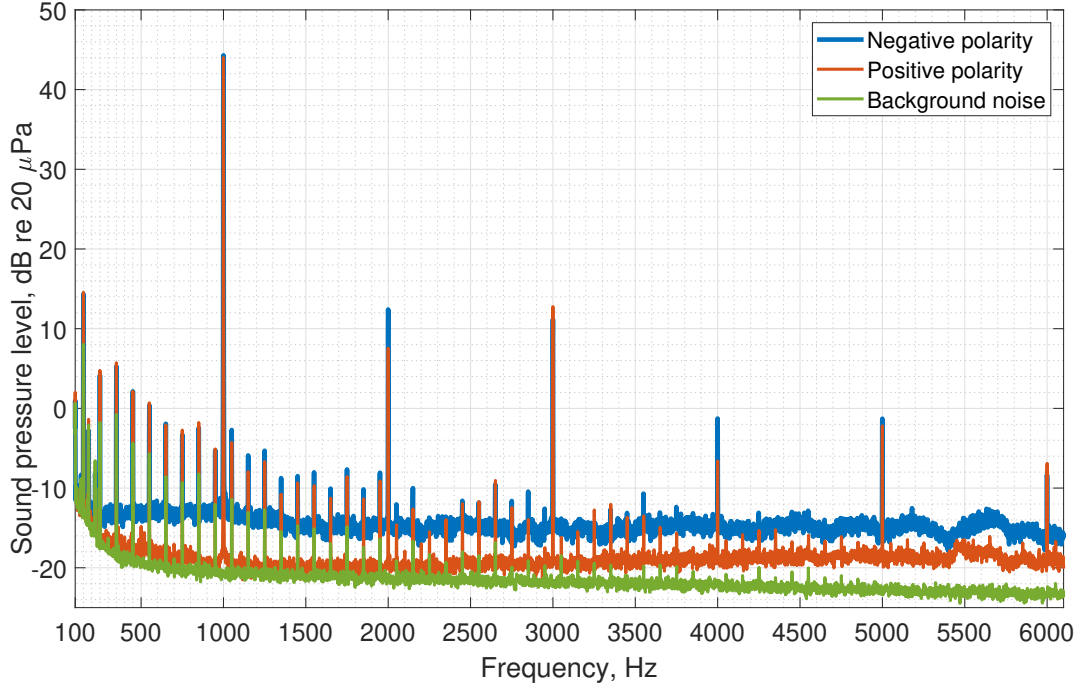


Figure 2.6: Sound pressure spectra of a corona discharge actuator powered with positive and negative polarity. Constant voltage level $U_{DC} = \pm 8.2$ kV, alternating sinusoidal voltage component u_{AC} equals to 200 Vrms for positive polarity, 150 Vrms for negative polarity at frequency 1 kHz. Background noise - the actuator is not powered.

2.4 Conclusions

After the review of existing hot- and cold-plasma transducers, the dielectric barrier and corona type of discharges were identified as the most optimal candidates for sound control applications. The reasons for this choice are the non-thermal effects prevalent in the sound generation process, and the possibility to organise a discharge on an extended area. Therefore, the closely placed objects would not be exposed to considerable heat, and the particle velocity can be controlled over a relatively large surface.

The manufactured simple DBD actuators were powered with different periodic signals. The nanosecond pulsed signal evidently cannot lead to a single tone sound spectrum, but it confirms from an acoustic viewpoint the streamer nature of the discharge. A fast propagating plasma channel generates an acoustic shock wave that is recorded as a short pressure pulse. Thus, the AC applied signal does not transform in the linear spectrum because the signal consists of many low amplitude pulses, non-distinguishable in the time domain pressure signal. The discharge could be potentially modulated at high frequencies (≈ 200 kHz) in order to maintain a constant plasma layer [92], but it would lead to inadequately high power consumption and heating, basically transitioning it to the hot-plasma actuators.

Corona discharge is a constant current discharge that allows providing a continuous interaction with surrounding air in contrast to discrete streamers in the DBD. The airflow created by the ions pushing the neutrals, together with some heat release in the ionisation region, can be modulated to produce sound. The actuator has visibly lower signal distortion and will be assessed in the next chapters. The lower background noise in the positive corona discharge defines the choice of polarity. Therefore, a positive polarity CD actuator is evaluated as the most suitable for the sound control application. The work continues with this type of discharge.

3 Development of corona discharge actuator for sound control

3.1 Introduction

This chapter investigates a positive corona discharge actuator built in a wire-to-mesh geometry. A simple but efficient analytical model is proposed to describe the acoustic sources of a corona discharge and calculate its far field acoustic response. For more insights on the physics of the electrical field and space charge distribution, as well as more accurate frequency response calculation, a finite element model for a CD actuator is proposed. Thanks to it, we optimise the prototype geometry, which is used later in most of the experiments throughout the work.

The chapter contains some of the material published in the following paper:

Sergeev, S., Lissek, H., Howling, A., Furno, I., Plyushchev, G., and Leyland, P. (2020). Development of a plasma electroacoustic actuator for active noise control applications. *Journal of Physics D: Applied Physics*, 53(49), 495202.

3.2 Geometry of the corona discharge actuator

The majority of studies investigate the corona discharge in a point-to-plane or point-to-grid configuration. The interelectrode distance does not exceed 20 mm. This constrains the transverse discharge dimension to the same order of magnitude. It happens because the ions tend to follow the electric field lines, which are concentrated in the region with the shortest distance between electrodes. Such a discharge resembles a point acoustic source up to high frequencies. However, for active sound control, a surface-distributed source would be preferable to control an acoustic plane. This can be achieved by manufacturing a two-dimensional array of points connected to the same potential as was done in the work of Matsuzawa [70]. One can understand that such an assembly is rather challenging to fabricate in order to keep all the points equidistant and maintain the same distance from the collector

electrode, otherwise the discharge can be more concentrated at a particular location and lead to early arcing.

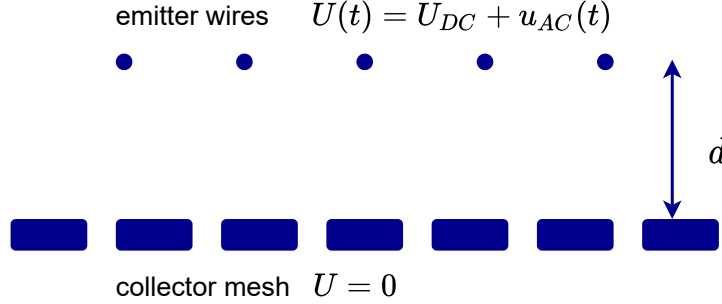


Figure 3.1: Schematic view of a CD actuator in a wire-to-mesh geometry. Not to scale.

In this study, we work with a wire-to-mesh design of the CD actuator. This geometry is schematically illustrated in Figure 3.1. The emitter electrodes are represented by a group of thin wires strung parallel to each other and the collector grid. It is relatively simple to maintain the exact distance between the emitter plane and the collector electrode by tensioning the wires and stretching them over an arbitrary surface. Although having the set of electrodes charged to the same high voltage potential leads to the reduction of maximal electrical field around the emitter and subsequently higher onset voltage, this geometry presents several advantages. The electric field in the drift region has a more uniform distribution with a strong normal component from the plane of corona wires to the collector. It can be approximated as the field in a parallel plate capacitor. Such an assumption simplifies the analytical description of the discharge. Furthermore, the flow velocity and acoustic particle velocity are expected to have similar magnitude all over the surface of the electrodes and be directed normally to it, which is not the case for a single corona wire setup [93]. This is particularly important for impedance control techniques where the normal velocity is typically controlled as a function of the sound pressure.

3.3 Analytical model for sound sources in corona discharge

A physical model of a transducer allows predicting its radiation properties without performing the actual measurements. It can also be needed to optimise control approaches. In this section, we develop an analytical model that can describe the far field low frequency electroacoustic behaviour of the CD actuator in the geometry, illustrated in Figure 3.1.

Several analytical electroacoustic models for corona discharge actuator can be found in literature [71, 70, 94, 72, 73]. The early work of Matsuzawa [70] considers the volumetric force as the only acoustic source due to its dominance. The works by Bequin [94, 72] demonstrated that a heat release also plays a non-negligible role in the sound radiation and included both sources in the model. However, to adjust all the unknown model parameters, the directivity

patterns measurements should be performed with a CD actuator, which presents a non-trivial task without a dedicated equipment. Here, we propose a simple macroscopic description of a corona discharge with force and heat acoustic sources. Setting all necessary coefficients only requires a measurement of the voltage-current discharge characteristics that is relatively simple to perform.

3.3.1 Governing equations

The gas in most of the volume of a CD actuator is weakly ionised (degree of ionisation lower than 10^{-3}). Thus, we can describe the neutral gas in the volume between the electrodes, neglecting the influence of plasma on the gas parameters. Ions can be indirectly included into consideration as the external force and energy source interacting with neutral gas [95]. The mass conservation can be written as:

$$\frac{\partial \delta}{\partial t} + \rho_0 \nabla \cdot \mathbf{u} = 0, \quad (3.1)$$

where $\delta = \rho - \rho_0$ is the variation of neutral gas mass density, and \mathbf{u} is the particle velocity. Since the explicit presence of ions is neglected, the ionisation and recombination processes changing the density are not considered.

Most of the energy from ions to the neutral air particles is transferred through elastic collisions in the drift region [76]. It can be described as a volume averaged force acting on the neutral air. Then, the Newton's equation takes the form:

$$\rho_0 \frac{\partial \mathbf{u}}{\partial t} + \nabla p = \mathbf{f} \quad (3.2)$$

In Equation (3.2) $p = P - P_0$ is a variation of pressure over the static value P_0 , which corresponds to the acoustic pressure in our case, \mathbf{f} is the mechanical force from ions per unit volume.

Heat release is considered as an injection of energy into the volume between the electrodes. It can be integrated as a source in the energy balance equation:

$$\rho_0 T_0 \frac{\partial s}{\partial t} = h, \quad (3.3)$$

where T_0 is a static gas temperature, $s = S - S_0$ - change of entropy per unit mass, h - heat power per unit volume.

The set of equations (3.1), (3.2), (3.3) is closed with the equation related to the gas properties. Assuming an ideal gas with adiabatic transformation the relation between density, pressure, and entropy writes:

$$\delta = \left(\frac{\partial \rho}{\partial P} \right)_s p + \left(\frac{\partial \rho}{\partial S} \right)_p s = \frac{1}{c^2} p - \frac{\rho_0}{C_p} s, \quad (3.4)$$

where C_p is the heat capacity at constant pressure per unit mass, c is the speed of sound in the gas. The system of four equations allows deriving the wave equation for pressure:

$$\frac{1}{c^2} \frac{\partial^2 p}{\partial t^2} - \nabla^2 p = \frac{\gamma - 1}{c^2} \frac{\partial h}{\partial t} - \nabla \cdot \mathbf{f}. \quad (3.5)$$

In Equation (3.5) γ is the specific heat ratio (taken as 1.4 for air). In the frequency domain the wave equation takes the form:

$$(k^2 + \nabla^2) p = \frac{-j\omega(\gamma - 1)}{c^2} h + \nabla \cdot \mathbf{f}, \quad (3.6)$$

where $k = \omega/c$ is the wave number, $j = \sqrt{-1}$. As was discussed in 2.3.1, the heat and force sources are not exactly collocated in the discharge. Nevertheless, the distance between the electrodes does not exceed a few millimetres. Placing both sources at the centre of coordinates in the analytical model cannot affect the pressure dynamics at low frequencies. The solution of the wave equation in the frequency domain with the CD actuator centred at position \mathbf{r}_0 can be expressed as:

$$p(\mathbf{r}) = \iiint [\Phi(\mathbf{r}_0) - \nabla \cdot \mathbf{f}(\mathbf{r}_0)] g(\mathbf{r}|\mathbf{r}_0) d\nu_o, \quad (3.7)$$

with

$$\Phi(\mathbf{r}_0) = -j\omega \frac{\gamma - 1}{c^2} h. \quad (3.8)$$

In Equation (3.7) g denotes the free space Green's function. The solution of this equation is non-zero only in the discharge volume ν_o where the sources exist. The monopolar term Φ describes a sound source in the centre of the discharge with heat power density h . The second term in Equation (3.7) represents the dipolar acoustic source created by the force vector \mathbf{f} . By the superposition principle, we can find the sound pressure field generated separately by heat

and force sources. Assuming a small source region compared to a wavelength, the heat p_h and force p_f pressures are derived accordingly:

$$\begin{aligned} p_h(\mathbf{r}) &= -\frac{j\omega(\gamma-1)}{4\pi|\mathbf{r}|c^2} \left(\int \int \int h d\nu_o \right) \exp(jk|\mathbf{r}|), \\ p_f(\mathbf{r}) &= -\frac{jk}{4\pi|\mathbf{r}|} \left(\frac{j}{k|\mathbf{r}|} + 1 \right) \left(\int \int \int f d\nu_o \right) \cos\theta \exp(jk|\mathbf{r}|). \end{aligned} \quad (3.9)$$

In the expression of p_f in Equation (3.9), θ is the angle between the force vector and direction of observation. It is assumed here, that \mathbf{f} has the same direction (from emitter plane to collector plane) in the whole interelectrode volume. The total sound pressure in Equation (3.7) is the sum of the two terms in Equation (3.9): $p(\mathbf{r}) = p_h(\mathbf{r}) + p_f(\mathbf{r})$.

3.3.2 Force and heat sources

The integrals in these expressions designate the cumulative force and heat power produced in the discharge. Let us denote them $F_\omega = \int \int \int f d\nu_o$ and $H_\omega = \int \int \int h d\nu_o$, where the subscript ω expresses a function in the frequency domain. We can consider these quantities in the time domain in order to obtain their estimations. The cumulative heat power being released in the discharge at a time moment t , can be approximated by its upper bound as the power that goes to Joule losses: $H(t) \approx U(t)I(t)$, where $U(t)$ and $I(t)$ are the applied voltage and total current in the CD actuator. The current can be expressed as a function of applied voltage using Townsend's approximation $I = CU(U - U_0)$ of the voltage-current characteristics (see Section 2.3.3). Then, the heat power writes:

$$H(t) = U(t)I(t) = CU(t)^2(U(t) - U_0). \quad (3.10)$$

The applied voltage is the sum of the constant and alternating components $U(t) = U_{DC} + u_{AC}(t)$ with the latter one in the form of a harmonic oscillation $u_{AC}(t) = u_{AC} \exp(j\omega t)$. With this formulation of voltage $U(t)$, the heat power can be broken down into a constant and time dependent terms:

$$\begin{aligned} H(t) = C[U_{DC}^2(U_{DC} - U_0) + (3U_{DC}^2 - 2U_{DC}U_0)u_{AC}(t) + \\ + (3U_{DC} - U_0)u_{AC}^2(t) + u_{AC}^3(t)]. \end{aligned} \quad (3.11)$$

The first component in Equation (3.11) represents a constant power that is injected into the discharge volume if the actuator is biased with a voltage U_{DC} . It has the greatest magnitude but

does not participate in sound generation. The other terms depict the functions that vary with frequencies ω , 2ω , and 3ω . The linear component with magnitude $C(3U_{DC}^2 - 2U_{DC}U_0)u_{AC}$ is responsible for sound generation. The higher order terms introduce distortion to the signal. The magnitudes of the heat source components can be written in a following way:

$$\begin{aligned} H_\omega &= C(3U_{DC}^2 - 2U_{DC}U_0)u_{AC} = 3CU_{DC}^3 \left(1 - \frac{2}{3} \frac{U_0}{U_{DC}}\right) \frac{u_{AC}}{U_{DC}} \\ H_{2\omega} &= C(3U_{DC} - U_0)u_{AC}^2 = 3CU_{DC}^3 \left(1 - \frac{1}{3} \frac{U_0}{U_{DC}}\right) \left(\frac{u_{AC}}{U_{DC}}\right)^2 \\ H_{3\omega} &= Cu_{AC}^3 = CU_{DC}^3 \left(\frac{u_{AC}}{U_{DC}}\right)^3. \end{aligned} \quad (3.12)$$

We can estimate their relative magnitudes. In a typical regime of corona discharge operation, U_{DC} is 1.5 times higher than the onset voltage U_0 . If the alternating component amplitude u_{AC} does not exceed 5 % of U_{DC} , the term of the second order is 15 times weaker than the linear one. This corresponds to the sound pressure level of the second harmonic 18 dB lower than the main tone. The third order source term is 670 times weaker than the main and can be considered negligible. If bias voltage is much higher than the onset voltage ($U_{DC} \gg U_0$), the ratios of the magnitudes can be seen directly from Equations (3.12):

$$\frac{H_{2\omega}}{H_\omega} \approx \frac{u_{AC}}{U_{DC}}, \quad \frac{H_{3\omega}}{H_\omega} \approx \frac{1}{3} \left(\frac{u_{AC}}{U_{DC}}\right)^2. \quad (3.13)$$

A more detailed study of the CD's harmonic distortion is presented in Section 4.6. Nevertheless, it is a rather acceptable level in the view of active control applications. Thus, only the linear term will be taken into account in the analytical model to estimate p_h , which writes as:

$$H_\omega = C(3U_{DC}^2 - 2U_{DC}U_0)u_{AC}. \quad (3.14)$$

The volumetric force, which describes the transfer of mechanical momentum from ions to the neutral air in the drift region, is represented by the Coulomb force. It acts on the ions from the electric field $\mathbf{f} = \rho_i \mathbf{E}$ (ρ_i is the density of positive ions, and \mathbf{E} is the electric field). The force is directed from the high voltage wires plane normal to the collector plane as the electric field vector. The current density magnitude in the drift region can be written as $J = \mu_i \rho_i E$, where μ_i is the mobility of positive ions. Here we assume that all the ions produced in the discharge constitute an effective mass of particles with +1 charge and properties described by effective mobility μ_i . Thus, the cumulative force F reads:

$$F = \int \int \int \rho_i E d v_o = \int \int \int \frac{J}{\mu_i} d v_o = \frac{I d}{\mu_i} \quad (3.15)$$

Here d is the interelectrode distance. The integration of the current density over the discharge area is substituted by the total current I . The following derivation is identical to the heat power term. The current in Equation (3.15) is expressed through the voltage using Townsend's voltage-current relationship. Separating the constant and time-dependent terms yields:

$$F(t) = \frac{C d}{\mu_i} [(U_{DC} - U_0) U_{DC} + (2U_{DC} - U_0) u_{AC}(t) + u_{AC}^2(t)]. \quad (3.16)$$

The first term represents a constant force that leads to a steady airflow generation, if the actuator is not enclosed. Its magnitude depends on the bias voltage U_{DC} . The time-dependent terms present only linear and second order components. They can be rewritten in a similar way as the Equation (3.12):

$$\begin{aligned} F_\omega &= \frac{C d}{\mu_i} (2U_{DC} - U_0) u_{AC} = 2 \frac{C d}{\mu_i} U_{DC}^2 \left(1 - \frac{1}{2} \frac{U_0}{U_{DC}} \right) \frac{u_{AC}}{U_{DC}} \\ F_{2\omega} &= \frac{C d}{\mu_i} u_{AC}^2 = \frac{C d}{\mu_i} U_{DC}^2 \left(\frac{u_{AC}}{U_{DC}} \right)^2. \end{aligned} \quad (3.17)$$

Under the same operational conditions, as discussed for the heat power ($U_{DC} = 1.5U_0$, $u_{AC} = 0.05U_{DC}$), the magnitude of the nonlinear component appears to be 25 times smaller, than the one for the main harmonic (results in 23 dB lower sound pressure level). Under assumption ($U_{DC} \gg U_0$) the ratio of second harmonic to the main one becomes:

$$\frac{F_{2\omega}}{F_\omega} \approx \frac{1}{2} \frac{u_{AC}}{U_{DC}}. \quad (3.18)$$

It means that the force related sound pressure p_f introduces even lower harmonic distortion than p_h . Finally, the linearised force amplitude in the frequency domain is written as follows:

$$F_\omega = \frac{C d}{\mu_i} (2U_{DC} - U_0) u_{AC}, \quad (3.19)$$

The derived expressions (3.14) and (3.19) for heat power and force generated in a wire-to-mesh

CD actuator can be implemented in Equations (3.9) in order to estimate the far-field acoustic behaviour of the discharge, which includes frequency response and directivity patterns. This formulation also allows assessing the level of distortion produced by the actuator. To get the values of all necessary parameters for the model, such as the dimensional constant C and the onset voltage U_0 , only a simple measurement of the voltage-current characteristics is needed. Effective ion mobility μ_i can be found in the literature for a given air humidity level [96]. Various acoustic characteristics of the CD actuator will be assessed using the proposed analytical model in the next chapter and compared with experimental data. This description of the force and heat sources can also be used to implement an active control approach based on the transducer model. Further, the numerical electroacoustic model of the CD transducer is developed.

3.4 Numerical model for a corona discharge design

Most of the studies related to the electroacoustic investigation of corona discharge actuators are either entirely experimental or provide a theoretical characterisation of the sound generation process. The authors report measured pressure frequency responses and applied voltage and current signals. However, the particle velocity or pressure can be of high interest in the vicinity of the electrode system in order to characterise the acoustic impedance at the collector plane. Since the actuator has no moving parts like a membrane, this task is not trivial. Moreover, the acoustic velocity is biased by the presence of constant flow. Particle image velocimetry could be potentially applied to extract the acoustic component [97, 98]. However, the technique is rather complicated to set up, it requires post-processing and mostly resolves only high acoustic wave amplitudes. Electrical field measurements are another problem that is difficult to tackle experimentally. The presence of a probe in the ionised gas disturbs the distribution of particles and changes the actual vector field. Analytical models typically describe the far field acoustic behaviour of the CD actuator. The electrical field, potential, and charged particles distributions between the electrodes cannot be accurately estimated, as they strongly depend on a particular actuator geometry, which is often simplified in theory. Therefore, numerical modelling of a corona discharge coupled with acoustics presents an alternative solution to the abovementioned problems. The actual geometry of the transducer can be taken into account in much greater detail. Moreover, the possibility to change one parameter without influencing the rest allows conducting parametric studies, which are less uncertain and faster than the fully experimental approach. The numerical simulation can provide valuable insights on the electrical parameters of the interelectrode zone. Although some works targeted to simulate the noise produced in coronating high voltage lines [99], to our knowledge, there is no numerical approach proposed to model the sound generation in a biased corona with alternating voltage applied to the emitter.

This section provides a transient simulation of the electrical and acoustic behaviour of the corona discharge actuator when it is supplied with a voltage signal in the form $U(t) = U_{DC} + u_{AC}(t)$. First, the electrical potential field is computed. The movement of charged particles

between the electrodes is taken into account. Then, the model is coupled with the acoustic environment, where the sound sources are taken from the electrical model. The induced constant airflow could also be calculated. However, as discussed in the previous section, the velocities do not exceed several meters per second and cannot influence the sound generation process noticeably. Since the main focus of the simulation is electroacoustic modelling, the constant flow is not considered. If a precise distribution of static pressure and airflow velocity is required, a sub-simulation can be performed as a separate stationary problem. The physics of the ionisation region is quite complex and can lead to unacceptable computational time in a time-dependent study if taken into consideration. Moreover, the region is negligibly small compared to the interelectrode distance. Instead, its size is assumed to be zero in the model. To model the rest correctly, the positive ions are explicitly injected from the high voltage electrode, which was shown to be a good compromise to complete modelling of plasma physics [82, 93, 100, 101].

3.4.1 Electrostatics modelling

The governing equations for the electrostatic problem characterise the electric potential V and concentration of the positive particles ρ_i . The distribution of electric potential provided by the Poisson equation:

$$\nabla \cdot (-\epsilon_0 \epsilon_r \nabla V) = \rho_i, \quad (3.20)$$

In Equation (3.20), ϵ_0 is the electrical permittivity in vacuum, ϵ_r the relative electrical permittivity of the medium (for air $\epsilon_r = 1$). The electric field vector is defined as the gradient of the electric potential $\mathbf{E} = -\nabla V$. The model considers a single type of ions with a charge number +1 because these species constitute most of the space charge in a positive corona. The current density \mathbf{J} can be expressed in the drift-diffusion form:

$$\mathbf{J} = \mu_i \mathbf{E} \rho_i - D_i \nabla \rho_i. \quad (3.21)$$

In Equation (3.21), the first part describes the drift of ions in the electric field with their effective mobility μ_i , which is assumed constant in the whole discharge volume. Its value is taken from available experimental data for a given gas (data from [96] is used for the following simulation) with respect to actual humidity and static pressure. The second component takes into account the diffusion of particles. D_i is the averaged ion diffusion coefficient ($5 \times 10^{-5} \text{ m}^2/\text{s}$ in the air). This term, finally, is not taken into account in the simulation as its magnitude is several orders lower than the drift term. The system of equations (3.20) and (3.21) is completed by the charge conservation equation:

$$\nabla \cdot \mathbf{J} = 0. \quad (3.22)$$

Boundary conditions

The boundary conditions are the following. The time-dependent high voltage signal is applied to the corona discharge electrodes. The collector electrode is connected to zero potential. The space charge density should also be specified on the electrodes since the ions are explicitly introduced in order to not model the breakdown and ionisation processes. For this purpose, an assumption on the HV electrode is made. It was first introduced by Kaptsov [102]. The lowest voltage at which the corona discharge initiates, or the onset voltage U_0 , corresponds to the critical magnitude of the electrical field E_c on the surface of the emitter electrode. The hypothesis states that if the voltage exceeds the onset voltage, the electric field magnitude at the electrode remains equal to E_c . This assumption lets us choose the correct space charge density ρ_i as a boundary condition on the corona electrode at a given voltage $U(t)$ so that the electrical field always equals E_c . The critical value E_c in dry air can be calculated according to Peek's semi-empirical formula [103]:

$$E_c = 3.1 \cdot 10^6 \delta \left(1 + \frac{3.08 \cdot 10^{-2}}{\sqrt{\delta R}} \right) [\text{V/m}]. \quad (3.23)$$

In this formula, R is the radius of curvature of the emitter electrode, δ is a parameter, accounting for the changes in the static pressure and temperature. For normal conditions $\delta = 1$. Initially, expression (3.23) was obtained for the coaxial cylindrical geometry of the electrodes but later was proven to be valid with slight adjustments in coefficients for other configurations, including wire-to-mesh and wire-to-plate [76, 93, 82]. If the surface of the electrode is not perfectly smooth in the experiment, the E_c value decreases. The recent works demonstrate that the critical field strongly depends on the relative air humidity [104]. Finally, we use the magnitude of the critical field reduced by 25 %, because the experimental measurements to assess the performance of the numerical model were carried out with relative humidity of 58%.

The voltage applied to the actuator is time-dependent. Thus, the space charge density should vary accordingly in order to satisfy Kaptsov's hypothesis at every time step. It means that the space charge density can be represented as a function of applied voltage $\rho_i(U(t))$ for a given geometry. To obtain this relationship, numerous stationary studies are performed applying different constant voltages to the actuator. Then the data is interpolated to cover the whole range of $U(t)$ variation. To sum up, the boundary condition of the space charge on the corona wires is a function $\rho_i(U(t))$ satisfying Kaptsov's assumption, and zero at the grounded collector electrode.

3.4.2 Acoustics modelling

To model the acoustic behaviour of the discharge, the wave equation is solved. It has a form similar to Equation 3.5:

$$\frac{1}{c^2} \frac{\partial^2 p}{\partial t^2} - \nabla^2 p = \frac{\gamma - 1}{c^2} \frac{\partial h}{\partial t} - \nabla \cdot \mathbf{f}. \quad (3.24)$$

The heat power density is defined as a Joule power loss $h = \mathbf{J} \cdot \mathbf{E}$. The force density is included in the model as the Coulomb force $\mathbf{f} = \rho_i \mathbf{E}$. The significant difference between the numerical model and the analytical one is that both force and heat sources are considered space-dependent variables. They use the distributions of electrical current density, electrical field, and space charge density from the solution of Equations (3.20)-(3.22). As a result, we can benefit from a better precision of sources estimation, which better reflects the actuator's geometry.

The boundary conditions for the acoustic study are straightforward. The electrode surfaces are treated as the sound rigid boundaries (zero velocity). The external air domain boundaries are defined as sound absorbing in order to measure free field responses.

3.4.3 Implementation in COMSOL

The numerical simulation is implemented in the finite element software COMSOL Multiphysics. The geometry studied in the model should represent the actual prototype that will be used in the experimental work. The collector mesh is chosen to have a rectangular cross-section of $50 \times 50 \text{ mm}^2$. Thus, the actuator has similar dimensions to a small electrodynamic driver. Moreover, with this size, the actuator is easier to study in the impedance tube (in the following chapters). Its size is relatively small compared to a wavelength at low frequencies so it can be considered as a point source in the far field. The distance between the collector mesh and the emitter electrode equals 6 mm. The emitter electrode is represented by a set of wires with a diameter of 0.1 mm. The electrode gap was chosen in order to operate at voltages below 10 kV because of the available high voltage amplifier for further measurements. The emitter wires are parallel to the collector plane and have the same distance between each other. The other parameters used in the simulation are listed in Table 3.1.

Equations (3.20)-(3.22) are processed in two-dimensional geometry because the quantities are assumed to not change in direction along the wires. This compromise was undertaken to keep the calculations time within reasonable limits and allow the computational mesh to be fine enough for the resolution of strong potential gradients close to HV electrodes. As a result, emitter wires are modelled as an array of circles with a diameter of 0.1 mm, and the collector is built as an array of 13 rectangles with 1 mm thickness, 3 mm width and spacing of 1 mm between the edges. The modelled collector represents the geometry of the perforated

Table 3.1: Physical and geometrical parameters of the CD.

Parameter	Symbol	Value	Unit
Positive ions mobility	μ_i	$1.1 \cdot 10^{-4}$	m^2/Vs
Voltage offset	U_{DC}	8.2	kV
Critical electric field	E_c	$1.3 \cdot 10^7$	V/m
Air mass density	ρ	1.23	kg/m^3
Emitter radius	R	$5 \cdot 10^{-5}$	m
Interelectrode gap	d	$6 \cdot 10^{-3}$	m
Wire length	l	$5 \cdot 10^{-2}$	m
Width of collector	w	$5 \cdot 10^{-2}$	m

plate further used to build the actuator. The electrode arrangement is placed in the centre of a circular air domain with a radius of 0.1 m.

The acoustic problem is modelled in a three-dimensional domain. The CD actuator is placed at the centre of a 0.1 m radius spherical domain. Another air domain with a thickness of 0.05 m encloses the sphere and represents a perfectly matched layer. It is used to model a free field radiation from the CD actuator with a compact size of the computational domains. The emitter electrodes are implemented as a set of cylinders, the collector as 13 parallelepipeds. Both arrays correspond to the height of 50 mm. The cross-sectional dimensions are the same as in 2D electrostatics modelling.

The simulation first computes the electrical potential and transport of charge problem in the time domain in 2D. Then, the 3D acoustic time domain simulation is performed based on the solutions of the first computation. The calculated distributions of current density, electric field, and space charge density are extruded along the electrodes over 50 mm (direction of extrusion corresponds to the z-axis in Figures B.2, 3.5. The mesh size was defined after preliminary sensitivity analysis. It consists of roughly 100 000 triangular elements for 2D electric simulation with minimal size of $5 \mu\text{m}$ (applied around the electrode edges), maximal size 10 mm and maximal growth rate 1.3. The mesh for acoustic computation contains 350 000 tetrahedral elements and has a larger characteristic dimension than in the electrostatic problem (minimal element size $5 \mu\text{m}$, maximal element size 3 mm, maximal grow rate of 1.6 for 1 kHz signal study).

3.4.4 Maximising the output power

The geometry of the corona discharge actuator (interelectrode distance, emitter radius) is almost completely defined by the available voltage range up to 10 kV and the mechanical strength of the wires (the smaller the radius - the higher the electrical field at a given voltage, but too thin wires are fragile). One adjustable parameter left is the number of HV wires to be placed over a 50 mm distance. This small study aims to choose the number of wires distributed

over the $50 \times 50 \text{ mm}^2$, which corresponds to the maximal output acoustic power. Therefore, we can run a parametric study in the numerical model in order to evaluate the performance.

Let us first analyse the expressions for a heat and force sources obtained from the analytical model. The Equations (3.14) and (3.19) can be rewritten in a slightly different form if we use a Townsend's relation also for a constant electrical current: $I_{DC} = CU_{DC}(U_{DC} - U_0)$. After few transformations:

$$\begin{aligned} H_\omega &= (2I_{DC} + CU_{DC}^2)u_{AC}, \\ F_\omega &= \frac{d}{\mu_i}(I_{DC} + CU_{DC}^2)\frac{u_{AC}}{U_{DC}}. \end{aligned} \quad (3.25)$$

We can see from Equations (3.25) that for a fixed bias voltage U_{DC} and alternating component u_{AC} , the magnitudes of the sources are greater for higher constant current I_{DC} , and parameter C . When several wires are combined as the emitter electrode, the voltage-current curve also has a steeper growth with a greater C value [104]. All this increases the magnitude of the sources. If condition $U_{DC} \gg U_0$ is satisfied, the total current from Townsend's formula is $I_{DC} \approx CU_{DC}^2$. The sources take a form:

$$H_\omega = 3I_{DC}u_{AC}, \quad F_\omega = 2I_{DC}\frac{d}{\mu_i}\frac{u_{AC}}{U_{DC}}. \quad (3.26)$$

Therefore, H_ω and F_ω can be proportional to the total electrical current and increase if the current grows. However, if too many wires are strung closely, the DC current can drop due to increased onset voltage U_0 . Thus, the numerical simulation can be carried out in order to determine the configuration, which results in the maximal DC current and, consequently, the maximal value of acoustic sources.

The numerical simulation was conducted with a constant voltage $U_{DC} = 8.2 \text{ kV}$ applied to the emitter wires. The n wires are aligned symmetrically with respect to the collector electrode. The distance between each wire is $\delta x = w/n$, and the distance between the external wires and collector edges is $0.5\delta x$. Figure 3.2 illustrates an example of $n = 5$ wires (the number of collector rectangles is 13 in the simulation). To evaluate the electrical current, only 2D simulation calculating electric potential and charge transport problems was performed.

Figure 3.2 presents the cumulative electrical current in the CD actuator as a function of the number of the emitter wires n . It can be seen that the current increases by more than two times when the number of wires changes from 1 to 3. The highest current is observed for the number of wires from 5 to 7. Arranging more wires over the 50 mm distance leads to a considerable decrease in the current magnitude. Therefore, we identified the possible

geometrical configurations that maximise the acoustic power. For the reasons of convenience, $n = 5$ was selected for further simulations and the experimental prototype.

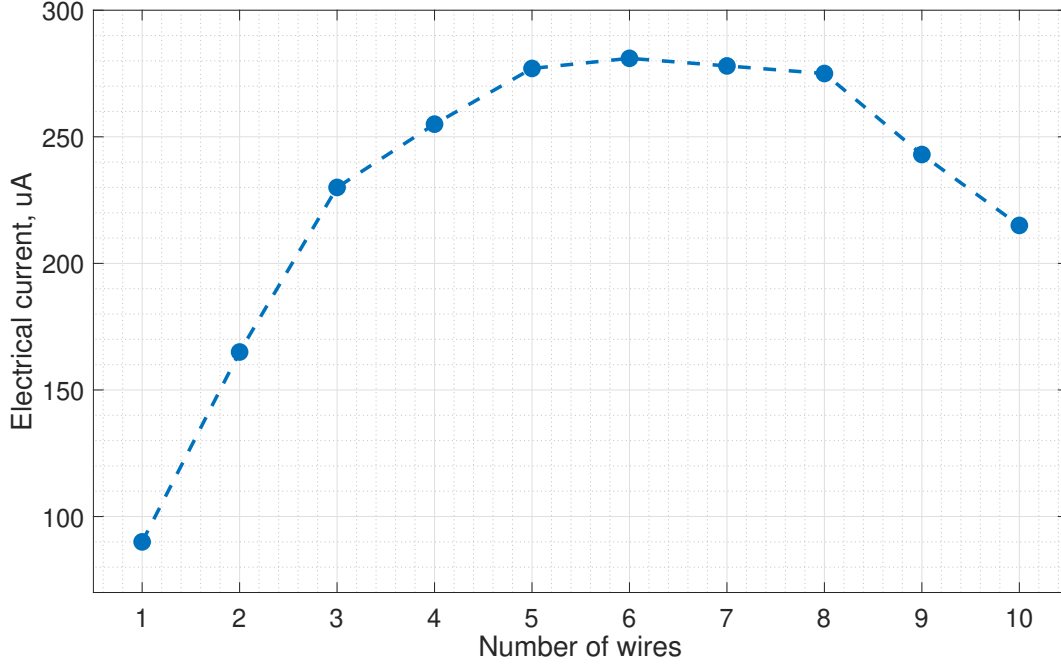


Figure 3.2: CD actuator electrical current dependence on the number of emitter wires. Constant voltage U_{DC} is applied.

3.4.5 Simulation capabilities

The numerical model can compute the sound pressure at an arbitrary location relative to the actuator. Figure 3.3 shows the three-dimensional directivity pattern by calculating the sound pressure level over a sphere of 1 m radius centred at the CD actuator. The transducer is biased with CD voltage and supplied with an 8 kHz sinusoidal signal. Three-dimensional radiation is rather complicated to measure. It is useful for the corona discharge actuator because it can be designed with a great geometrical freedom having non-symmetrical electrode arrangement. As can be seen, the high frequency radiation is rather complicated at high frequencies when the actuator geometry is not symmetric relative to the main axis (y-axis in Figure 3.3). An example of low frequency radiation by the CD actuator is provided in Appendix B in Figure B.2.

The distribution of acoustic pressure in the vicinity of the electrodes is illustrated in Figure 3.4 in the plane that cuts the actuator in the center. The data is taken from the time-domain simulation. Negative and positive pressure regions indicate the presence of the external force directed in the negative y-axis direction. The high magnitude pressure regions can be observed around the HV electrodes and under them on the collector grid inner side closest to the HV

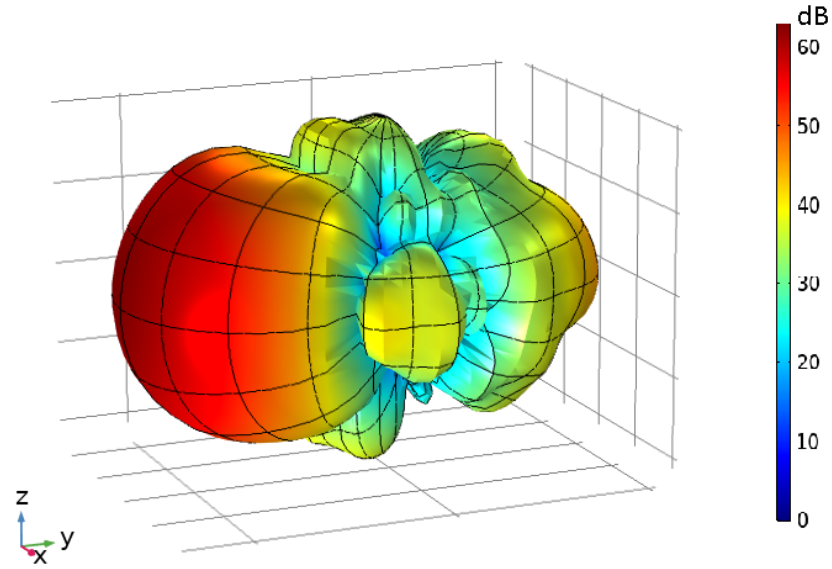


Figure 3.3: Three dimensional directivity pattern of the corona discharge actuator at 8000 Hz. $U_{DC} = 8.2$ kV, $u_{AC} = 300$ Vrms. The sound pressure level on the colour bar corresponds to the magnitude at the distance of 1 m.

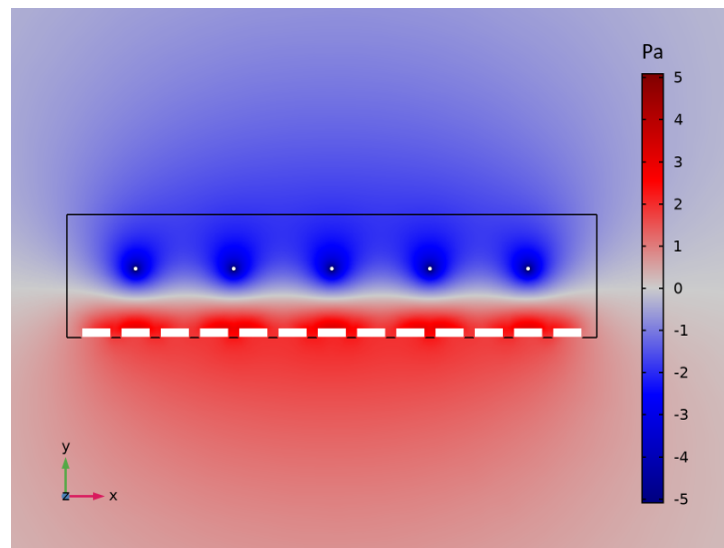


Figure 3.4: Acoustic pressure in the vicinity of the electrodes at an arbitrary time moment. Actuator is biased with $U_{DC} = 8.2$ kV with applied sinusoidal signal at 1 kHz with amplitude $u_{AC} = 425$ V. The distribution is shown in the horizontal plane.

electrodes. Nevertheless, on the outer side the pressure is more homogeneous along the collector grid. Therefore, the actuator creates a rather uniform pressure front as a membrane transducer. The other acoustic characteristics, such as frequency response, and directivity

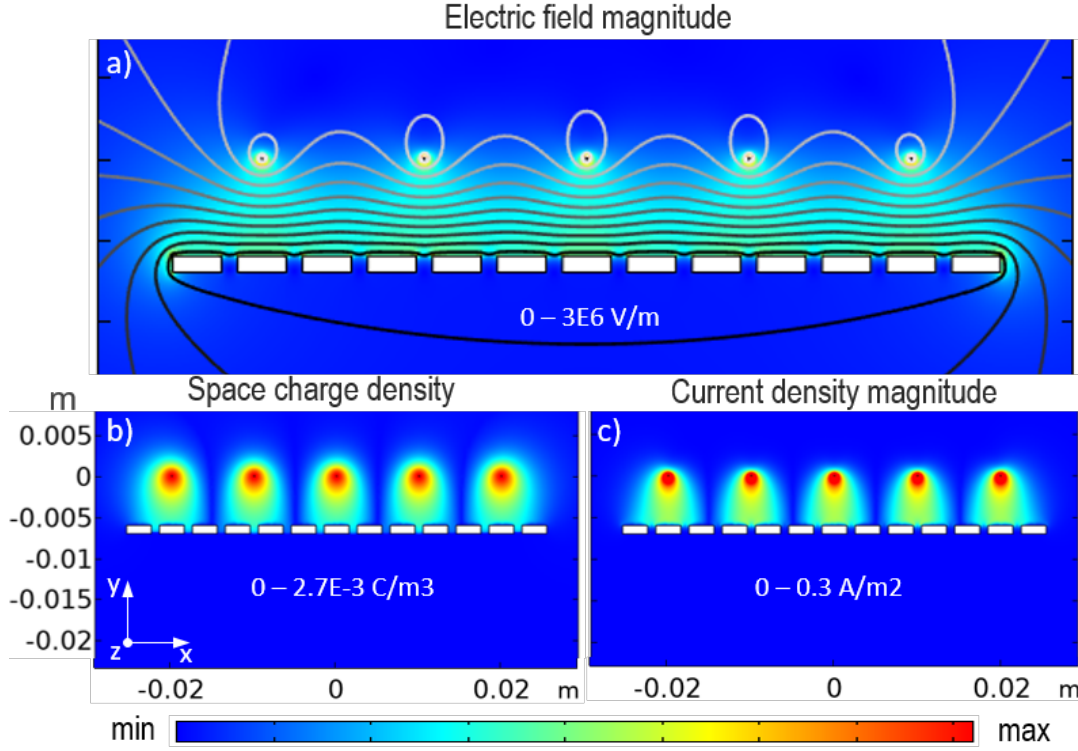


Figure 3.5: a) Electric field magnitude with equipotential lines; b) Space charge density; c) Current density magnitude. The actuator is supplied with constant voltage $U_{DC} = 8.2$ kV. The magnitude ranges indicated on the figures correspond to “min-max” colourbar, but do not represent the highest values calculated in the simulation.

patterns at different frequencies, which are calculated with the numerical model, will be presented in Chapter 4.

Along with the acoustic radiation modelling, the simulation can provide an insight on the electrical parameters in the corona discharge. Figure 3.5 illustrates the electrical field, positive ions density, and electrical current density distributions close to the electrodes. The electrical field presents a rather uniform distribution in bulk between the electrodes. Its magnitude becomes negligible behind the collector grid. This aspect can be important for the experimental measurements. It indicates that the sensors, which might be sensitive to a high electrical field, can be placed in the vicinity of the actuator without danger. The potential isolines also accompany the electrical field map. The lines are horizontal in most of the volume between the electrodes, which confirms that the electrical field is directed normally from the emitter plane to the collector plane and can be approximated by the field of the flat plate capacitor. This indirectly validates one of the assumptions made in the analytical model in Section 3.3. An example of the electrical field distribution in the CD actuator with two wires forming the emitter electrode is provided in the Appendix B (Figure B.3). In this case, such an assumption does not hold.

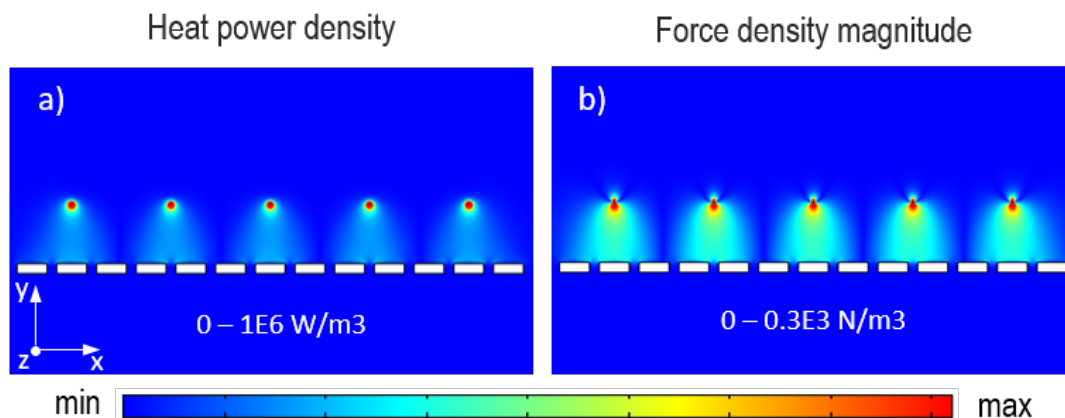


Figure 3.6: a) Heat power density b) Force density magnitude. The actuator is supplied with constant voltage $U_{DC} = 8.2$ kV. The magnitude ranges indicated on the figures correspond to “min-max” colourbar, but do not represent the highest values calculated in the simulation.

The space charge density in Figure 3.5 is concentrated around the wires. As we can see, the charged particles generated in the vicinity of each electrode form distinctive clouds which stretch towards the grounded grid. They do not merge because of the Coulomb force acting on the similarly charged particles. The current density looks similar to the ions distribution, however, around the HV electrodes, the maximal values are shifted towards the collector. Finally, the three quantities from Figure 3.5 are linked by a simple relation: $J = \mu_i \rho_i E$. Therefore, by knowing two distributions, the third one can be easily calculated. If fewer wires form the emitter, the distributions are different. The clusters of ions expand, and greater movement along the x-axis can be observed. As we are interested only in the vertical movement of the air particles (from the emitter electrode to the collector) for the active control applications, the larger number of electrodes is to be favoured.

Figure 3.6 shows the distribution of the heat power density and y component of force density magnitude. The plots represent the values in the case when the actuator is supplied with a constant voltage. However, the case with an AC component looks identical. It can be observed that the heat power is more concentrated around the emitter wires than the force source. These quantities were estimated over a rectangular area with a thickness of 0.5 mm (along the y-axis) and width of 50 mm (along the x-axis), where the emitter wires are positioned in the centre. The measurement was compared to the total heat power and force, integrated over the whole volume between the electrodes. As a result, a thin layer around the emitter contains more than 25 % of the total heat power produced in the discharge. It is not the case for the force calculation, where less than 8 % is constrained around the emitter compared with the whole volume. In contrast to the analytical model, where the distributions of heat and force are considered uniform, the numerical simulation takes the space-dependent sources into account to calculate the acoustic response.

3.5 Conclusions

The chapter studied the positive corona discharge in a wire-to-mesh geometry. Such configuration was chosen because stringing the array of wires allows distributing the discharge over a larger surface which can be potentially controlled. In order to grasp more understanding of the underlying corona discharge physics and its electroacoustic principles, the analytical model and numerical model in finite-element software were developed.

The analytical model considers the CD as a small volume of air, where the mechanical force and the supply of heat energy exist. The force is the mechanism of momentum transfer from the charged particles to the neutral air particles with 100% efficiency, where the density of ions is assumed to be negligible. The force has an electrical origin and is defined as the product of the charge and external electric field, which is created by the electrode system. The heat source is considered as the total Joule losses in the discharge. The model operates by the quantities averaged over the whole discharge. Thus, it only requires knowledge of the relationship between voltage and current. This has to be estimated experimentally by simply measuring the voltage-current characteristics, which is a relatively simple procedure. As a result, the magnitude of the sound sources and the radiated sound pressure can be estimated.

The numerical model takes into account the geometrical details of the actuator. It first solves the electrostatic problem with the transport of charge and consecutively the acoustic radiation. The model is still considerably simplified compared to the complete discharge physics. Nevertheless, it provides access to the distribution of the electrical parameters between the electrodes and indirectly validates some analytical model assumptions. An important result is the rather uniform electrical field distribution. It finally causes the generated acoustic pressure and velocity to be the same over the whole collector surface. Simulation results were used to finalise the geometry of the CD actuator prototype that maximises the electrical and, consequently, the acoustic power. One outstanding feature of the numerical model is its self-sufficiency. The simulation does not require any experimental data from a given actuator. Therefore, it can be potentially used to design and evaluate the CD-based transducers without tedious experimental measurements. Further studies can also exploit the model for transducer optimisation purposes with more parameters than presented here.

However, the models should be validated by direct comparison with the experimental measurements. This task is merged together with the acoustic characterisation of the experimental prototype in the next chapter.

4 Electroacoustic characterisation of the corona discharge actuator

This chapter presents the experimental assessment of characteristics of the corona discharge actuator prototype. It is essential for active sound control applications to have a transducer which does not introduce distortion to the signal. The prototype is designed with the dimensions defined previously and taking into account the parametric study performed with the numerical model. The following characteristics are measured: free field frequency response, pressure directivity patterns, and total harmonic distortion. This experimental data, also including the voltage-current curve, is compared with the numerical simulation results and the analytical model presented in the previous chapter.

The chapter contains some of the material published in the following paper:

Sergeev, S., Lissek, H., Howling, A., Furno, I., Plyushchev, G., and Leyland, P. (2020). Development of a plasma electroacoustic actuator for active noise control applications. *Journal of Physics D: Applied Physics*, 53(49), 495202.

4.1 CD actuator prototype

The corona discharge prototype is illustrated in Figure 4.1. The two electrodes system is designed in a wire-to-mesh geometry. The HV electrode is made of a single wire of 0.1 mm diameter. Nichrome alloy is chosen for this electrode because of its mechanical strength even with such a diameter. Moreover, this material is known to be resistive to oxidation, which is caused by local ionisation and heating. The wire is arranged in a back and forth pattern of 5 parallel wire lengths spaced by 10 mm through the rigid plastic frame. It results in the 5 identical segments which participate in the ionisation process because the rest of the wire is hidden inside the frame and does not produce ions. Such a corona electrode is strung parallel to the second grounded electrode. The latter is fabricated from a perforated stainless steel plate with a thickness of 1 mm. This electrode has a large open area ratio so that its flow

resistance is low (it was measured to be 2% of the characteristic air impedance). It should be mentioned that the geometry of the plate is taken into consideration in the numerical simulations since the thickness of the modelled rectangles and percentage of open area are similar (see Section 3.4.3). The frame separating the electrodes is 3D-printed from Polylactic acid (PLA) plastic. The actuator hollow area is $50 \times 50 \text{ mm}^2$, and the distance between the HV and collector electrodes is 6 mm. When the actuator is biased with a positive high voltage, a stable corona discharge is produced with a homogeneous glow along the wire lengths. The geometry in Figure 4.1 provides a corona discharge in the 6.5-10 kV voltage range. At higher voltages, sparking is observed.

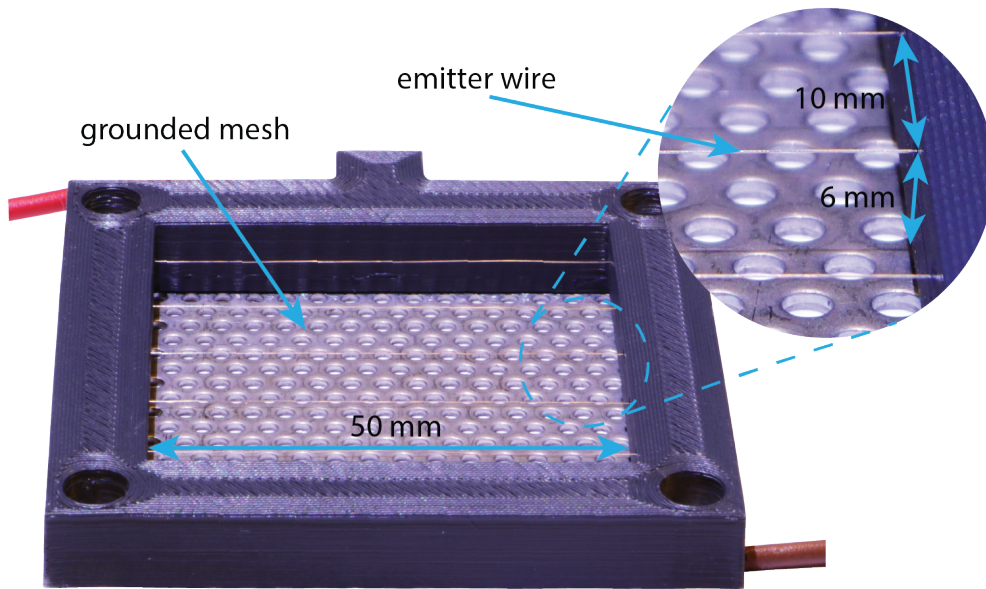


Figure 4.1: Photo of the corona discharge actuator designed in a wire-to-mesh geometry. The top-right magnified picture highlights the high voltage electrode formed by the nichrome wire segments.

4.2 Experimental setup

The acoustic measurements presented in this chapter are carried out in the anechoic chamber of EPFL (cut-off frequency 80 Hz). The schematic of the experimental setup is shown in Figure 4.2. The pressure signal is recorded with PCB 378B02 1/2" free-field condenser microphone. The CD actuator is fixed on a turntable in order to be able to measure its directivity in the horizontal plane. The frequency response measurement corresponds to the angle $\theta = 0^\circ$. In this case, the collector mesh faces the microphone. The distance between the microphone and the actuator is 1 m. TREK 615-10 high voltage amplifier ($\pm 10 \text{ kV}$, 10 mA) powers the actuator.

It amplifies the input signal by the factor 1000 to obtain u_{AC} and adds a constant bias voltage U_{DC} . The generation of the signal to the high voltage amplifier and the acquisition of the microphone signal is carried out with Brüel&Kjaer Type 3160 Pulse Multichannel Analyser.

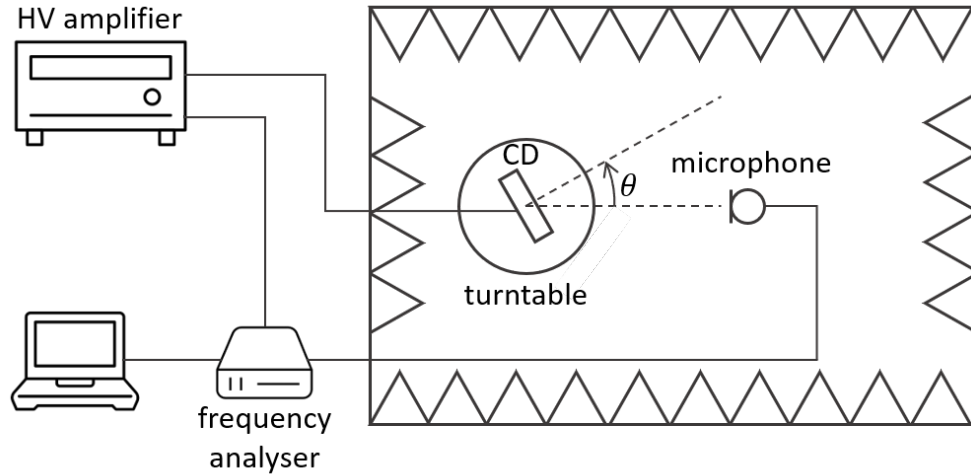


Figure 4.2: Schematic of the CD actuator measurements setup. Not to scale.

4.3 Voltage-current characteristics

To be able to use the analytical model for the frequency response estimation, the voltage-current curve should be measured experimentally (Figure 4.3). The DC current is sensed with a micro amperemeter connected in series with the actuator to its grounded terminal. The measurement is conducted in the voltage range up to 9 kV. As can be seen, the DC current in the actuator does not exceed 0.5 mA. Thus, the actuator consumes approximately 2 W of DC power in the middle of the operation range at 8 kV. The experimental curve (blue curve) is superimposed with the characteristics calculated in the numerical simulation (green curve in Figure 4.3). The total current is estimated in the model as the integral of the current density over the whole emitter surface. We can observe that both curves exhibit prominent nonlinear dynamics. However, the electrical current in numerical simulation (green curve) presents a less steep rise than in the measurements. Besides, the discharge initiates at slightly lower voltages in the model. The difference with the experimental curve could occur due to several reasons. First, the exact geometry of the actuator cannot be completely reflected in a two-dimensional simulation, although the porosity and thickness of the collector grid are considered. The electrodes can also have some imperfections, such as a non-circular cross-section of the emitter wire or sharp edges on the perforated plate, which can lead to the increase of the actuator current. Second, the effective mobility of ions is assumed to be constant in the model. Its value is taken from the literature at average air humidity, which cannot be the case in the experiment. Nonetheless, the numerical simulation captures the essential features of the discharge, such as its initiation and slightly nonlinear dynamics. If

the bias voltage U_{DC} is set close to 8 kV, the mismatch between the simulated and measured curve does not exceed 10% for u_{AC} up to 800 V.

The experimental data is also fitted with Townsend's formula (red curve). The weights of the least-squares approximation are focused around the voltage of 8 kV as it corresponds to the middle of the operating range. The retrieved parameters $C = 1.69\text{e} - 11 \text{ A/V}^2$, $U_0 = 6190 \text{ V}$ are used further to set up analytical model from Section 3.3.

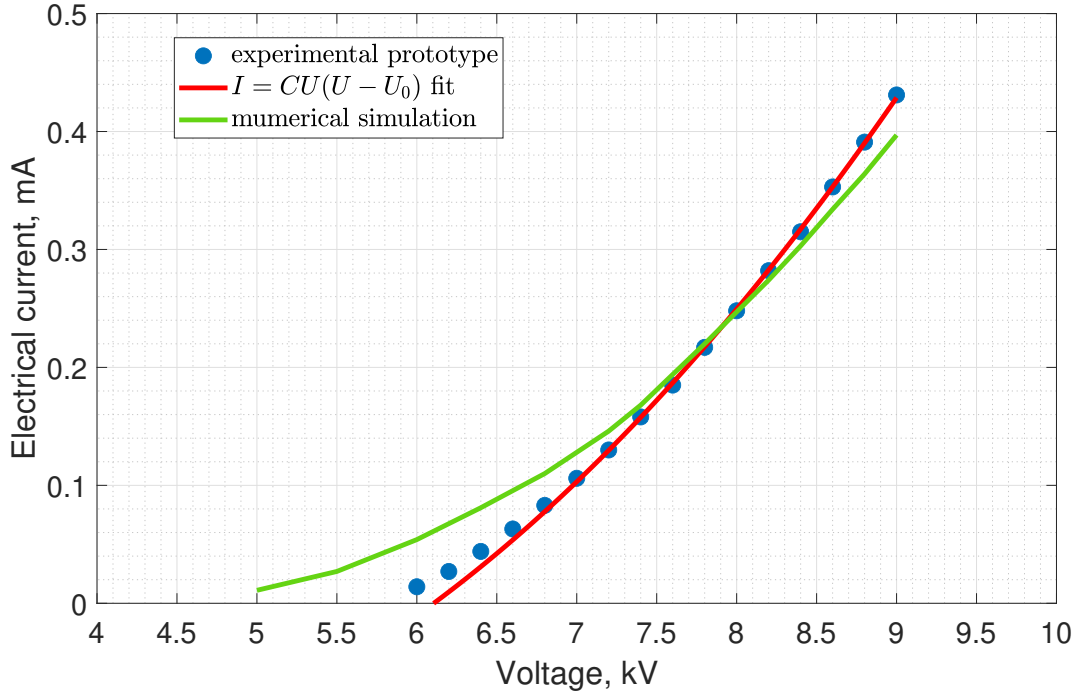


Figure 4.3: Voltage-current characteristics of the corona discharge actuator from Figure 4.1. Blue dots - measurements; red curve - least-squares fit of the experimental data with formula $I = CU(U - U_0)$, $C = 1.69\text{e} - 11 \text{ A/V}^2$, $U_0 = 6190 \text{ V}$; green curve - numerical simulation.

4.4 On-axis frequency response

To measure the frequency response, the CD actuator is biased with $U_{DC} = 8.2 \text{ kV}$. As the alternating component, a swept sinusoidal signal is applied with the amplitude of 300 Vrms. The sound pressure levels (SPL) recorded in the anechoic chamber and obtained with analytical and numerical models are presented in Figure 4.4. The red curve from the analytical model is obtained as the magnitude of the total sound pressure, which is the sum of heat and force-induced components from Equations (3.9), at a distance of 1 m and $\theta = 0^\circ$. The sources are calculated from Equations (3.14) and (3.19). All the needed parameters are taken from Table 3.1. It should be noted that at frequencies below 300 Hz and above 3 kHz, the

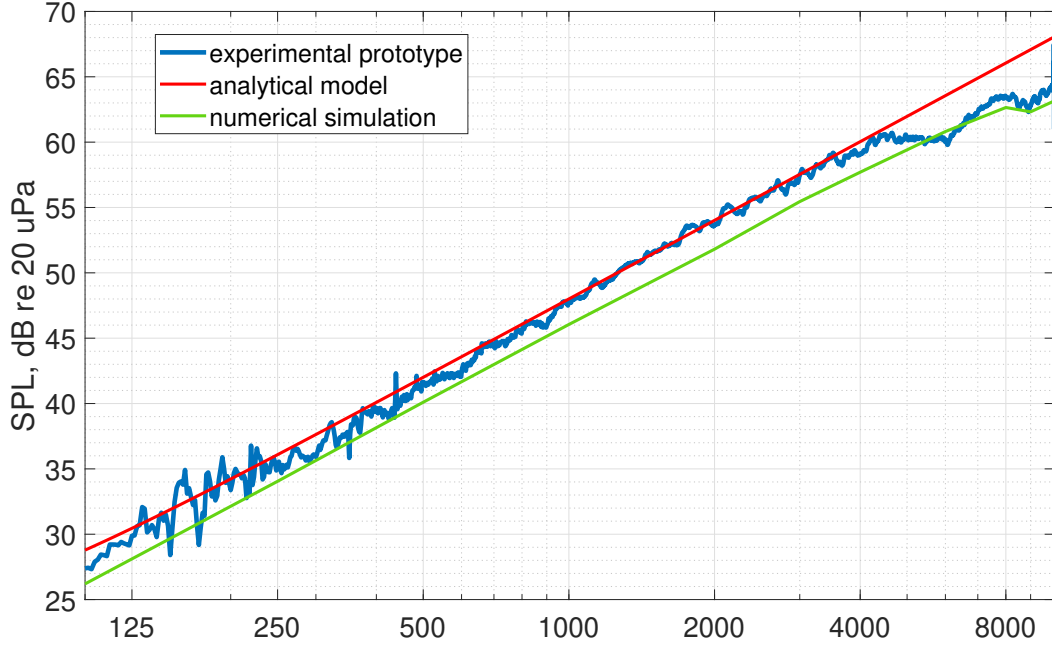


Figure 4.4: On-axis sound pressure levels of the corona discharge actuator in the frequency range 100 - 10000 Hz, measured at 1 m with $U_{DC} = 8.2$ kV, $u_{AC} = 300$ Vrms in blue. The data is compared with the analytical model (red curve) and numerical model (green curve).

measurements do not fully satisfy the far field and small source conditions correspondingly, which are assumed in the analytical model.

As expected, the CD actuator does not present any resonant response due to the absence of moving mass. The sound pressure level increases with the rate of +6 dB per octave. This dynamics is well in line with the tendency obtained with both analytical and numerical models. On the other hand, we see that the sound pressure levels simulated numerically lay (green curve) on average 1.5 dB lower than the experimental curve. Referring to the comparison of voltage-current characteristics (Figure 4.3), a less steep slope of the numerical curve leads to the smaller swing of electrical current in the actuator at the same magnitude of u_{AC} , which can lead to slightly lower generated sound pressure. In contrast, the levels obtained with the analytical model (red curve) match well with the experimental results up to 4 kHz. If force and heat sources are considered dipolar and monopolar correspondingly, constant slope also confirms that the distance between these acoustic sources can be neglected in this frequency range, otherwise the phase shift would change the slope of the curve. At higher frequencies, the measured response slightly deviates from the 6 dB/octave slope. This can be because the prototype dimensions are not negligible compared to the wavelength anymore, and the spatial distribution of the sound sources plays a more important role. Moreover, the analytical model does not consider the electrical resistance and capacitance of the discharge, which

at high frequencies can contribute to low-passing the alternating current component and reduce the radiated sound pressure [94]. Therefore, it keeps the same slope and does not follow the experimental curve. The numerical response also gradually changes the slope at high frequencies. Since the numerical model does not use the abovementioned assumptions, it can describe the response trend at high frequencies more precisely. Nevertheless, in the frequency range of interest for sound control, which does not exceed few kilohertz, both the analytical model and numerical simulation provide a reasonable estimation of the frequency response of the CD actuator of comparable size.

From the frequency response and the voltage-current characteristics, we can make an estimation of the CD efficiency in terms of the electroacoustic conversion. At 1000 Hz the actuator produces 48 dB SPL at 1 m with an input signal amplitude $u_{AC} = 300$ Vrms. It corresponds to approximately 10^{-7} W in terms of acoustic power. The AC electrical power can be upper-bounded by the product of AC current and voltage magnitudes, which results in ≈ 20 mW. As we can see, the AC power is much smaller than the DC one that maintains the ionisation (≈ 2 W). Therefore, the efficiency as the ratio of acoustic power to the AC electrical power equals $0.5 \cdot 10^{-5}$. According to the frequency response plot, it is higher towards the high frequencies and decreases in the opposite direction.

4.5 Directivity patterns

The measured directivity patterns and the ones derived from both models are presented in Figure 4.5. The measurements are conducted at discrete frequencies (250, 500, 1000, 2000, 4000, 8000 Hz). In the frequency range 250-2000 Hz, the pressure is estimated with 10° step, at higher frequencies, it is refined to 5° . In the low frequency range, the patterns correspond to a supercardioid shape, which is the combination of a dipole and a monopole operating in phase. Both analytical and numerical models replicate precisely the shape of the radiation. From the difference in the magnitudes between front and back radiation at low frequencies that corresponds to 4 dB, we can conclude that the dipolar source (force source) is 4.4 times stronger than the monopole (heat source). This pattern shape was also observed in different geometrical configurations such as point-to-plane [105, 72], but the relative strength of the sources is considerably different (force-related pressure is approximately 2 times higher). Thus, the geometry of the actuator can be potentially adjusted to obtain the desired radiation pattern. It also highlights that the heat-produced pressure is non-negligible compared to the part generated by the electrical force. As the frequency increases, the CD actuator becomes more directive. It can be seen that although the front radiation (corresponds to the frequency response) stays in good correspondence with analytical data till high frequencies, the rest of the pattern does not match the model. Since the analytical model describes the perfect monopole and dipole, the directivity shape does not change. However, at 8 kHz, the secondary lobes can be observed in the experiment. The numerical model is able to capture the general shape of the radiation pattern at high frequency since it is influenced by the actuator geometry and sources positions. In addition, the difference between the front and back radiation also

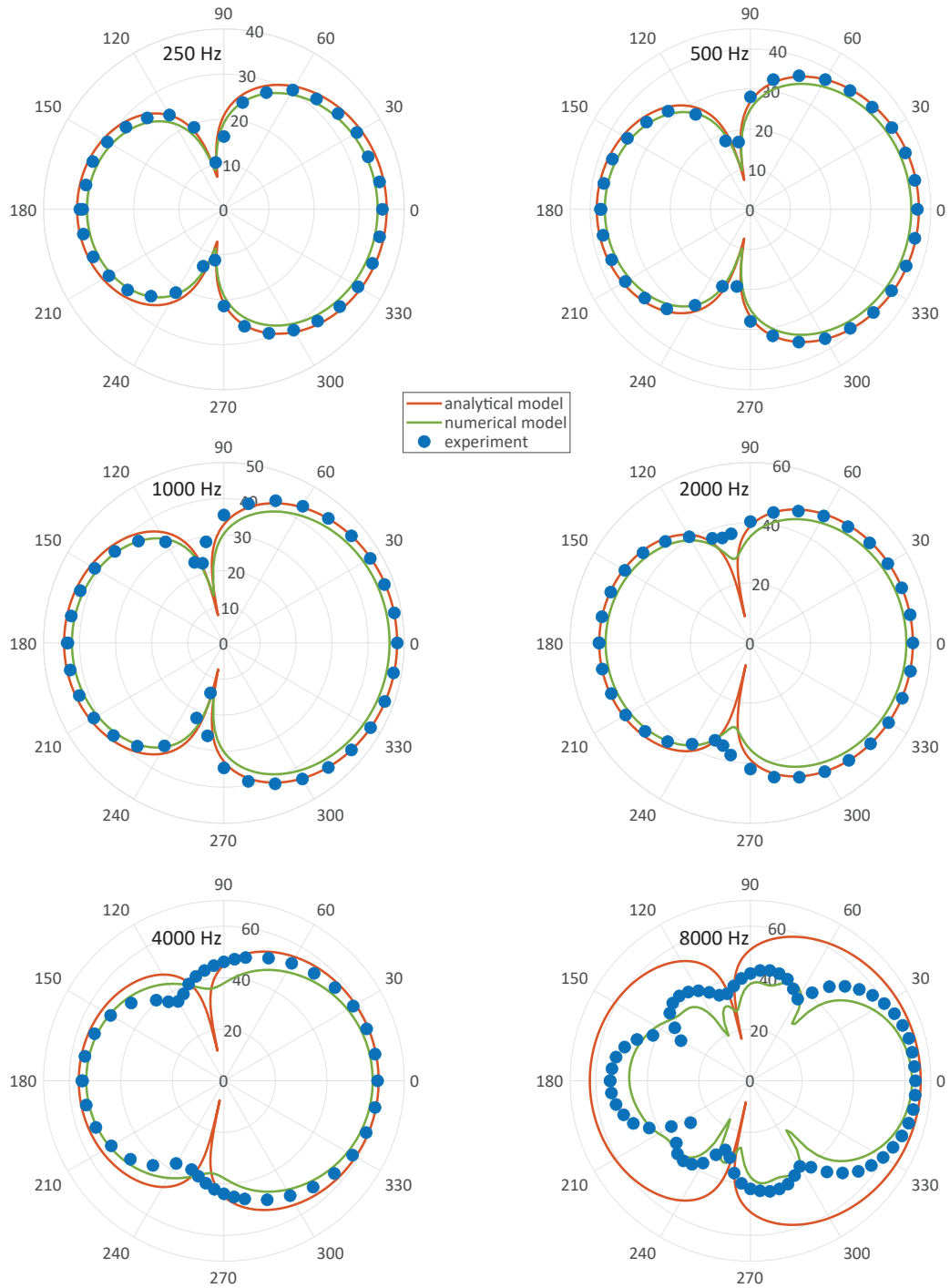


Figure 4.5: Directivity patterns of the corona discharge actuator at frequencies 250, 500, 1000, 2000, 4000, 8000 Hz. Magnitude is in dB normalised to 20 uPa. $\theta = 0^\circ$ corresponds to the frequency response case. $U_{DC} = 8.2$ kV, $u_{AC} = 300$ Vrms.

increases towards high frequencies. It suggests that the relative strength between the force and heat sources evolves with frequency, and the heat radiated pressure approaches in magnitude to the pressure created by the force.

4.6 Total harmonic distortion

The total harmonic distortion (THD) of the transducer expresses the relative contribution of the higher order harmonics to the generated acoustic pressure at a given frequency when a pure sinusoidal electrical signal is applied. It indicates the degree of non-linearity in the electroacoustic conversion. The THD in percentage can be written as:

$$THD = 100 \sqrt{\frac{\sum_{n=2}^{\infty} A_n^2}{A_1^2 + \sum_{n=2}^{\infty} A_n^2}}, \quad (4.1)$$

where A_1 is the amplitude of the fundamental frequency, and A_n is the amplitude of the n -th harmonic. The evaluation was performed by measuring the sound spectra of the sinusoidal signals of various frequencies and amplitudes. The acoustic signal was recorded at 1 m distance from the actuator at $\theta = 0^\circ$. The amplitudes at the fundamental frequency and its harmonics are recorded, then THD is calculated according to Equation (4.1).

Figure 4.6 presents the THD of a CD actuator at selected frequencies for excitation voltages u_{AC} from 50 to 400 Vrms. The bias voltage is set to 8.2 kV, so the alternating component does not exceed 7 %. The resulting THD remains lower than 10 % for the highest excitation voltage at any of the considered frequencies. Most of the curves, which correspond to a single frequency, indicate the linear increase of the THD when the excitation voltage increases. There is no visible evidence if higher or lower frequencies are more distorted. At some frequencies (250, 4000, 8000 Hz), the distortion decreases at low u_{AC} , but then also tends to grow linearly. We cannot suggest any reasonable explanation for the measured drops in THD at these frequencies. Although the overall distortion may be unsatisfactory for sound reproduction applications, the levels are still sufficiently low for active control to bring enough benefit [106]. For the sake of comparison, the THD of the CD actuator, when it is biased with the negative high voltage, is provided in Figure B.4 in Appendix B.

The total harmonic distortion can be also predicted by the means of analytical model. The sound sources from Equations (3.11), (3.16) have the following amplitudes:

$$\begin{aligned} H_\omega &= C(3U_{DC}^2 - 2U_{DC}U_0)u_{AC}, & H_{2\omega} &= C(3U_{DC} - U_0)u_{AC}^2, & H_{3\omega} &= Cu_{AC}^3. \\ F_\omega &= \frac{Cd}{\mu_i}(2U_{DC} - U_0)u_{AC}, & F_{2\omega} &= \frac{Cd}{\mu_i}u_{AC}^2. \end{aligned} \quad (4.2)$$

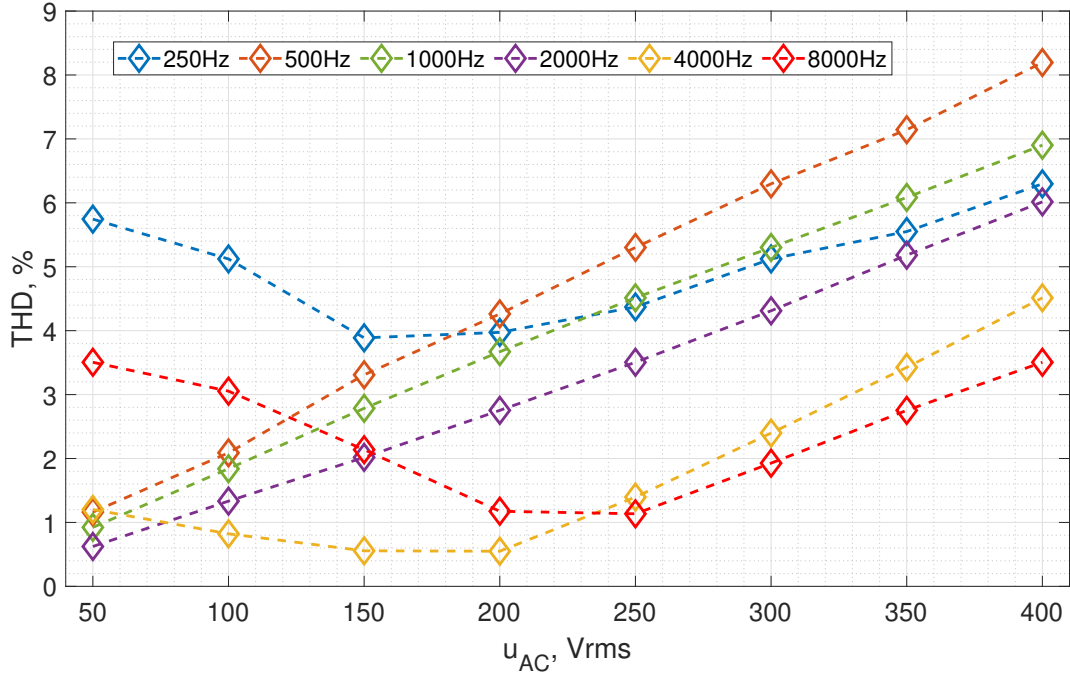


Figure 4.6: Total harmonic distortion in percents of the CD actuator at frequencies 250, 500, 1000, 2000, 4000, 8000 Hz. The actuator is biased with $U_{DC} = 8.2$ kV.

We can see that approximating voltage-current characteristics of the discharge with Townsend's formula results in the appearance of the second and third harmonics in sound sources. Higher order polynomial approximation of the curve would lead to a greater number of harmonics. From formulas (4.2), it can be seen that the relative strength of the nonlinear terms depends on the amplitude of u_{AC} , compared to the fixed bias voltage U_{DC} and onset voltage U_0 . Finally, the rest is to plug components from Equation (4.2) in the corresponding terms of the pressure solution in Equation (3.9), and estimate the harmonic distortion of the total pressure according to Equation (4.1). The result is shown in Figure 4.7.

The lines corresponding to different frequencies superimpose. Only very low frequencies can present different distortion (lower values) due to the presence of the factor $jk(j/kr + 1)$ in the force-induced pressure from Equation (3.9). Otherwise, according to the analytical model, THD almost does not depend on the frequency and behaves as a linear function of the u_{AC} amplitude when u_{AC} is much smaller than U_{DC} . Although the model slightly overestimates THD, compared to the experiment, a generally good agreement can be seen. If the high frequency experimental measurements of THD (4000 and 8000 Hz in Figure 4.6) are considered to be outliers, then the measurements at the other frequencies are rather close to each other, resembling the model result. Finally, the linear trend indicates that the distortion is governed mainly by the second harmonic.

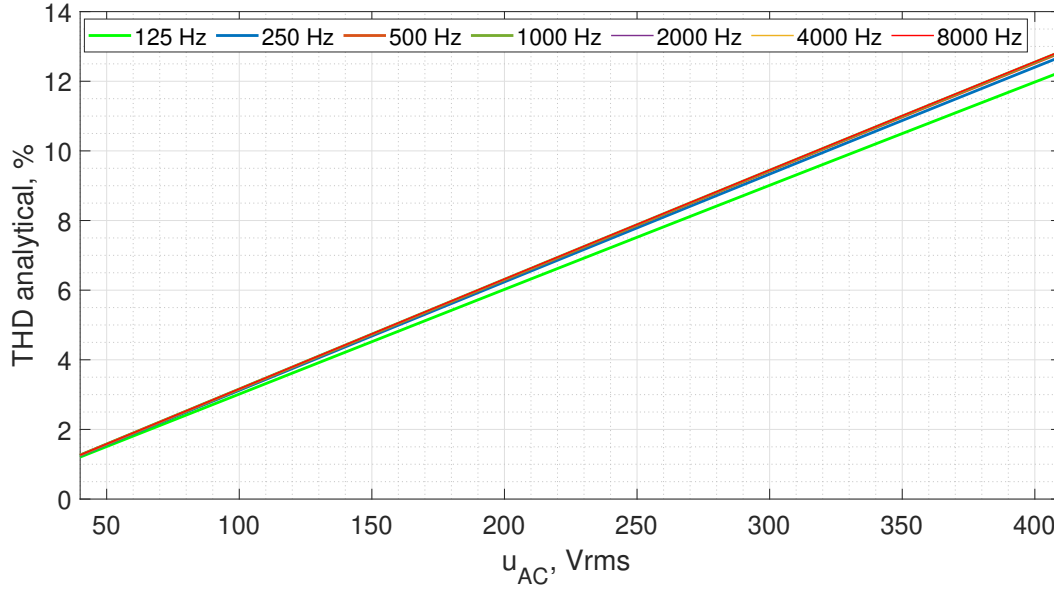


Figure 4.7: Total harmonic distortion in percents of the CD actuator at frequencies 250, 500, 1000, 2000, 4000, 8000 Hz, calculated with the analytical model from Equations (4.2). The actuator is biased with $U_{DC} = 8.2$ kV, the needed parameters are taken from Table 3.1, and Figure 4.3.

4.7 Conclusions

In this chapter, we investigated the acoustic characteristics of the corona discharge actuator. For this purpose, the experimental prototype was manufactured in a wire-to-mesh geometry. It has an active area of $50 \times 50 \text{ mm}^2$ and an electrode gap of 6 mm. The arrangement of the emitter wires reflects the result of electrical current optimisation in the numerical simulation. The experimental measurements are cross-compared to the results provided by analytical and numerical results to evaluate the validity of the models.

In free field, the CD actuator is able to generate the sound pressure, which frequency response presents a 6 dB/octave rise in the low frequency range in free field. This tendency is the result of the heat and force sources radiation. From this perfect slope, we can conclude that the magnitude of the sources does not vary with frequency, thus, they can be considered ideal. However, at frequencies where the size of the actuator is of the same order as the wavelength, the curve deviates from this ideal response. The directivity measurements allow determining the relative strengths of the heat and force sound sources. At low frequencies, the patterns have a supercardioid shape, while at high frequencies, secondary lobes appear.

The harmonic distortion of the CD actuator appears to be proportional to the excitation amplitude if it is limited compared to U_{DC} . The linear dependence reasonably comes from close to the almost quadratic dependence of electrical current on the applied voltage, which results

in a prominent second harmonic in both sound sources. Although the discharge is rather convenient to control in voltage, the direct control of electrical current can potentially lower the harmonic distortion [107] because both heat and force sound sources are proportional to the current. Nevertheless, the distortion level stays in sufficiently low bounds for active sound control, which makes CD the most suitable among the other plasma-based actuators.

The numerical and analytical models demonstrate, in general, a good agreement with the experimental data. The analytical model describes well the low frequency response of the actuator. It means that the sound sources are sufficiently precisely estimated via voltage-current characteristics. Thus, this framework can be potentially used to implement the model-based control system. However, the analytical model cannot be used to predict the dynamics of an actuator design which has not been manufactured yet. When the design needs to be evaluated with fewer resources, the numerical model appears to be useful. Although some discrepancies with the experimental data in the calculated sound pressure levels are observed, the model better reflects the high frequency part of the acoustic response. From the numerical simulation, it was seen in the Chapter 3 that the current density is concentrated around the emitter wires. Thus, the high frequency response of the analytical model could be improved if the actuator is considered as the combination of several identical smaller sources separated in space.

To conclude, it should be mentioned that the construction of the actuator is relatively simple and mechanically robust. Since the sound radiation is governed by the ionised particles, which dynamics does not change with the actuator surface, the CD actuator can offer some flexibility in design and applications without change of the response at low frequencies. All this makes the CD-based actuator in the proposed geometry an attractive alternative to conventional transducers for active noise control.

5 Feedback impedance control of corona discharge actuator

5.1 Introduction

As discussed in the introduction, active sound control with the aim of noise reduction can be achieved by minimising the acoustic pressure at a given location or absorbing the incident sound wave [108]. As in any other field of active control, the transducers are driven in a feedback or feedforward manner [8]. The feedforward method manipulates the controlled sources in a predefined way, often involving a model of the transducer which is experimentally estimated or theoretically derived. In contrast to this, the feedback architecture typically provides all the necessary information for control from external sensors. As a consequence, this approach does not require any model of the transducer and can inherently be more adaptive to the changing environmental conditions. The first electroacoustic sound reducing device was proposed in [7]. A proportional feedback signal from a microphone drives the controlled loudspeaker in order to minimise the sound pressure locally at the sensor position. At low frequencies, it forms a so-called “silent zone” which can reduce sound levels in enclosed volumes or block the transmission through the partitions [109, 110, 111]. Alternatively, the impedance control aims to suppress any reflections of sound waves that impinge on the active interface. Using a pair of sensors (two microphones, accelerometer and microphone, laser velocimeter and microphone, etc.), it is possible to estimate the acoustic pressure and particle velocity close to the transducer and adjust their ratio to the target impedance value in a feedback loop [112, 113, 114, 115]. A passive porous material with a controlled source releasing pressure at its back can also be used for impedance control. In the case of a matched impedance, it leads to sound absorption [116, 114]. Such a combination improves a low frequency absorption of a passive quarter-wavelength resonator. However, the bandwidth of absorption of both direct impedance control and hybrid impedance control are limited by the resonant response of the actuator as was discussed in the introduction. To extend the bandwidth of operation, the impedance control techniques can be combined with the

adaptive LMS algorithm [113, 117, 90, 118].

The above-mentioned feedback impedance control approaches require low signal distortion from an electroacoustic transducer to absorb sound successfully. The CD actuator presented in the previous chapter, with its satisfactory low harmonic distortion and non-resonant response, can potentially extend the bandwidth of control. It should be mentioned that there are no works in the available literature so far (except the ones published by the author of this thesis) which investigate the active sound absorption with plasma-based actuators. One attempt was reported by Nasiri [119] to cancel out a single-tone acoustic noise generated by a loudspeaker in a duct using a surface dielectric barrier discharge actuator. Although the main tone amplitude was slightly reduced, strongly nonlinear response of the actuator diminished the positive outcomes of active noise control. Therefore, to our knowledge, this work is the first in the field since the plasma-based actuators were never used for active impedance control.

The goal of this chapter is to investigate the use of the proposed CD actuator in feedback impedance control so as to provide more broadband performance than other commonly used loudspeakers. First, the concept of hybrid sound absorption is described, followed by the implementation and experimental assessment under normal sound incidence. Then, the pressure-velocity feedback impedance control strategy with the CD actuator is studied. Finally, both concepts are applied to realise an active acoustic liner for noise reduction under grazing sound incidence.

Some parts of the work reported in this chapter is published in the following paper:

Sergeev, S., Humbert, T., Lissek, H., and Aurégan, Y. (2022). Corona discharge actuator as an active sound absorber under normal and oblique incidence. *Acta Acustica*, 6, 5.

5.2 Hybrid passive-active impedance control

This method aims to maximise the absorbing properties of passive porous material with the use of active control. The approach is attractive for an unknown actuator such as a corona discharge. It relies on the pressure measurement in front of the transducer and only requires a low output signal distortion in order to avoid generating noise at high harmonics since the control is purely linear.

5.2.1 Principle of the hybrid absorption

If a constant pressure difference is applied at two sides of a porous layer, it generates a steady airflow. Viscous forces dominate in the material, and the flow characteristics mainly depend on the flow resistivity. Assuming microscopically homogeneous porous layer of thickness d with flow resistivity r , under a net pressure difference $p_1 - p_2$ (Figure 5.1), the induced flow velocity can be written as:

$$u = (p_1 - p_2) / r d. \quad (5.1)$$

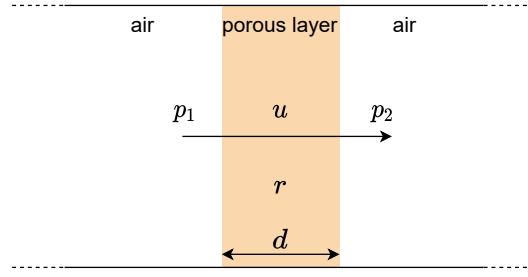


Figure 5.1: Flow resistance of the layer made of porous material.

At low frequencies, the same relation holds for acoustic quantities. As frequency increases, the reactive terms were shown to become non-negligible [12]. If such a porous layer is placed at a quarter wavelength from a rigid wall, the acoustic pressure at the back p_2 vanishes. Thus, the front surface acoustic impedance becomes equal to the material flow resistance rd :

$$Z_1 = p_1 / u = rd. \quad (5.2)$$

To obtain total absorption under normal incidence, for example, one should choose the material layer with the resistance equal to the characteristic impedance in the air. The passive absorber with a fixed position of a porous layer relative to the wall can present the absorption maxima only at discrete frequencies. Moreover, absorption of the low frequency sound requires a proportionally large system size. Placing the actively controlled transducer that ensures $p_2 = 0$ allows maintaining absorbing condition over a wide frequency range with a compact size.

5.2.2 Control design with FxLMS algorithm

The schematic of the hybrid absorption control is illustrated in Figure 5.2. Apart from the microphone for pressure minimisation p_e , the control procedure utilises a second reference microphone p_r located further away from the absorber. The algorithm is based on the adaptive LMS algorithm to increase the stability of the system [120]. Thus, it takes the reference signal $\mathbf{p}(t)$ as the input. In the tested configuration, this signal was buffered to 50 previous values. The microphone that senses pressure p_e provides the error value $e(t)$ at each time step t . The weights W of a filter change in the “LMS update” block as follows:

$$\mathbf{W}(t) = \mathbf{W}(t-1) + \mu e(t) \mathbf{p}^T(t). \quad (5.3)$$

In Equation (5.3), μ is the adaptation step size that controls how fast the algorithm converges.

After the weights update, the reference signal is filtered in the “LMS apply” block. Finally, it is inverted and leaves the controller to be amplified (not shown in Figure 5.2) and applied to the CD actuator. The diagram also contains two FIR filters of the length 50. The first one, the “path estimation” filter, takes into account the response of the CD actuator and the path between it and the error pressure p_e . The second “Feedback filter” compensates for the influence of the CD actuator operation to the signal recorded by a reference microphone.

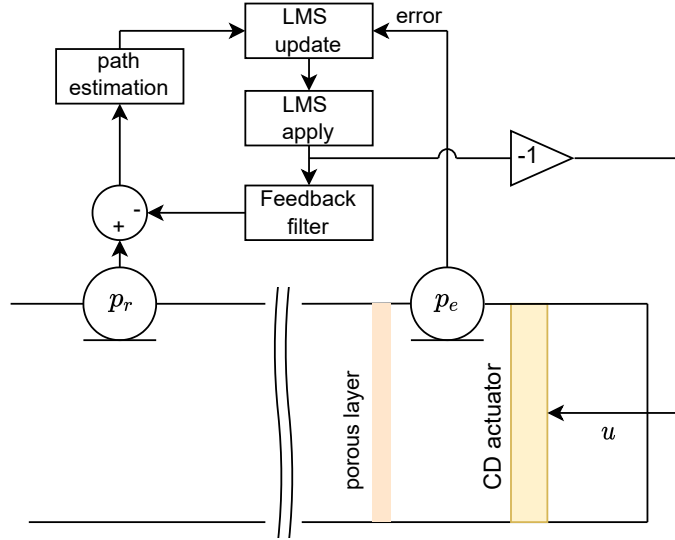


Figure 5.2: Block scheme of the adaptive algorithm for hybrid sound absorption.

The control algorithm is implemented in Matlab Simulink, and the input-output communication is realised onto a Speedgoat IO 334 Real-Time Target Machine with a 20 kHz sampling rate. First, the “path estimation” and “Feedback” filter coefficients are estimated and fixed by generating white noise with the CD actuator. Then, the weights $\mathbf{W}(t)$ of the LMS filter are adapted, generating white noise with an external sound source, and also fixed as proposed in [19]. During the measurements of sound absorption, the coefficients are kept unchanged.

5.2.3 Experimental setup

The measurements of acoustic impedance and sound absorption coefficient under normal sound incidence are performed in the impedance tube (Figure 5.3). The duct is 1.1 m long, and it has a rectangular cross-section $50 \times 50 \text{ mm}^2$. The actuator, which design is described in Section 4.1, is located at the right termination of the impedance tube and enclosed with a back cavity of the same cross-section and 20 mm depth. Such dimensions allow only plane wave propagation at frequencies below 3 kHz. The actuator is oriented with collector facing the duct, emitter wires are enclosed. With this orientation sensors in front of CD are protected from high voltage. As a passive porous layer for the hybrid absorption method, a 1.5 mm thick

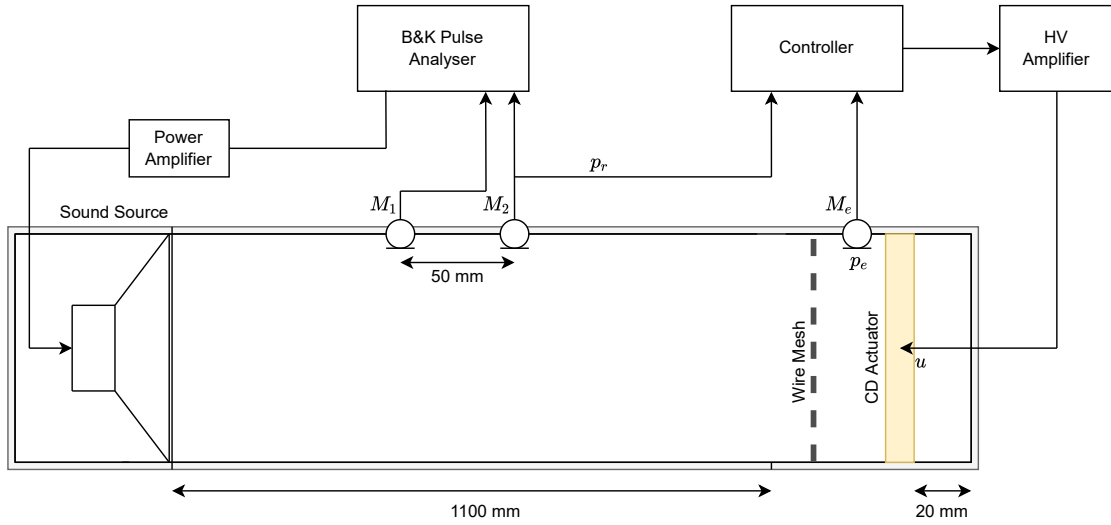


Figure 5.3: Schematic of the experimental setup for the measurements of sound absorption under normal incidence. Hybrid sound absorption method with the CD actuator is implemented.

sandwich of 4 identical wire meshes is installed¹ (inox 304L, 0.285 mm filament, resistance 120 Pa·s/m). The cumulative low frequency resistance was estimated as $1.07\rho c$ with the method proposed in [121], which is sufficiently close to the characteristic air impedance. The termination at the left is closed by a loudspeaker used to generate a bidirectional sinusoidal sweep. Two PCB130D20 microphones M_1 and M_2 placed 50 mm apart are used to derive the acoustic impedance and absorption coefficient of the CD-based hybrid absorber according to ISO-10534-2 standard [122]. Signals from these microphones are processed with a Brüel&Kjaer Pulse frequency analyser. The hardware used to control the CD actuator is depicted at the right in Figure 5.3. The error microphone M_e (PCB130D20) senses the pressure p_e between the wire mesh and the CD actuator. The microphone M_2 is also used to provide the reference noise signal p_r for control. As the controller cannot generate a high voltage (maximum 10 V), the following procedure is performed. The alternating voltage component calculated by the controller to supply the actuator (in the range of kV) is reduced by a factor of 1000 before the output. The controller is then connected in series with a floating power supply that adds positive bias voltage (8 V to achieve 8 kV) for stable corona discharge operation. The controller is then connected to a TREK 615–10 high voltage AC/DC amplifier (± 10 kV, 10 mA) which amplifies the signal back by 1000 and supplies the actuator. The performance of the active absorber is evaluated in the frequency range 100 – 2000 Hz so that the lower limit is higher than the cut off frequency of the control microphones (50 Hz), and the higher limit is sufficiently lower than the sampling rate of the controller.

¹<https://www.gantois.com/en/Catalogues.php>

5.2.4 Achieved acoustic impedance and sound absorption

The measurements of sound absorption coefficient and acoustic impedance are shown in Figure 5.4 for a passive absorber and when the control is on. The impedance is evaluated at the front face of the wire mesh. In the passive regime (blue curves), the low frequency impedance presents high absolute values of the real and imaginary parts. As frequency increases, the impedance converges to $Z = \rho c$. The related absorption corresponds to the typical performance of a quarter wavelength resonator with a matched resistance. At low frequencies, which correspond to the wavelengths much greater than the absorber size, it almost does not absorb sound. We should mention here that all absorption relates to the losses in the wire mesh. The stainless steel grounded collector plate of the CD actuator was measured to have a resistance of $0.02\rho c$. Therefore, its contribution to sound absorption can be considered negligible.

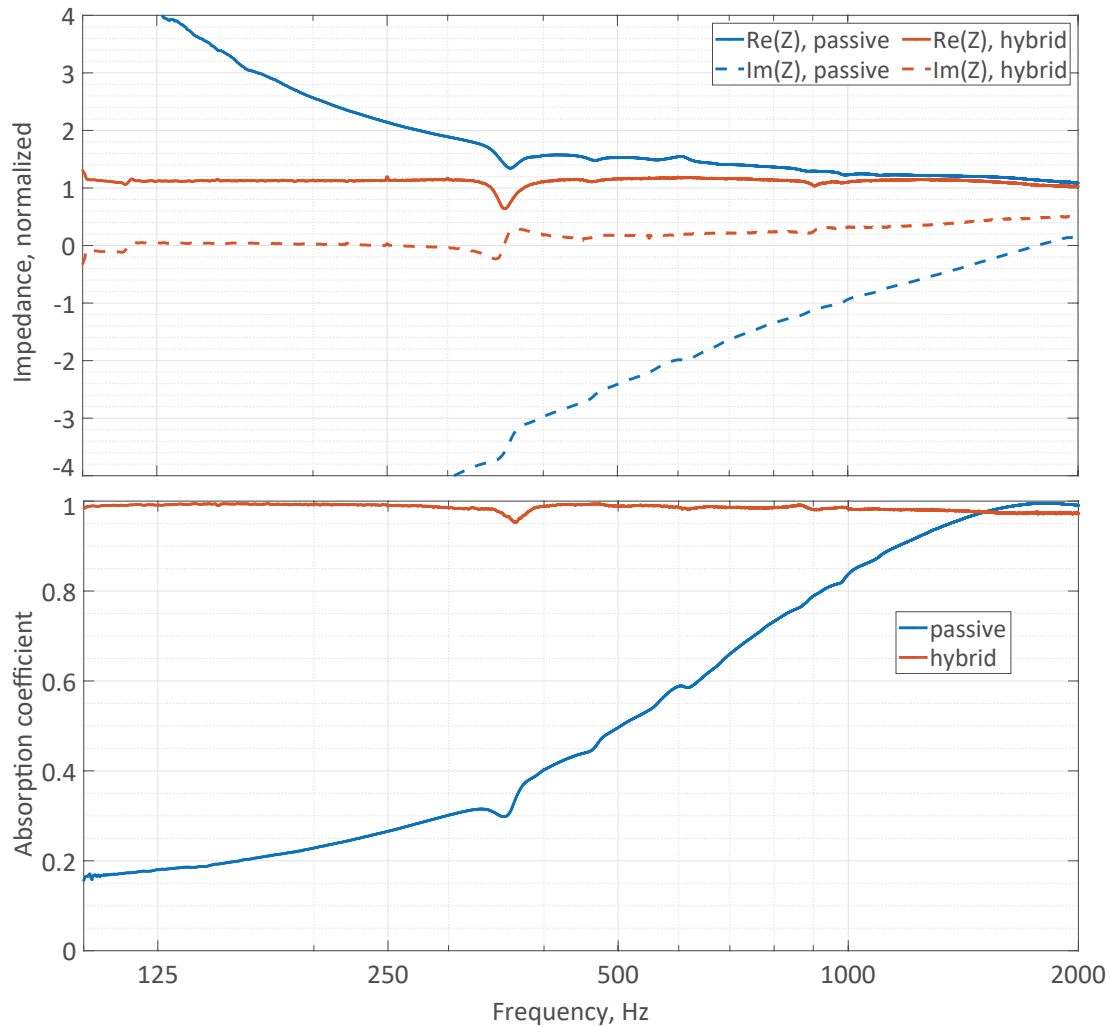


Figure 5.4: Acoustic impedance and absorption coefficient measurements of a system in passive and hybrid mode. The impedance is normalised by ρc .

When the system is in hybrid mode with the CD actuator cancelling pressure at the back of the wire mesh, it turns into a perfect broadband absorber (red curves in Figure 5.4). The average value of the achieved real value of impedance is $480 \text{ Pa}\cdot\text{s}/\text{m} \approx 1.14\rho c$ in the considered frequency range, which is close to the resistance of the wire mesh. At low frequencies, the imaginary part of the impedance remains close to zero but slightly increases above 500 Hz. As was mentioned in Section 5.2.1, the porous materials cannot be considered as a pure resistance. As the macroscopic parameters, such as porosity, and tortuosity, are challenging to evaluate experimentally, we cannot estimate at which frequency the deviation from a purely resistive behaviour starts. The absorption coefficient stays higher than 0.97 from 100 to 2000 Hz (except for the measurement artefact at 370 Hz, which can also be visible on passive measurements). The change in reactance lowers the absorption quality gradually at high frequencies. Above 2000 Hz, we can expect further degradation in the absorption performance of the hybrid absorber. Thus, the passive system may appear more efficient.

Finally, broadband sound absorption was achieved with the use of the CD actuator. However, as may be seen, only resistive target impedance can be realised with this method, and any change in the target requires the change of the passive material. An alternative method that does not present these drawbacks is proposed in the next section.

5.3 Pressure-velocity feedback impedance control

This method relies on external sensors to drive the acoustic impedance at the actuator surface to the target one. The measurement of acoustic pressure divided by the target impedance yields the particle velocity that should be created to achieve this target. The actual particle velocity is estimated independently. The difference between the estimated and desired velocity is minimised in a feedback loop to achieve the target impedance.

5.3.1 Methods to estimate particle velocity in front of corona discharge

Pressure-velocity feedback control requires the accurate estimation of both acoustic pressure and particle velocity close to the front face of the actuator. While pressure estimation is straightforward, the absence of moving parts in the actuator poses some constraints on how the particle velocity can be estimated. Indeed, several methods used for membrane transducers, such as a laser velocimeter or accelerometer, cannot be implemented here. In this study, the two approaches to estimating the particle velocity are proposed. Both of them utilise a pair of microphones. Their relative performance in terms of achieved acoustic impedance and sound absorption under normal incidence is compared in the impedance tube in the next section.

In the first method, the two microphones are simply placed in front of the CD actuator and spaced by a distance l . If there are no acoustic sources between the microphones, the acoustic pressure and velocity are linked through the Euler equation, which writes:

$$\frac{\partial p}{\partial x} = -\rho_0 \frac{\partial u}{\partial t}. \quad (5.4)$$

The pressure gradient can be approximated by the difference of pressures at the two microphone positions. The estimated particle velocity then reads:

$$v_{\text{est}} = -\frac{1}{\rho_0} \int \frac{\partial p(t)}{\partial x} dt \approx -\frac{1}{\rho_0} \int \frac{p_1(t) - p_2(t)}{l} dt. \quad (5.5)$$

In the frequency domain the equation takes the form:

$$v_{\text{est}} = \frac{p_1(s) - p_2(s)}{\rho_0 l s}, \quad (5.6)$$

where $s = j\omega$ is the Laplace variable. Such an estimation of the particle velocity implies that the distance between the microphones should be reasonably smaller than the wavelength of the acoustic signal. On the other hand, when the wavelength is much larger than l , the separation may be not sufficient for an accurate estimation of the velocity in the presence of a parasitic noise in the system. Therefore, the distance l is constrained by both the lowest and highest frequencies of interest. In this work, the considered frequency range is limited by 2000 Hz (more difficult to tackle with passive materials in a limited space). The distance l is set to 30 mm in order to remain smaller than the quarter of the wavelength at 2000 Hz and still be accurate at low frequencies.

The second approach consists in placing a passive resistive material with the microphones to estimate the acoustic velocity. A thin porous layer, for example, a wire mesh with known flow resistance R is placed between the microphones. The flow velocity through a porous layer is mostly controlled by its resistance and the same holds for the acoustic velocity at low frequencies, as in the case of hybrid absorption. Therefore, the estimation of particle velocity reads:

$$v_{\text{est}} = \frac{p_1 - p_2}{R}. \quad (5.7)$$

At high frequencies, inertial forces become non-negligible, and the Equation (5.7) may not hold anymore. In this approach of estimating the particle velocity, the microphones can be placed closer than in the first method since the pressure drop is assumed to occur between each side of the resistive layer, which makes the system more compact.

5.3.2 Control design

The control schematic for the pressure-velocity feedback is shown in Figure 5.5 for both approaches of particle velocity estimation. Simple proportional feedback control is realised in this study since it does not perturb the phase of the output signal, which is essential for real-time impedance control. The rectangular blocks represent continuous-time transfer functions which should be discretised and implemented on the control hardware.

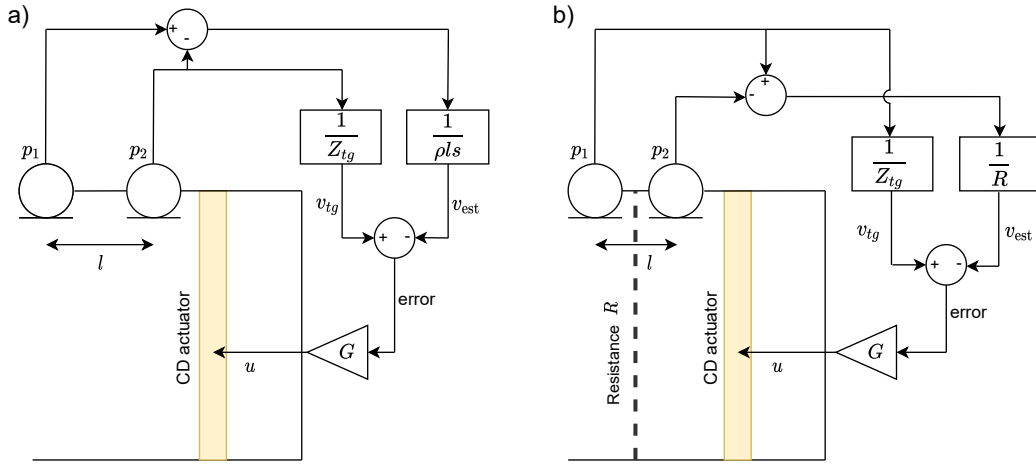


Figure 5.5: Block diagram of the pressure-velocity feedback control of the corona discharge actuator. a) the particle velocity is estimated based on Euler equation. b) particle velocity is estimated with the use of a known resistive layer.

In Figure 5.5a, the microphone p_2 provides the measurement of the total acoustic pressure in front of the actuator. The target velocity is estimated as p_2/Z_{tg} , where Z_{tg} is the target impedance. The estimated velocity v_{est} is obtained from Equation (5.6). The difference between v_{tg} and v_{est} yields the error signal, which should be minimised. The error is further amplified by a dimensional gain G and forms a voltage u that is applied to the actuator.

In Figure 5.5b, the target velocity v_{tg} is calculated with the use of microphone p_1 since the total impedance presented by an active absorber is the one on the front face of the resistive layer. Velocity v_{est} is calculated according to Equation (5.7). The rest of the control circuit is similar to the one already described. The target acoustic impedance can be changed digitally in the controller to adjust the system to optimal absorption in various configurations. The transfer function $1/Z_{tg}$ should be proper to keep the control stable. Since it is possible to set a complex frequency-dependent impedance, this method can be advantageous compared to the hybrid absorption method under grazing incidence.

5.3.3 Experimental setup

The measurements of acoustic impedance and sound absorption coefficient under normal sound incidence are performed in the impedance tube.

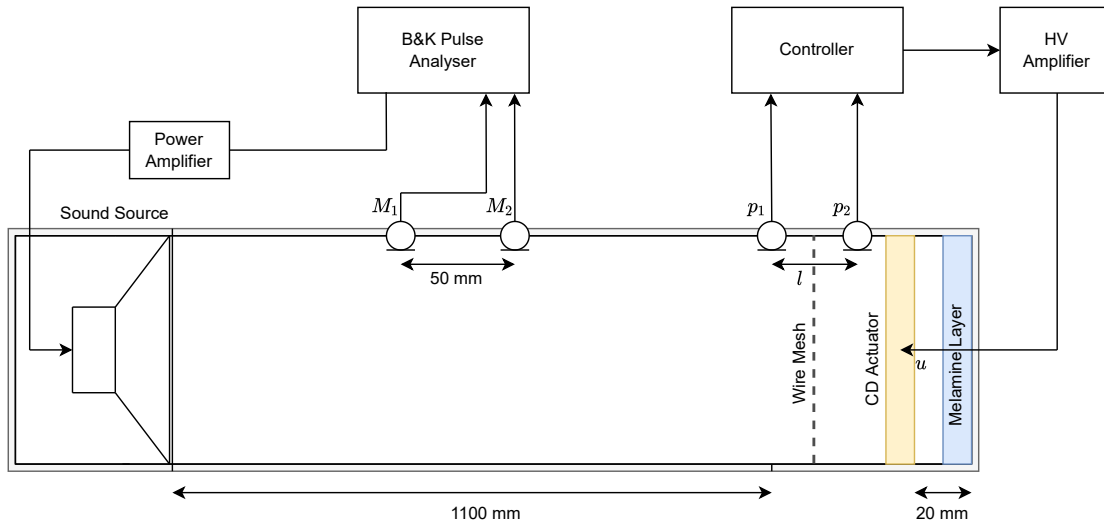


Figure 5.6: Schematic of the experimental setup for the measurements of sound absorption under normal incidence. Pressure-velocity feedback impedance control of the CD actuator is implemented.

The duct parameters, the actuator, and the measuring system are the same as the one described in Section 5.2.3. A 10 mm-thick layer of melamine foam is placed in the back cavity in order to increase control stability (due to the presence of the hard wall close to the actuator). A pair of PCB130D20 quarter-inch microphones sense the pressure at positions p_1 and p_2 . Therefore, to estimate the velocity with the first approach, the separation $l = 30$ mm was chosen as a compromise to keep the sound absorbing system small but still work in the considered frequency range. When v_{est} is measured according to the second approach, the wire mesh with a thickness of 0.3 mm and flow resistance $R = 0.3\rho c$ is installed, and the microphone spacing $l = 9$ mm. The control schemes of Figure 5.5 are implemented in a real-time platform Speedgoat IO-334 programmed with Matlab Simulink. The discretised loop runs at a frequency 50 kHz.

5.3.4 Achieved acoustic impedance and sound absorption

The sound absorption performance was evaluated using both approaches for particle velocity estimation. The environmental conditions and levels of noise source excitation are kept the same during the experiment. The feedback gain G of the feedback loop is always set to the highest value until the control system becomes unstable. The target impedance is set to the

characteristic impedance in the air $\rho c \approx 418 \text{ Pa}\cdot\text{s}/\text{m}$ in order to achieve full absorption under normal sound incidence.

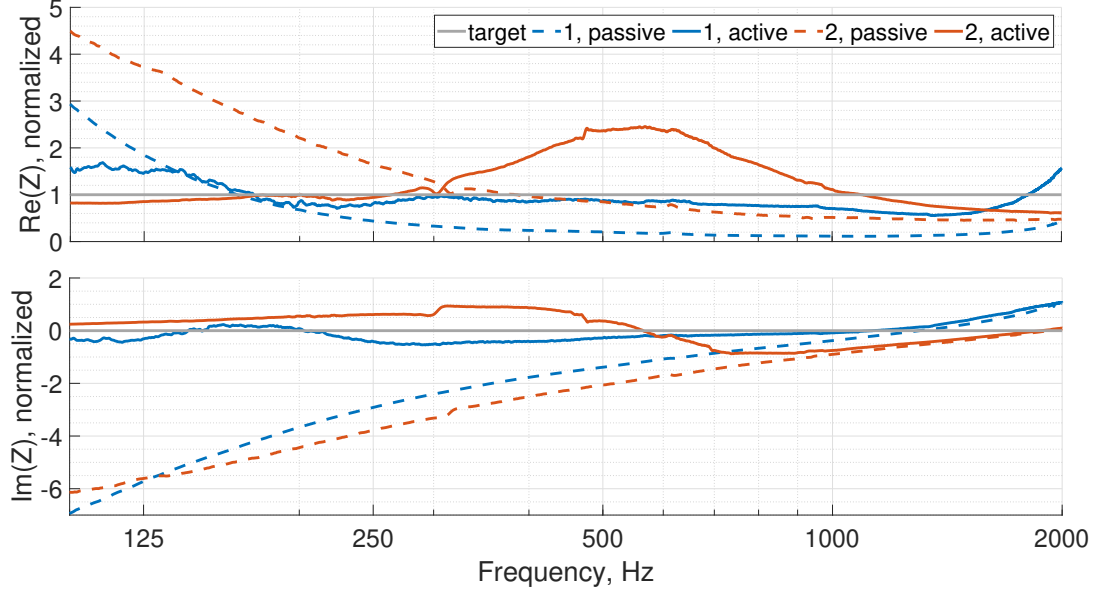


Figure 5.7: Real and imaginary parts of the measured acoustic impedance in passive and active modes. Number 1 corresponds to configuration with velocity estimation according to Equation (5.6), 2 - according to Equation (5.7) with resistive material between microphones. Values are normalised by ρc .

The measured impedances of the CD actuator in passive and active cases are presented in Figure 5.7. The reference plane where the impedance is evaluated is different for the two velocity estimation methods. For the Euler-based velocity estimation, it is placed at the centre between the two microphones; for measurements with a resistive layer, the impedance is estimated at the position of the first microphone (see Figure 5.6). In the passive regime, the stiffness of the actuator enclosure controls the low frequency impedance dynamics, which is represented by high magnitudes of impedance and negative imaginary part (dashed lines in Figure 5.7). At frequencies above 1000 Hz, the behaviour of the impedance with two velocity estimation methods differs due to the slightly different position of the evaluation plane and the presence of the wire mesh in the second case. In the active case, when the actuators are controlled, the real part of the impedance shifts close to ρc while the imaginary part tends to zero (solid lines). At frequencies above 1 kHz, the impedance curves deviate from the target closer to the passive dynamics. This can be explained due to several reasons. First, the passive absorption increases and shifts the impedance closer to ρc (passive curve 2). Second, the velocity estimation in both cases becomes less accurate and deviates the achieved impedance from the target.

The absorption coefficient corresponding to the achieved impedance is depicted in Figure 5.8. In the passive case, the system does not have any means to absorb sound at low frequencies.

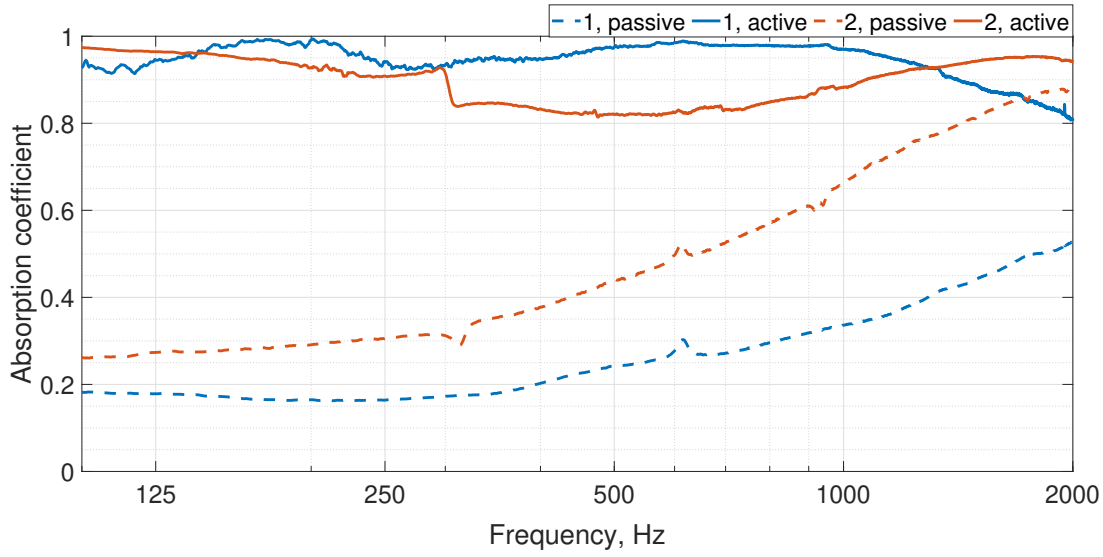


Figure 5.8: Measured absorption coefficient of the CD actuator with a pressure-velocity feedback control.

For the velocity estimation through the Euler equation, all the sound energy dissipation happens due to the installed thin melamine layer at the back. As a result, the absorption coefficient reaches only 0.5 at 2 kHz. In the second configuration, the presence of a resistive mesh approximately 40 mm from the rigid wall forms a quarter wavelength resonator. This visibly increases the overall absorption performance and particularly at high frequencies. In contrast to the passive case, the impedance control of the CD actuator increases sound absorption reaching levels higher than 80% in the whole frequency range of interest. For the first active configuration, the gradual reduction of absorption coefficient can be seen above 1000 Hz. As already mentioned, the approximation of pressure gradient by a simple difference is less accurate at high frequencies, which leads to errors in velocity estimation. The absorption achieved with the second approach has a local decrease in the middle range that corresponds to the strongest mismatch between the achieved and target impedances in Figure 5.7. One can suggest that the wire mesh is not a pure resistance anymore at high frequencies that influences the estimated velocity. However, as the passive absorption in the second case significantly increases at high frequencies, this effect is compensated. To sum up, the CD actuator can act as a broadband sound absorber with simple proportional feedback control, which is not achievable with electrodynamic transducers over such a bandwidth.

5.4 Application to acoustic liners

Modern development of aircraft engines tends to use larger rotating parts with the aim of reducing the consumption of fuel. As a result, the acoustic noise emitted by the engine presents more energy at lower frequencies [123, 5]. This brings a new challenge in aircraft engine noise

reduction since the low frequencies should be absorbed with minimal space for acoustic treatment. The only available place for absorbers is the wall of the engine nacelle surrounding the rotor. The conventional resonator-based acoustic treatment is called “acoustic liner”. It was illustrated in Figure 1.2 in the introduction. These conventional liners based on the microperforated panels [124, 125] may not satisfy the noise reduction requirements of modern engines anymore, and new, deep sub-wavelength and broadband at the same time, concepts should be developed to face this challenge.

Among the passive methods, various membrane and metamaterial-based liner concepts were recently proposed [25, 126, 127]. With relatively low mass and small thickness, they can address such low frequency noise. However, greater bandwidth would be of high importance, and the application of these concepts is still to be evaluated in realistic environmental conditions.

Alternatively, active sound absorbing concepts were also studied for the acoustic liner application [128, 91, 129]. The operation can often be adjusted to focus on different frequency bands, which is particularly valuable in the case of engine noise reduction as it has tonal components with varying frequencies in different regimes. However, at high sound pressure levels, the displacement of the transducer’s membrane can become nonlinear or even lead to its damage. In addition, large arrays of electrodynamic actuators can be relatively heavy for aircraft applications due to the presence of heavy permanent magnets in construction. As discussed in the introduction, alternative piezoelectric transducers have a rather narrow frequency response and, thus, controllable bandwidth [128]. Therefore, corona discharge actuator can potentially offer a more flexible design, reduced weight of the liner, mechanical robustness, and greater bandwidth for liner application.

In this section, we implement the hybrid absorption concept and pressure-velocity feedback control in a liner prototype based on the CD actuators.

5.4.1 Noise reduction under grazing incidence

An acoustic liner is integrated into a wall of the air channel (engine intake or bypass channel), where the sound propagates along the surface of the treatment. Therefore, noise reduction under grazing incidence demands adjusting the control strategy and the CD actuator geometry.

When sound absorption is performed under normal incidence, as in the impedance tube, the active absorber should act as a whole because the wavefront is parallel to the actuator’s surface. In other words, the acoustic pressure at any point on the actuator surface is the same. In the case of grazing incidence, in particular when mounted on the duct wall, the sound propagates along the actuator surface. This limits the maximal size of an active cell unit for a given wavelength of operation, otherwise, the acoustic pressure and velocity acquired with the sensors at a certain location do not correspond to the average value across the whole active surface.

In a two dimensional infinite duct with height h , the analytical solution of the wall impedance

Z_{opt} that maximises the modal sound attenuation is given by Cremer's formula [130]:

$$Z_{\text{opt}} = (0.929 - j0.744) \frac{2fh}{c}. \quad (5.8)$$

Although the Equation (5.8) is obtained for an infinite duct, the wall section that has the impedance close to Cremer's one in a finite length duct imposes sufficient sound attenuation [131]. Therefore, this formula can serve as a reference for the target impedance.

5.4.2 Prototype design and flow duct facility

The measurements were conducted in a rectangular flow duct with a cross-section of $40 \times 50 \text{ mm}^2$ in LAUM laboratory in Le Mans (Figure 5.9). On one side, it is connected to a fan that generates the airflow. Two anechoic terminations are placed at both ends of the duct. The acoustic measurements are performed by six flush-mounted microphones $M_1 - M_6$. Two compression chambers are mounted at the two ends of the duct to be able to generate sound either downstream (in the direction of flow) or upstream (in the direction opposite to flow). An acoustic excitation signal consists of discrete sinusoidal waves with frequencies from 100 to 2000 Hz and 10 Hz step. The constant amplitude of the incident wave is maintained in the considered frequency range.

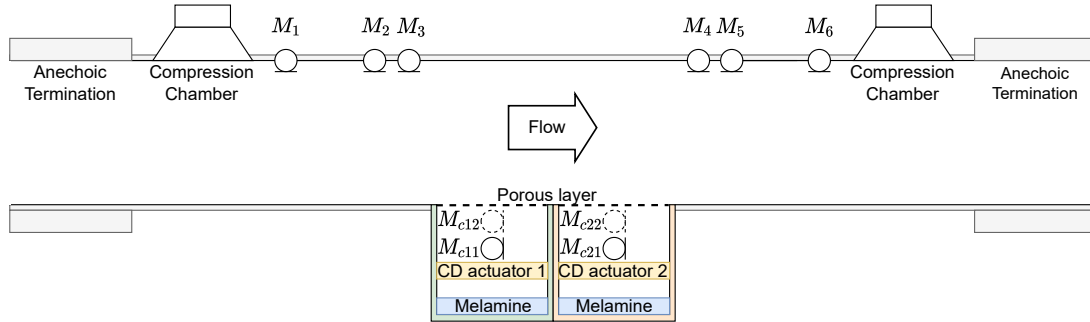


Figure 5.9: Scheme of the rectangular flow duct for measuring the liner absorption under grazing incidence. The second control microphone (M_{c12} and M_{c22}) is only used for direct feedback impedance control. The depth of the cavity is different for hybrid absorption and direct impedance control methods.

We evaluated the transmission losses in the duct induced by the presence of the active liner. For this, the scattering matrix of the CD-based acoustic liner was computed using two different configurations: in the first only the upstream source is working (on the left in Figure 5.9, marked as + further in the text), in the second only the downstream source is on (marked as -). The measured signal is averaged at each frequency over 400 cycles without flow and 1000 cycles with the flow. The transmission coefficients T^+ and T^- are obtained from the scattering matrix [132]. Then, the transmission losses can be calculated as follows:

$$TL^{\pm} = 20 \log_{10} \left| \frac{1}{T^{\pm}} \right|. \quad (5.9)$$

The acoustic impedance achieved by the sample is deduced using the inverse method, which is based on the multi-modal calculation of the acoustic field in a 2D lined channel with a uniform flow [133].

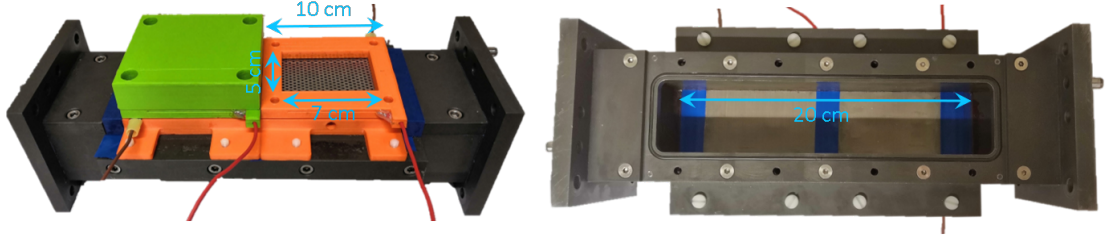


Figure 5.10: Test section with the plasma-based liner prototype mounted on a side wall. Left - two active cells comprising the liner (one is partially disassembled for illustrative purpose). Right - view from the duct inside, top cover is removed.

The active liner setup in this study consists of the two active cells (Figure 5.10). Each cell covers the wall area of $100 \times 50 \text{ mm}^2$ in the duct, but the hollow discharge area is limited to $70 \times 50 \text{ mm}^2$. Given the active length of the actuator, the control cannot be efficient at frequencies higher than 2 kHz. For higher frequency absorption, shorter in length cells would be needed. Each cell includes one (M_{c11} and M_{c21} in case of hybrid sound absorption) or two microphones (M_{c11} , M_{c12} and M_{c21} , M_{c22} in case of direct impedance control in Figure 5.9). For simplicity, both cells always have the same control law while operating. However, different target impedances can be implemented if needed. The two actuators operate independently; the control loops do not have any cross terms. In the case of hybrid absorption, both active cells share the same reference signal. However, different microphones for upstream and downstream measurements are used. The microphones M_3 and M_4 (Figure 5.9), which are located 20 cm from the test section borders, provide the reference signal for upstream and downstream measurements, respectively. The calibration procedure described in Section 5.2.2 is performed for each cell individually.

The actuators are built in a modular way to be able to easily change the configuration. The cells are fixed side by side to the wall of the duct section. First, the cavity with the microphones is screwed. Then, the collector electrode plate is placed. The frame with corona electrodes is placed next. Finally, the 20 mm cavity with a 10 mm melamine layer finishes the assembly.

Figure 5.10 illustrates the liner assembly for the hybrid control method. Pressure-velocity feedback impedance control requires a larger cavity that hosts two microphones and is illustrated in Figure B.5 in Appendix B. As was discussed in Section 5.2.1, the hybrid absorber requires a porous layer whose resistance is matched to the optimal one. As can be seen, the

drawback of this technique is that there is no simple possibility to influence the imaginary part of the acoustic impedance. Although the optimal impedance in Equation (5.8) contains a reactive part changing linearly with frequency, in our case, it is always set to zero. Moreover, the resistance is also proportional to frequency and, with a duct height $h = 40$ mm, varies from $0.02\rho c$ to $0.44\rho c$ in the 100-2000 Hz frequency range. Therefore, a wire mesh with the resistance of approximately $0.25\rho c$ is chosen so that it lies in the middle of the considered interval. For the second method, a thin layer of Kevlar (weight = $61 \text{ g}\cdot\text{m}^2$, thickness = 0.12 mm) is glued on the cavity which is done for measurements with the mean flow to prevent it from entering inside the liner.

5.4.3 Performance without mean flow

First, the measurements were conducted without airflow in the duct. The magnitude of the incident wave was maintained at the level of 90 dB. Figure 5.11 on the left shows the transmission losses induced by the hybrid system when the CD actuator is off and on. In the passive regime (blue curves), the liner presents a resonant response as expected. The low frequency attenuation is almost negligible. At high frequencies, the transmission losses increase and reach a peak value of 17 dB at 1500 Hz. The corresponding educed normalised impedance is illustrated on the right of Figure 5.11. As a reference, the optimal impedance from Equation (5.8) for $h = 40$ mm is also provided. One can see that the maximal value of transmission losses corresponds to the frequency region where both the liner resistance and reactance are the closest to Cremer's impedance. However, the passive liner resistance does not fall below 1, which means $p = 0$ condition behind the wire mesh is not reached in the considered frequency range.

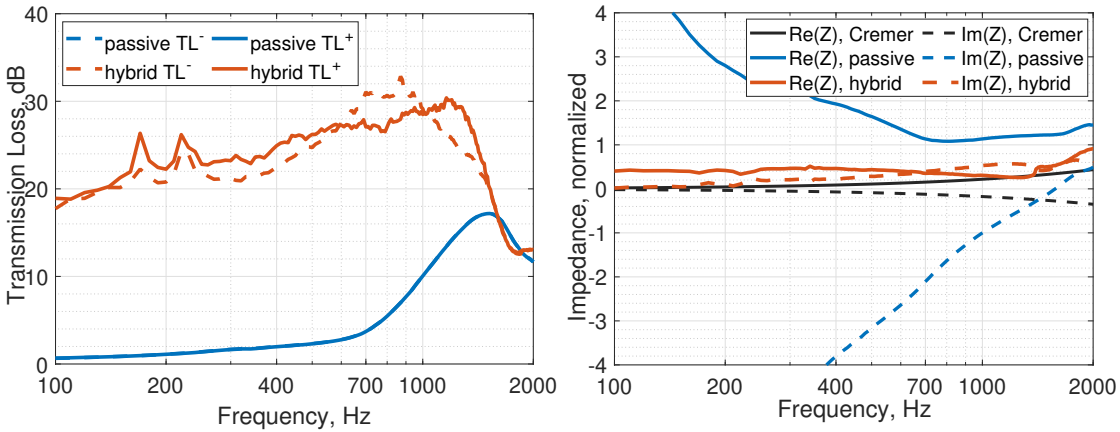


Figure 5.11: Transmission loss (left) and normalised acoustic impedance (right) of hybrid absorption system in comparison to passive behaviour without mean flow. + sign corresponds to measurement with the upstream source on, – with the downstream source on. Blue curves of passive measurements coincide. The Cremer impedance is calculated for a duct height of 40 mm.

In the hybrid mode, the absorber induces broadband sound attenuation starting from low frequencies. In the frequency range from 140 Hz to 1500 Hz, the transmission losses exceed 20 dB with a maximal value around 30 dB at 1000 Hz. It can be noticed that the TL^+ and TL^- curves are not strictly similar. This phenomenon occurs because of the calibration process. Since the flow duct is not symmetric with respect to the test section (the duct parts in the upstream and downstream directions together with anechoic terminations are built differently), the estimated filters do not coincide for the opposite directions of sound propagation. The impedance presented by the hybrid liner has both real and imaginary parts closer to Cremer's target. The mean value of resistance is $0.4\rho c$, which is higher but close to the expected one. The reactance has a similar trend as in the case of normal incidence. At 200 Hz, it starts deviating from zero towards the positive direction. At frequencies above 1500 Hz, the impedance furthers from the optimal one, which results in a drop in transmission losses. It should be mentioned here that the educed impedance is calculated as the average value over the whole liner, which is 20 cm long. However, as described in Section 5.4.2, only 75 % of the liner surface is active, the rest being the hard wall. Therefore, such deviation of the achieved impedance relative to the target is expected.

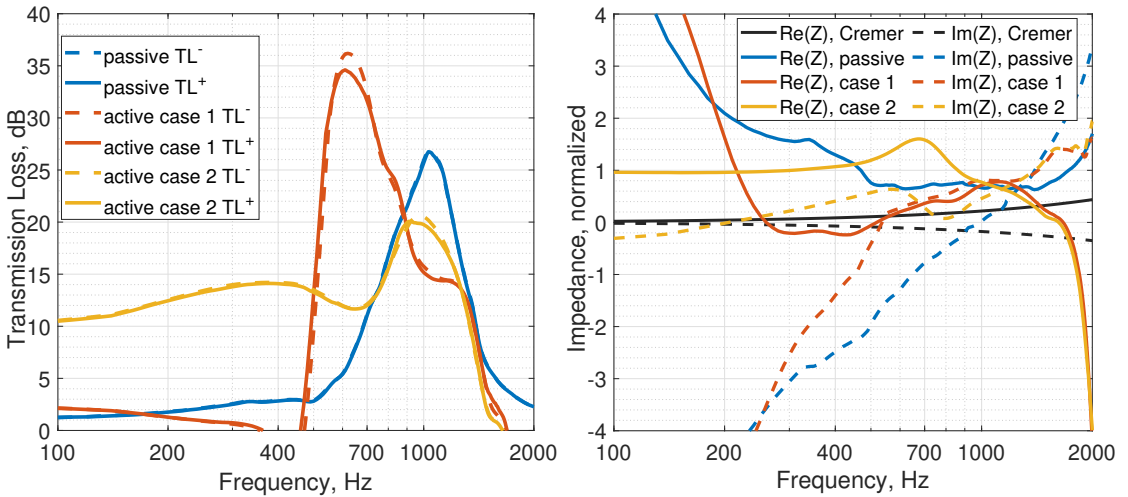


Figure 5.12: Transmission loss (left) and normalised acoustic impedance (right) of direct impedance control system in comparison to passive behaviour without mean flow. The Cremer impedance is calculated for a duct height of 40 mm.

Pressure-velocity feedback impedance control was also tested in the duct. Although a frequency-dependent impedance can be targeted with this method, the exact formulation of Cremer's optimal impedance cannot be realised on a real-time platform since it is not representable as a continuous time transfer function. Instead, the following target impedance is chosen:

$$Z_t = s a_m M + a_r R + a_c \frac{1}{sC}, \quad (5.10)$$

Table 5.1: Parameters for pressure-velocity feedback impedance control with target impedance from equation 5.10. $M = 0.044 \text{ kg}\cdot\text{m}^{-2}$, $R = 35 \text{ Pa}\cdot\text{s}\cdot\text{m}^{-1}$, $C = 4.3\text{e-}7 \text{ m}\cdot\text{Pa}^{-1}$

Parameter	a_m	a_r	a_c
Control case 1	0.5	2	0.2
Control case 2	0	2	0

where s is the Laplace variable. This equation resembles the passive response of an electrodynamic loudspeaker (see Section 1.2.2). It also fits well the response of the enclosed CD actuator around passive absorption peak, as the combination of the air volume with a slightly resistive grid backed with a cavity. The target impedance is written as a sum of an acoustic mass M , resistance R , compliance $\frac{1}{C}$ with the corresponding dimensionless coefficients a_m, a_r, a_c . Therefore, if all coefficients equal one, formula (5.10) corresponds to the passive case. By changing these parameters, we can realise various control scenarios. The values of M, R, C as well as a_m, a_r, a_c for 2 implemented control cases are listed in Table 5.1.

Figure 5.12 presents the transmission losses and achieved impedance in the passive regime and two control cases without the mean flow. The passive liner absorbs sound locally at around 1050 Hz. The maximal absorption occurs at lower frequencies than in the hybrid mode because of the deeper cavity hosting the two microphones. In control case 1, a high absorption peak is obtained around 620 Hz with a transmission losses value of 35 dB. As can be seen from Equation (5.10), the target impedance is purely real with magnitude $a_r R$ at frequency $f_r = \frac{1}{2\pi} \sqrt{\frac{a_c}{a_m C M}}$. Around this frequency, the impedance is relatively close to Cremer's optimal with both small resistance and reactance. Changing the ratio $\sqrt{a_c/a_m}$, we can shift f_r and, as a consequence, we can influence the frequency of maximal attenuation. However, one can notice that while remaining stable, the control loses passivity, which is indicated by locally negative achieved resistance and negative transmission losses. The active case 2 targets a purely resistive impedance that corresponds to more broadband transmission losses but with lower maximal values than in the first case. Several more control cases without mean flow are shown in Appendix B in Figure B.6.

The achieved impedances differ significantly from the target ones with pressure-velocity feedback, as can be seen in Figure 5.12. There are several arguments contributing to this. As was described in Section 5.3.2, the target impedance is realised between the two control microphones. Since the distance between the microphones is 30 mm, the target impedance plane is almost 20 mm away from the duct wall, which creates discrepancies. Moreover, the Kevlar layer impacts the final result as an additional porous layer. Finally, as was already mentioned, only 75 % of the liner is active. All these reasons also lead to the strong deviation of the achieved impedance from the target at high frequencies. Nevertheless, the two different control cases of pressure-velocity feedback demonstrate a broad range of control possibilities, which can be useful for absorbing different types of noise.

5.4.4 Performance in presence of mean flow

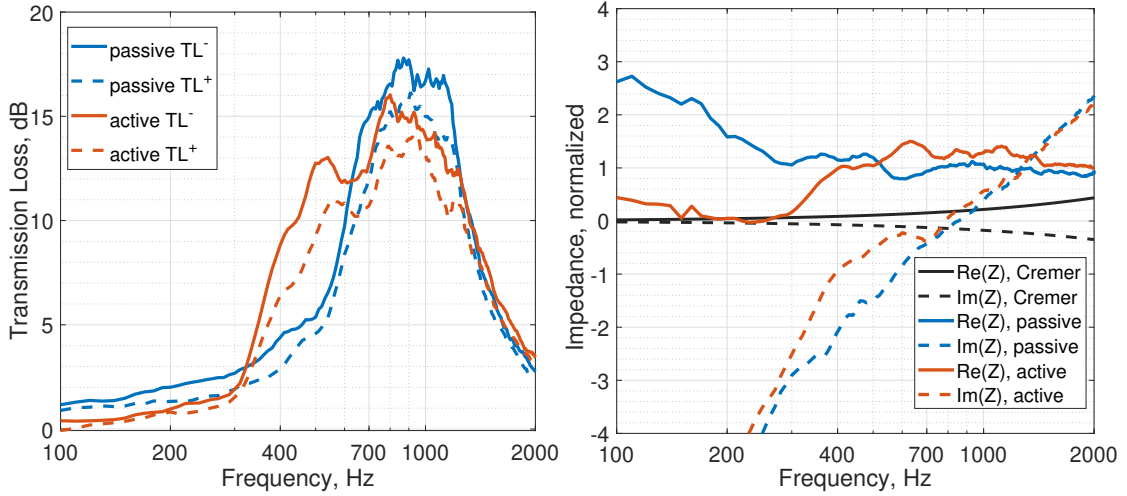


Figure 5.13: Transmission loss (left) and normalised acoustic impedance (right) of direct impedance control system in comparison to passive behaviour in a mean flow with $M = 0.05$. The Cremer impedance is calculated for a duct height of 40 mm.

Pressure-velocity feedback impedance control was tested in the presence of a mean flow with velocity $17 \text{ m}\cdot\text{s}^{-1}$ (Mach number 0.05). Another Kevlar layer was added to the liner, otherwise, the flow noise was saturating the CD output signal. As a consequence, the total resistance presented by the liner was increased. The transmission losses with calculated impedance in a passive regime and one active case are shown in Figure 5.13. For both passive and active cases, the transmission of waves propagating from upstream and from downstream is not the same. Acoustic waves propagating in the same direction as the flow are transmitted better, thus, the transmission losses are lower, which is a typical effect in such a configuration. Passive absorption is concentrated in the frequency range from 700 to 1100 Hz. The active case, illustrated in Figure 5.13, has the same control parameters as the case 1 without the flow. Although the transmission loss values are 2-3 dB lower than in the passive operation, the absorbing performance extends toward lower frequencies. Below 200 Hz, the control is inefficient due to the implemented high pass filtering of the input signals. The estimation of particle velocity in front of the CD actuator involves an integration step. In the presence of flow, which produces a strong non-periodic low frequency noise, the estimated velocity accumulates the DC offset that leads to an offset in the output voltage signal. Such an issue can shift the operation of the actuator out of the corona discharge region and either result in too low voltage or too high voltage leading to an electrical arc. High pass filtering is a measure against this, but it makes the control inefficient in the low frequency range due to the phase mismatch. Some other examples of control cases with the mean flow are provided in Figure B.7 in Appendix B.

In the presence of a mean flow, the optimal Cremer's impedance should be corrected by the factor $1/(1 + M)^2$, where M is a flow Mach number [134]. However, at tested velocities, the

difference in optimal impedances does not exceed 10 %, so no change was applied to the target impedance.

Hybrid absorption was not able to counteract the flow noise inside the liner. The sound pressure level at the error microphone exceeded 95 dB, and the CD actuator could not minimise the pressure in the cavity because the alternating output voltage component was exceeding the limits to stay linear.

5.4.5 Influence on the flow noise

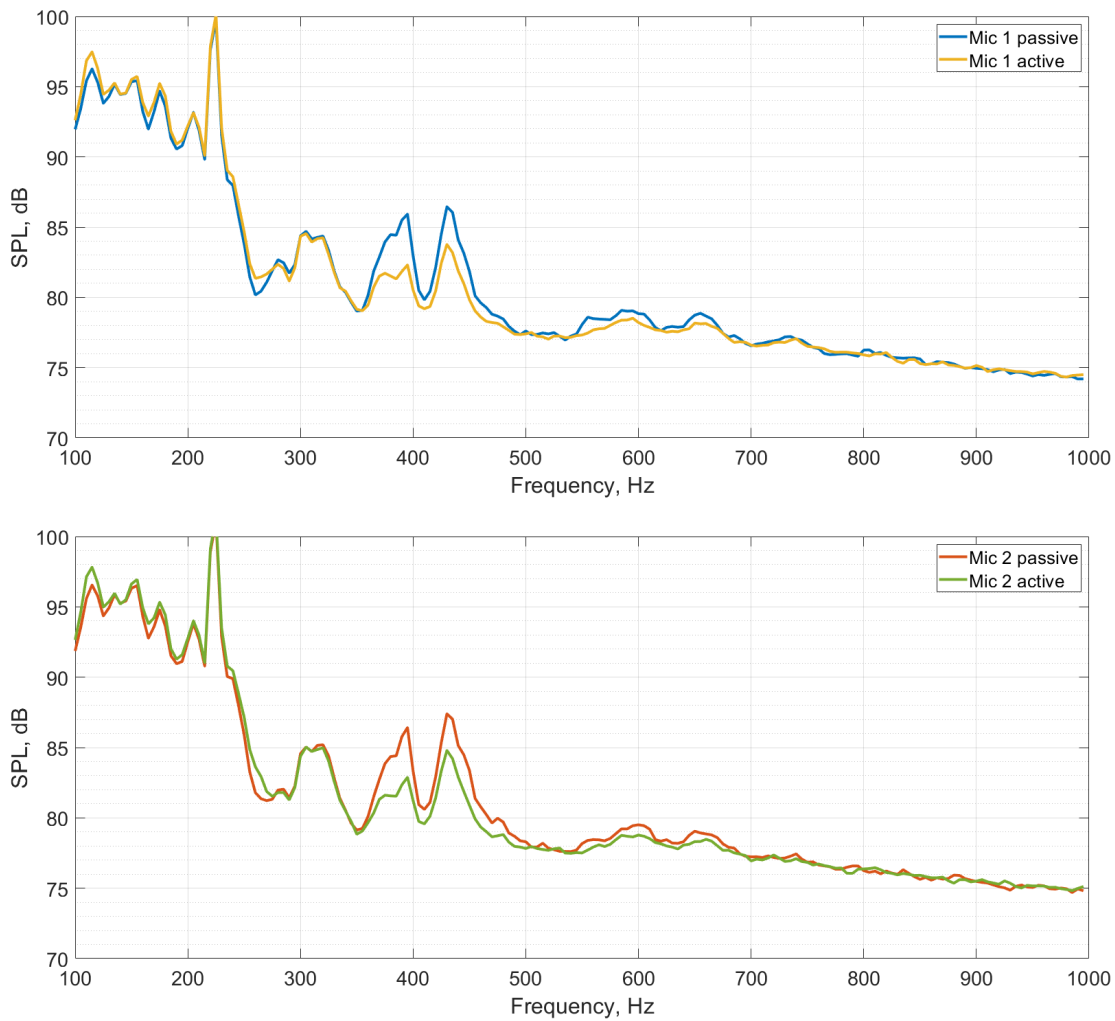


Figure 5.14: Sound pressure levels of broadband noise created by the flow in the duct. Passive – actuators are off, active – actuators are on with pressure-velocity feedback. Signals are recorded by 2 closest downstream microphones M_4 and M_5 .

It is not possible to totally exclude the flow noise from the control. The pressure perturbations created by the turbulent flow are captured by the microphones and further processed in the

control algorithm. Therefore, in addition to the target tonal noise to be attenuated, plasma actuators also tend to slightly reduce the broadband flow noise in the duct. Figure 5.14 shows the influence of the active impedance control method on the flow noise. In the absence of any additional acoustic excitation from the loudspeakers, the downstream microphones recorded the signal produced by the mean flow with Mach number $M=0.05$. The comparison is shown on two microphones when the plasma liner is passive and active. The sound pressure levels with the active system are slightly lower in the frequency range 350-700 Hz compared to the passive case recorded by the same microphones. Reduction of turbulent noise can be considered as the laminarisation of the flow in the duct, which could be of interest for flow control applications.

5.5 Conclusions

In this chapter, the application of the corona discharge actuator to impedance control was investigated with two feedback control methods. Relying completely on the external sensors, these techniques do not require any knowledge of the transducer except its sufficient linearity.

Hybrid passive-active impedance control relies on the pressure release condition behind the porous layer, which leads to the surface impedance in front of the layer equal to its flow resistance. In the performed experiments in the impedance tube, the resistance was matched to the characteristic impedance in the air to target the absorbing condition. The use of the FxLMS algorithm with the CD actuator allowed for achieving perfect broadband sound absorption. In the experiments under the grazing incidence, the resistance of the porous layer was adjusted for a particular flow duct facility to induce broadband sound attenuation with the maximum in the middle of the considered frequency range. Although there is no simple digital way to change the target impedance, the achieved performance both in the impedance tube and in the duct without flow is remarkable.

Direct impedance control in a pressure-velocity feedback configuration was also tested. A proportional type of feedback was realised. Two methods of particle velocity estimation were proposed, which involve two microphones separated by either an air gap or a porous layer. Since there is no physical moving membrane, which separates the air medium, a compact solution such as an accelerometer on the membrane or a microphone in the back cavity [135] cannot be implemented. As a consequence, the sensing system appears to be relatively bulky (15 to 35 mm depending on the approach) compared to the CD actuator (7 mm for electrodes + 20 mm enclosure). On the other side, we confirmed that due to its non-resonant response it is possible to control the real target impedance in a wide frequency band which is not feasible with electrodynamic loudspeakers or piezoelectric transducers. The experiments under oblique sound incidence showcased that various control scenarios can be realised by changing the target impedance digitally, for example, maximising the transmission losses in a selected band.

One important aspect is that the experiments were conducted with relatively low levels of

the incident wave around 90 dB. At higher SPLs, the alternating voltage of the CD actuator exceeded the specified limit of 1 kV (to not exceed the THD of 10%). Therefore, the sound sources and the control should be further investigated to see what are the current limitations. It is performed in the next chapter, where we make an effort to design a single sensor system for controlling the CD actuator, which is more compact and provides more data on its electroacoustic operation.

6 Feedforward model-based impedance control of corona discharge actuator

6.1 Introduction

In the preceding chapter, a feedback-based method has been applied to impose a desired acoustic impedance at the interface of the corona discharge actuator. It seems to be an appropriate solution if the transducer's dynamics is complicated to estimate, it varies over time, or placed in the environment, that is regularly changing (static pressure, temperature, humidity). The direct estimation of particle velocity and acoustic pressure provides the necessary information for active control. We demonstrated that, without specific knowledge of the CD actuator electroacoustic operation, it is possible to achieve a broadband control of impedance, which can be adjusted to absorb sound. Hybrid absorption is limited in the range of impedances that can be realised: only one per configuration and real-valued. On the other hand, the performance of pressure-velocity feedback is limited by the accuracy of the velocity estimation and stability. Moreover, as we have seen in Chapter 5, the real-time velocity measurement in front of the actuator is not straightforward and space consuming, which limits the advantage of a very thin actuator. Thus, it is of interest to reduce the total size of the system for space sensitive applications, such as acoustic liners for aircraft noise reduction.

An alternative method of direct impedance control consists in describing the transducer dynamics analytically. If the actuator's model is known, it is possible to achieve broadband sound absorption by applying a feedforward type of control. The model can potentially avoid the velocity estimation and use only one pressure sensor. The usage of a single microphone in a control scheme is rather cost effective and easy to implement for industrial applications. Moreover, the control system can become more compact in the case of the corona discharge actuator. Although a precise identification of the transducer's mechanical and electrical parameters is required prior to operation, such architecture makes the control scheme more

stable and easier to process [16]. Since the technique does not rely on the absorbing properties of any passive material, it generally allows targeting frequency-dependent impedances and changing the target numerically. As a result, electroacoustic liner prototypes with feedforward control demonstrated their absorption performance in duct noise attenuation under grazing sound incidence [91, 136]. Thus, developing a CD-based impedance control system appears to be an appealing direction.

The motivation of this chapter is to develop a real-time impedance control concept for the corona discharge actuator, which relies on the electroacoustic principles of the transducer. The first part aims at deriving the control transfer function that involves the analytically estimated heat and force sound sources. It is followed by the numerical simulation of the control, identification of the most sound absorbing configuration and experimental validation. The control cases with different target impedances in addition to ρc are presented.

6.2 Development of electroacoustic analytical model of corona discharge for control

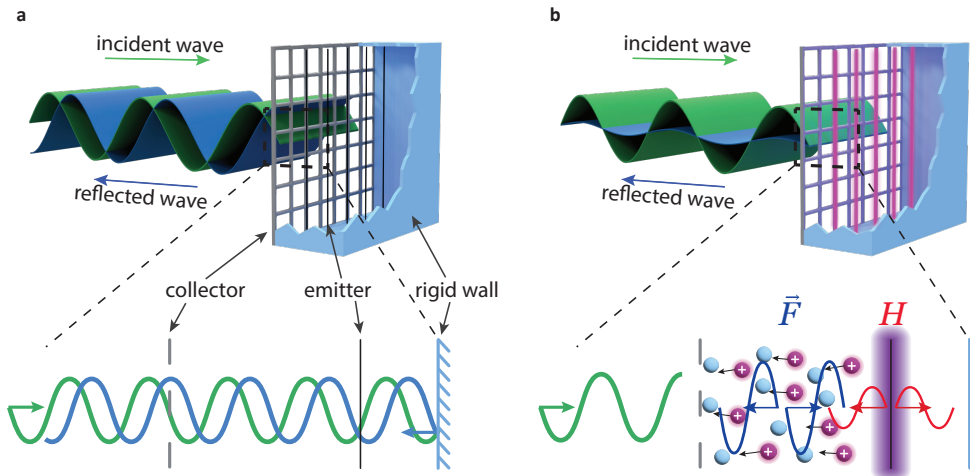


Figure 6.1: The principle of sound absorption with the corona discharge closed in a box. In passive regime (a) the actuator behaves as a rigid termination with electrode grids transparent to sound. In active regime (b) heat H and force \vec{F} sound sources are operating in order to suppress reflected wave. Shape of the sinusoidal wave from the heat source (red) and force source (blue) represents the monopolar and dipolar property correspondingly.

When the actuator is not powered, it is almost transparent to sound waves. As illustrated in Figure 6.1a, in the case of a rigid enclosure, the incident sound wave reflects back without any loss in the amplitude. If the high voltage $U_{DC} + u_{AC}(t)$ is applied to the electrodes, the CD actuator forms a complex acoustic source consisting of monopole type heat source H centred around the high voltage electrode and dipole type force source \vec{F} located between

the electrodes (illustrated in red and blue in Figure 6.1b). The heat source, shown as the red symmetric waves propagating in opposite directions in Figure 6.1b, is generated due to the energy loss into heat in the ionisation region. The force source, shown as the asymmetric blue waves, is produced by the interaction of ions drifting from the high voltage electrode towards the grounded collector with neutral particles of air. By controlling the two sources, it is possible to adjust the acoustic impedance in front of the actuator to the desired one.

The linear approximation of the sound sources can be taken from the analytical model developed in Section 3.3 from Equations (3.14) and (3.19). These are important milestones that will be used in the next section to derive the control transfer function. The magnitude of AC force component and heat power density in the CD actuator with considered wire-to-mesh geometry can be expressed as follows:

$$\begin{aligned} F_\omega &= \frac{Cd}{\mu_i} (2U_{DC} - U_0) u_{AC}, \\ H_\omega &= C(3U_{DC}^2 - 2U_{DC}U_0) u_{AC}. \end{aligned} \tag{6.1}$$

where d is the interelectrode distance, μ_i is the effective ion mobility in the air, U_{DC} is the constant bias voltage, u_{AC} is the alternating voltage component responsible for sound, U_0 is the onset voltage (when discharge initiates), C is a dimensional constant. The last two parameters are estimated by measuring the voltage-current characteristics of the transducer and approximating it by Townsend's formula (Equation (2.1)), the other parameters are known. These two phenomena can be included as the sound sources in the wave equation (3.6). The goal of this study is to design a feedforward control architecture which uses a pressure signal from a microphone as the control input. The analytical model with the sound sources (Equation (6.1)) together with target acoustic impedance should be embedded in the control transfer function in order to calculate the needed actuator response.

6.3 Analytical derivation of control transfer function

The transfer function $\theta(\omega)$ converts the pressure signal acquired in front of the actuator into an AC component of the electrical voltage signal $u_{AC}(\omega)$ which is further summed with U_{DC} and applied to the electrodes. Before deriving θ , several assumptions should be made in order to simplify the problem without losing important information. In many sound absorption applications the CD actuator should be backed by some enclosure, for example, to be installed in a room corner, duct termination or wall-mounted. Therefore, we consider that the actuator is covered by a termination parallel to the electrodes plane with load impedance Z_L at a distance L from the actuator centre. If it is a rigid wall, Z_L can be considered as a high real-valued impedance. In the case when there is no termination (e.g. mounted in the cross-section of the ventilation duct), the load impedance is equal to characteristic medium impedance.

Furthermore, the problem can be considered as one dimensional due to several factors. First, the space between the set of electrodes and the enclosure presents a section of waveguide with termination impedance Z_L and constant cross-section. Second, the distribution of force \mathbf{F} and heat release H is homogeneous along the actuator hollow area. Thus, the sound sources can be treated as constant force and heat densities: $f = F_\omega / Sd$, $h = H_\omega / Sd$. Further, we are interested in solving the problem at a distance x_0 in front of the actuator, where the control microphone is placed. Since x_0 is much smaller than the actuator length ($x_0 = 10 \text{ mm} \ll \sqrt{S} = 50 \text{ mm}$), plane wave can be considered with negligible effect of spherical expansion. Finally, the thickness of the discharge volume $d = 6 \text{ mm}$ is much smaller than the wavelength at frequencies up to several kilohertz, so the CD actuator sound sources f and h can be considered as point sources. The simplified one-dimensional problem is summarised in Figure 6.2. Without any loss of generality, it can be assumed that the actuator is centred at the origin of the x -axis.

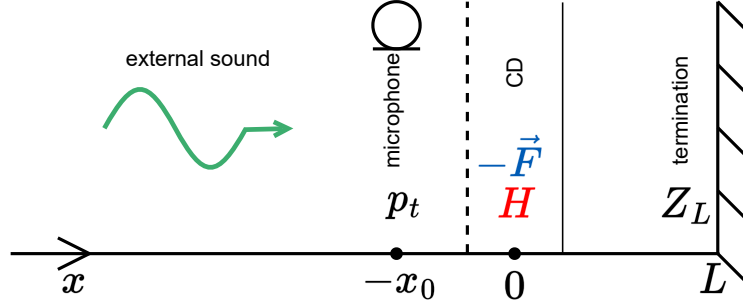


Figure 6.2: One dimensional schematics of acoustic sources and boundaries positions.

As the air in the corona discharge is weakly ionised, the energy mainly transfers through elastic interaction [76]. The wave equation can be derived from the system of linearised continuity, Newton's, and energy conservation equations with heat and force sources and the gas obeying adiabatic transformations [95]. The one-dimensional wave equations for acoustic pressure p and particle velocity v in the frequency domain can be derived similar to Equation (3.6) and are written as follows:

$$\begin{aligned} \left(\frac{\partial^2}{\partial x^2} + k^2 \right) p &= -\frac{j\omega}{C_P T_o} h + \frac{\partial f}{\partial x}, \\ \left(\frac{\partial^2}{\partial x^2} + k^2 \right) v &= -\frac{1}{\rho_o C_P T_o} \frac{\partial h}{\partial x} + \frac{j\omega}{\rho_o c^2} f, \end{aligned} \quad (6.2)$$

where k is the wave number, C_P is the heat capacity per unit mass, T_o is the static ambient air temperature, ρ_o is the static air density, c is the speed of sound in the air. The external acoustic excitation emanates from the left of the actuator (negative x values). Further, all acoustic pressures and velocities are considered for negative coordinates x as the only region of interest. Using the principle of superposition, acoustic pressures and velocities generated

only by either the heat source or the force source can be found independently in Equation (6.2). It reads:

$$\begin{aligned}
 p_f &= \frac{d}{2} \left(e^{jkx} - r e^{jk(x-2L)} \right) f, \\
 v_f &= -\frac{d}{2\rho_o c} \left(e^{jkx} - r e^{jk(x-2L)} \right) f, \\
 p_h &= \frac{dc}{2C_P T_o} \left(e^{jkx} + r e^{jk(x-2L)} \right) h, \\
 v_h &= -\frac{d}{2\rho_o C_P T_o} \left(e^{jkx} + r e^{jk(x-2L)} \right) h.
 \end{aligned} \tag{6.3}$$

In Equation (6.3), r is the reflection coefficient from the enclosure wall defined by $r = (Z_L - \rho c) / (Z_L + \rho c)$. p_f and v_f are the solutions of Equation (6.2) if $h = 0$, p_h and v_h are solutions of Equation (6.2) if $f = 0$. The acoustic pressure and velocity generated by the corona discharge actuator at position x is the sum of force and heat induced quantities. Thus, in the presence of external acoustic excitation (p_{ac} and v_{ac}), the total sound pressure and velocity at any position x in the duct can be written as:

$$\begin{aligned}
 p_t(x) &= p_f(x) + p_h(x) + p_{ac}(x), \\
 v_t(x) &= v_f(x) + v_h(x) + v_{ac}(x).
 \end{aligned} \tag{6.4}$$

The microphone at position $-x_o$ provides the measurement of $p_t(-x_o)$. The active control of the actuator should lead to achieving the target acoustic impedance Z_{tg} at $-x_o$. The goal is to assign the correct AC voltage component $u_{AC}(\omega) = \theta(\omega) p_t(-x_o, \omega)$ in order to adjust total velocity v_t so that $p_t(-x_o) / v_t(-x_o) = Z_{tg}$.

The particle velocity v_{ac} is linked to a specific acoustic impedance in the absence of the actuator: $v_{ac}(x) = p_{ac}(x) / Z_{ac}(x)$. In turn, Z_{ac} at the microphone position can be expressed in terms of known termination impedance Z_L , as the impedance at distance $x_o + L$ from a termination of a transmission line:

$$Z_{ac}(-x_o) = \rho c \frac{Z_L + j\rho c \tan(k(L + x_o))}{\rho c + jZ_L \tan(k(L + x_o))}. \tag{6.5}$$

Therefore, the total particle velocity v_t in Equation (6.4) rewrites through the known quantities:

$$v_t = v_f + v_h + \frac{p_t - p_f - p_h}{Z_{ac}}. \quad (6.6)$$

Now it is possible to derive the transfer function θ . Taking into account that $v_t(-x_o) = p_t(-x_o)/Z_{tg}$ and substituting all components from Equation (6.3) in Equation (6.6), one can obtain

$$\begin{aligned} \theta(\omega) &= \frac{u_{AC}}{p_t} = \frac{1}{A} \left(1 - \frac{Z_{ac}}{Z_{tg}} \right) / \left(1 + \frac{Z_{ac}}{\rho c} \right), \\ A &= \frac{d}{2} \left(f_o + \frac{ch_o}{C_P T_o} \right) e^{-jkx_o} + \frac{d}{2} \left(\frac{ch_o}{C_P T_o} - f_o \right) r e^{-jk(x_o+2L)} \\ f_o &= f/u_{AC} = \frac{C}{S\mu_i} (2U_{DC} - U_0), \quad h_o = h/u_{AC} = \frac{C}{Sd} (3U_{DC}^2 - 2U_{DC}U_0). \end{aligned} \quad (6.7)$$

In Equation (6.7) f_o and h_o are the constants depending on the actuator geometry and operating conditions. By changing the value of Z_{tg} , it is possible to target different acoustic conditions and obtain partial or full absorption under normal or grazing sound incidence. However, before implementation on a digital platform, the transfer function should be expressed in terms of the Laplace variable $s = j\omega$. One must ensure that $\theta(s)$ is a stable and proper transfer function.

Let us consider the derivation of the control transfer function $\theta(s)$ from analytical $\theta(\omega)$ with target impedance $Z_{tg} = n\rho c$ ($n \in \mathbb{R}$) which will be further implemented for experimental validation. In the low frequency range (up to ~ 2 kHz) the distance between the actuator and the microphone can be neglected setting $x_o = 0$ (in the experiment microphone is located 10 mm in ahead of the grounded electrode). If target impedance is set as $Z_{tg} = n\rho c$, the transfer function from Equation (6.7) with Z_{ac} from (6.5) can be written in the form:

$$\begin{aligned} \theta(s) &= \frac{\theta_1}{\theta_2}, \\ \theta_1 &= \frac{\left(Z_L - \frac{\rho c}{n} \right) \left(\frac{n\rho c - Z_L}{nZ_L - \rho c} + j \tan(kL) \right)}{(Z_L + \rho c)(1 + j \tan(kL))} \\ \theta_2 &= \frac{d}{2} \left(f_o + \frac{ch_o}{C_P T_o} + \left(\frac{ch_o}{C_P T_o} - f_o \right) r e^{-2jkL} \right). \end{aligned} \quad (6.8)$$

A way to convert this transfer function to the s domain is to use the Taylor expansion for tangential and exponential functions. High order expansion should preserve the function behaviour at higher frequencies but can lead to unstable poles and coefficients with too

high or too low values that are difficult to implement digitally. Thus, a first order expansion was used for the tangent function and second order for exponential, rewritten in the form $\exp(-2jkL) = \exp(-jkL)/\exp(jkL)$. Therefore, the transfer function takes the following form in the s domain:

$$\theta_1 = \frac{(Z_L - \frac{\rho c}{n}) \left(\frac{n\rho c - Z_L}{nZ_L - \rho c} + \frac{Ls}{c} \right)}{(Z_L + \rho c) \left(1 + \frac{Ls}{c} \right)} \quad (6.9)$$

$$\theta_2 = \frac{d}{2} \left(f_o + \frac{ch_o}{C_P T_o} + \left(\frac{ch_o}{C_P T_o} - f_o \right) r \frac{1 - \frac{Ls}{c} + \frac{L^2 s^2}{2c^2}}{1 + \frac{Ls}{c} + \frac{L^2 s^2}{2c^2}} \right)$$

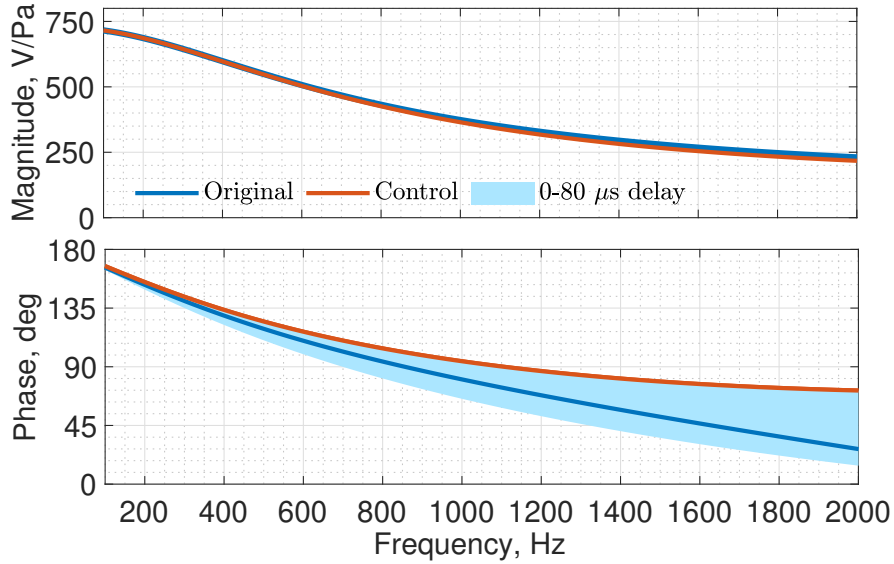


Figure 6.3: Bode plots of transfer functions $\theta(\omega)$ from (6.7) and $\theta(s)$ from (6.9) with target impedance $Z_{tg} = \rho c$. The light blue filled area shows the change in phase of $\theta(s)$ if time delay in control is introduced.

Figure 6.3 illustrates the magnitude and phase of the transfer functions. The parameters needed to plot the functions are collected in Table 6.1. The procedure of their estimation is detailed in the experimental section. The blue curve relates to the original analytical function $\theta(\omega)$ calculated from Equation (6.7) with target impedance $Z_{tg} = \rho c$. The control transfer function $\theta(s)$ from Equation (6.9) to be used in the experiment is depicted in red. All the approximations taken to derive Equation (6.9) from Equation (6.7) do not affect the magnitude considerably (for $Z_{tg} = \rho c$) but change the phase in the frequency range of interest. As can be seen, the control transfer function has a noticeable phase lead over the original one that builds up to approximately 45 degrees at 2000 Hz. Such dynamics is advantageous as it can be partially corrected by inducing a simple time delay in the controller. The light blue

area shows where the phase of the control transfer function can fall if the delay between 0 and 80 microseconds is added. Note that the difference in phase and amplitude between $\theta(\omega)$ and $\theta(s)$ can be different if another target impedance is set. The same functions are shown in a wider frequency range in Appendix B in Figure B.8. The figure demonstrates, that the low order approximation of the analytical function is accurate only at low frequencies. In the next section, numerical analysis is conducted in order to evaluate the performance of the plasma-based system and find the optimal delay value that maximises sound absorption in the 100-2000 Hz frequency range.

6.4 Modelling absorption performance

The CD-based absorber can be modelled in a finite element method software (Comsol Multi-physics). Although the complete electroacoustic numerical model of the corona discharge was proposed in Chapter 3, it would not be advantageous to use it in order to simulate the active control. First, a transient simulation requires a long time to compute in the wide frequency range with a fine step. Second, we are interested in the linear part of the CD response in a waveguide. Therefore, a two-dimensional simulation is carried out directly in the frequency domain, where the sound sources are taken from the analytical model. Since the source estimation was found to be accurate in Chapter 4, such a hybrid approach is a reasonable compromise for the efficiency of the simulation in the low frequency range (up to 2000 Hz), when there is no need to capture the nonlinear dynamics.

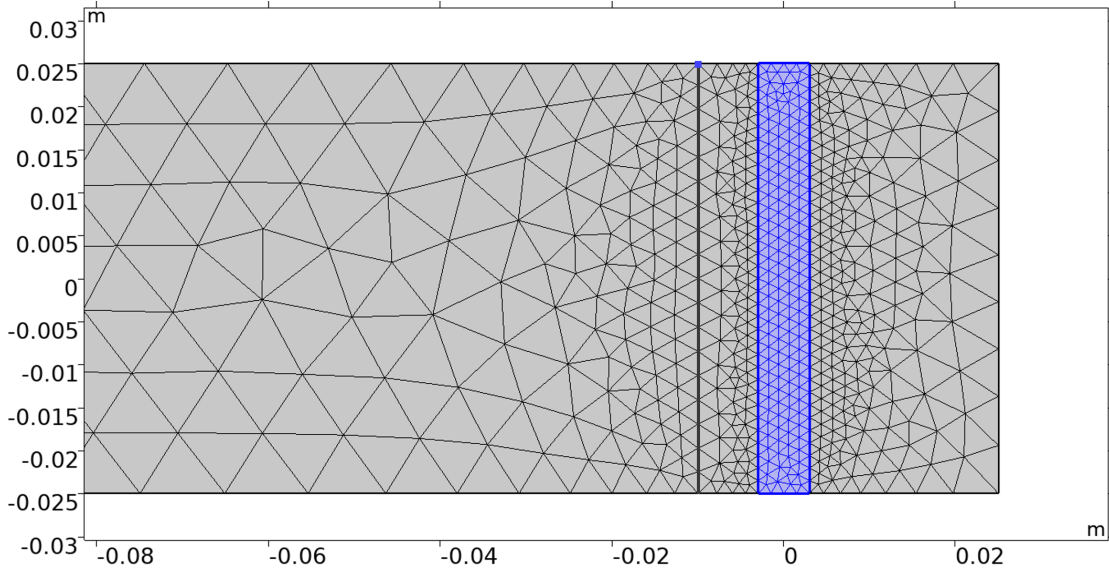


Figure 6.4: Geometry of the two dimensional waveguide terminated with the enclosed corona discharge actuator. The triangular mesh is denser towards the rectangular zone which imitates the discharge (highlighted in violet). The microphone position is a blue dot with coordinates (-0.01, 0.025).

The geometry of the numerical model is illustrated in Figure 6.4. The simulation is carried out in a duct with a height of 5 cm. The CD actuator is represented by an air volume of height 5 cm (\sqrt{S}) and thickness $d = 6$ mm. This volume acts as a source of uniform force and heat power with densities f and h , as expressed in Equation (6.7). The electrodes are not included in the simulation since they present negligible acoustic resistance and thus are transparent to sound waves. The actuator is terminated by the boundary with impedance $Z_L = 6.7 \cdot 10^3 \text{ Pa} \cdot \text{s} \cdot \text{m}^{-1} \approx 16\rho c$ at a distance of 25 mm from the actuator centre. It reflects the mean value of the real part of the termination impedance which was measured in the impedance tube with the actual prototype. Since the termination for the experimental prototype is manufactured with a 3D printer out of PLA plastic, a more realistic value for Z_L should be considered instead of the hard wall. As will be seen in Figure 6.11 from passive measurements, constant real impedance Z_L is a good approximation of the termination. The microphone is placed in front of the CD actuator flush-mounted in the tube (blue dot in Figure 6.4). Its centre is located 10 mm ahead of the actuator centre. To estimate the strengths of the force and heat sources, the voltage-current characteristics of the actual prototype should be measured and fitted with the Townsend formula. The procedure was described in Section 4.3. The fit result is illustrated in Figure B.9. Table 6.1 lists all the parameters needed for the numerical model.

Table 6.1: CD actuator model parameters for a definition of a control transfer function.

Parameter	Symbol	Value	Unit
Air mass density	ρ_o	1.23	kg m^{-3}
Sound speed in air	c	343	m s^{-1}
Ambient temperature	T_o	293	K
Heat capacity	C_P	1015	$\text{J kg}^{-1} \text{K}^{-1}$
Interelectrode gap	d	$6 \cdot 10^{-3}$	m
Discharge area	S	$25 \cdot 10^{-4}$	m^2
Microphone distance	x_o	$1 \cdot 10^{-2}$	m
Enclosure length	L	$25 \cdot 10^{-3}$	m
Load impedance	Z_L	$6.7 \cdot 10^3$	Pa s m^{-1}
Positive ion mobility	μ_i	$1.1 \cdot 10^{-4}$	$\text{m}^2 \text{V}^{-1} \text{s}^{-1}$
Voltage offset	U_{DC}	8.0	kV
Onset voltage	U_0	6.19	kV
Fitting constant	C	$2.31 \cdot 10^{-4}$	A V^{-2}

The achieved acoustic impedance Z_{ach} of the system is evaluated along the line at the same distance as the microphone (black line at $x = -0.01$ m). The reflection coefficient of the system R and sound absorption coefficient α can be calculated as:

$$R = \frac{Z_{\text{ach}} - \rho c}{Z_{\text{ach}} + \rho c}, \quad (6.10)$$

$$\alpha = 1 - \text{abs}(R^2).$$

If the system is passive, the reflection coefficient R has the same magnitude as r from Equation (6.3) and equals $(Z_L - \rho c)/(Z_L + \rho c)$. The sound absorption is only provided by the enclosure wall. In the active case, the numerical model simulates the dynamics of the CD actuator that senses the pressure in front and outputs the voltage signal according to the defined transfer function. Figure 6.5 shows the calculated achieved impedance and sound absorption in the passive case, in the active case with ideal analytical transfer function θ from Equation (6.7), as well as its simplified version from Equation (6.8). Both active cases aim at full sound absorption with $Z_{tg} = \rho c$.

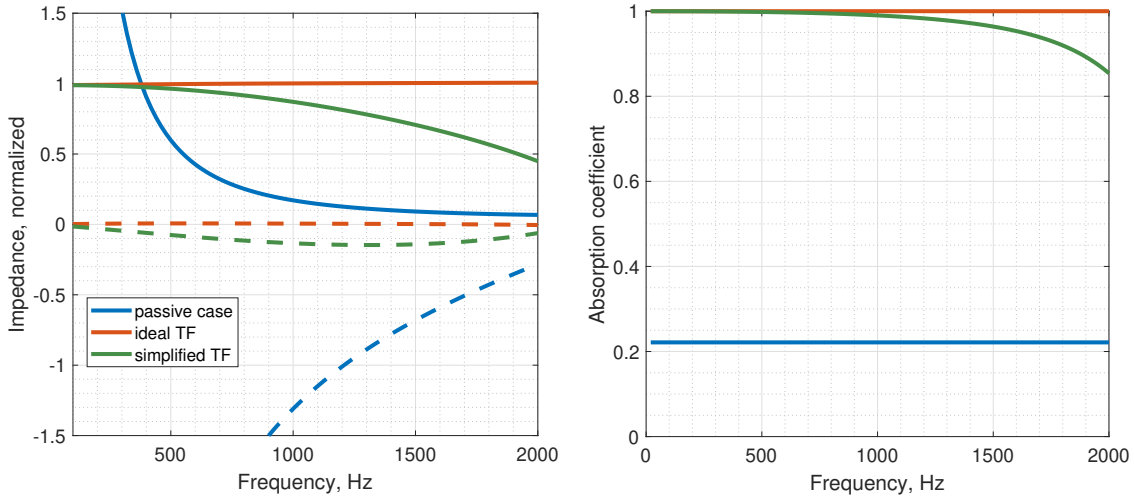


Figure 6.5: Simulated achieved normalised impedance and sound absorption coefficient of the CD actuator in 3 cases: control off (blue); ideal control transfer function according to Equation (6.7) (orange); simplified control transfer function as in Equation (6.8). Solid lines on the impedance graph represent the real part of achieved impedance, dashed lines - imaginary part. $Z_{tg} = \rho c$.

During the derivations in the previous section, we made an assumption that the sound sources and, consequently, the CD actuator is infinitely thin. Although this is not the case in the numerical simulation, the control with the ideal transfer function from Equation (6.7) still leads to precisely achieved impedance and perfect absorption in the considered frequency range (orange curves in Figure 6.5). This result confirms that the thickness of the actuator can be neglected. However, the achieved sound absorption falls to 86%, if the CD actuator is controlled through the simplified θ from Equation (6.8) (green lines). The achieved resistance deviates from the target starting from 500 Hz and decreases to $0.43\rho c$ at 2 kHz. The control transfer function (6.8) differs from Equation (6.7) only because of neglecting the distance between the microphone and the actuator centre (10 mm, which means only 4 mm between the collector plate and the body of 1/4" microphone). Thus, ignoring it can lead to a noticeable degradation in the absorption performance during the experimental tests. This simulation assumes that the hardware has no delay between the pressure acquisition and voltage output. However, this is not the case in real situations. Moreover, as we observed in Figure 6.3, the

transfer function from Equation (6.9), which is to be implemented in the experiment, has a very similar magnitude to the original θ from Equation (6.7) but provides a phase lead in the considered frequency range. Therefore, a particular delay in the control loop can potentially tailor the system to have a response closer to the original transfer function. In this way, we further investigate if having a delay in the control system can help close the gap in performance.

6.4.1 Influence of control delay on performance

The operation of the CD-based active absorber, which is controlled via $\theta(s)$ from Equation (6.9), is simulated numerically with the time delays in the range of 0-80 μs . The delay is simply implemented as a multiplying factor $\exp(-j\omega\tau)$ to the transfer function. Figure 6.6 illustrates the expected performance in terms of achieved sound absorption coefficient and the corresponding acoustic impedance.

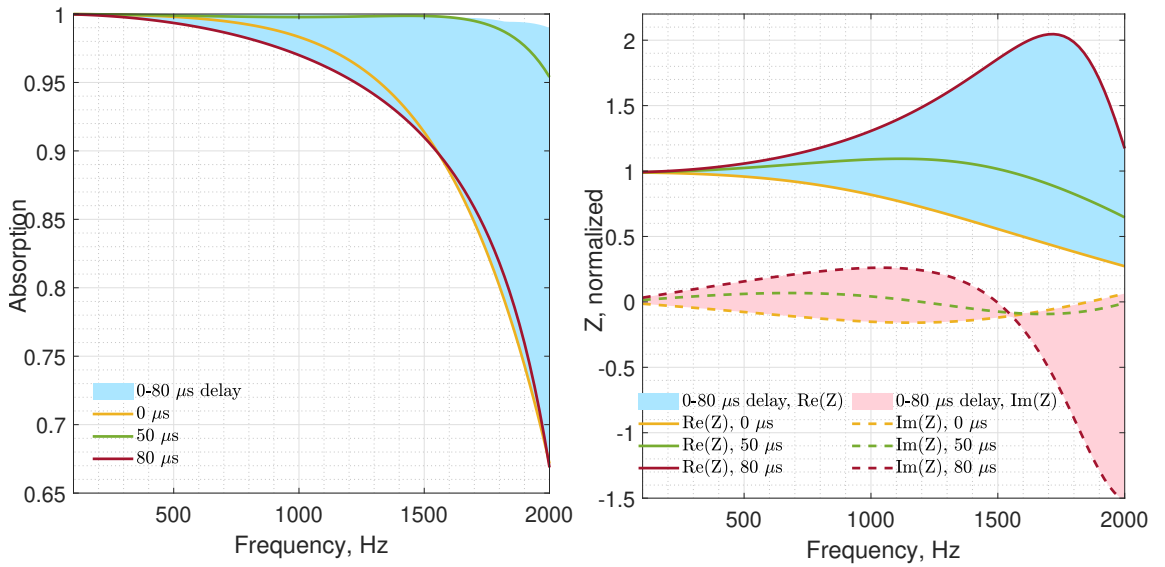


Figure 6.6: Simulated performance if the active system is controlled with transfer function from Equation (6.9) with the time delay 0-80 μs . Left: achieved sound absorption coefficient; right: achieved normalised acoustic impedance. Solid line - real part of impedance, dashed line - imaginary part of impedance.

Note that the absorption coefficient in Figure 6.6 is shown in the range 65-100%. If we assume that the system has no delay (pure response of the transfer function of Equation (6.9)), the sound absorption remains close to perfect from 100 to 1000 Hz (yellow line in Figure 6.6 on the left). Such bandwidth is already competitive with loudspeaker-based state-of-the-art absorbers [45]. However, at higher frequencies, the performance degrades, and absorption reaches only 67% at 2000 Hz. The corresponding achieved resistance drops down to $0.25\rho c$

(solid yellow line on the right). Such deviation is caused by the phase mismatch of the control transfer function compared to the analytical model because the tangent and exponential functions are expanded only to the first and second order. Since the introduction of delay into the control system shifts the phase closer to the original transfer function of Equation (6.7), this should increase the absorption efficiency in the high frequency range. The blue and pink shaded areas show the range where the achieved absorption and impedance can fall with the additional 0-80 μs delay. One can observe that the control case with 80 μs delay results in a similar absorption function, although it is achieved with a significantly different impedance.

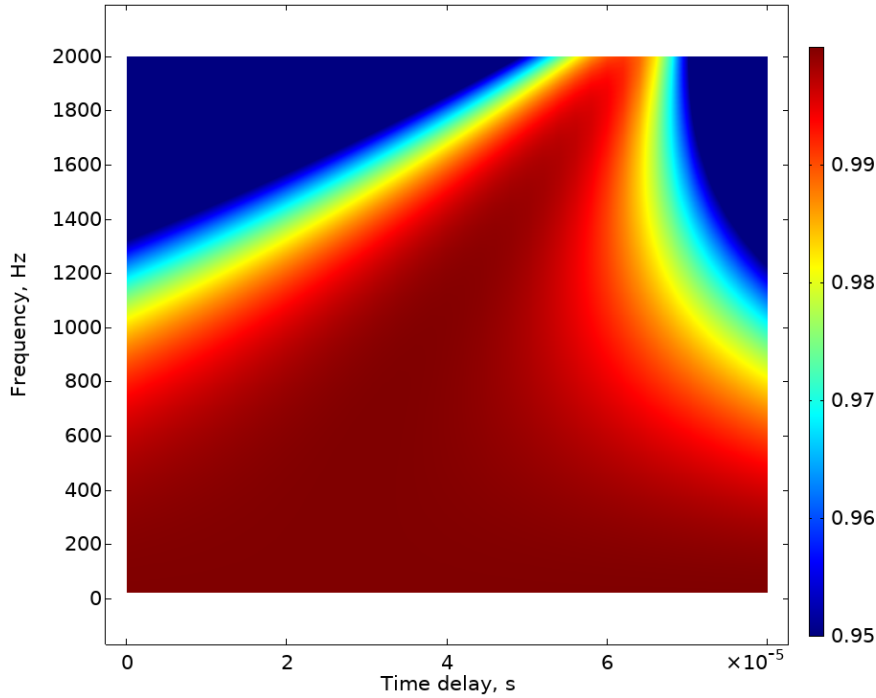


Figure 6.7: Absorption coefficient map as a function of frequency and the introduced delay. The active system is controlled with transfer function from Equation (6.9). Note, that the minimal value in legend is set to 0.95, but blue colored zones contain data with lower absorption coefficient (down to 0.66).

The parametric study on the optimal delay value was conducted in order to determine the one that maximises the sound absorption in the frequency range 100-2000 Hz. Figure 6.7 depicts the achieved absorption coefficient as a function of frequency and control delay. We can see that a constant time delay cannot bring the absorption to 100% in the whole frequency range. If all the frequencies are equally weighted, it appears that $\tau \approx 50\mu\text{s}$ provides the best result in the considered range. The corresponding achieved absorption and acoustic impedance are shown in green in Figure 6.6. Compared to the control case with no delay, the achieved resistance remains close to ρc in the broader frequency range, falling only to $0.6\rho c$ at 2000 Hz, while the reactance is not significantly affected and stays around 0. As can be seen from Figure 6.7, with a greater delay, it is possible to boost absorption further above 1800 Hz, but at

the cost of efficiency at lower frequencies.

Finally, the numerical study reveals the broadband absorbing potential of the CD-based active system that operates with a predefined control transfer function. The simulation helped in identifying what control delays can be tolerated by the system and can even improve the performance. It must be noted here that the analysis carried out above is valid for a considered target impedance $Z_{tg} = \rho c$. If the target changes, the phase mismatch between the original transfer function of Equation (6.7) and the one to be implemented in the hardware can be different. Therefore, the optimal time delay can vary. In the next section, we estimate the delay of the whole control system in order to see what can be achieved in the experiment.

6.5 Experimental setup and implementation

6.5.1 Experimental setup

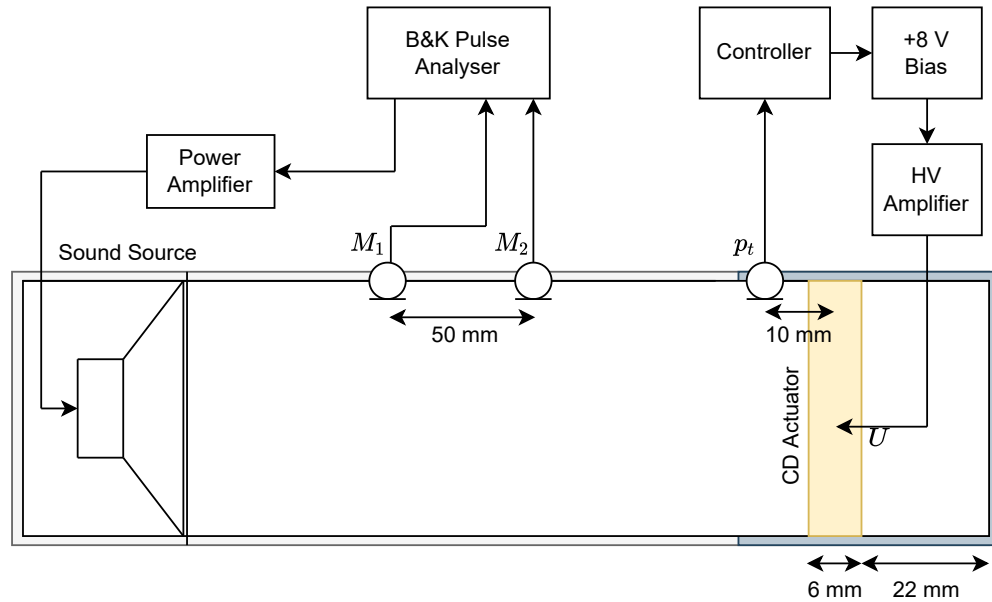


Figure 6.8: Schematics of experimental setup, including the impedance tube, block scheme of active control and signal acquisition.

To experimentally evaluate the absorption performance of the CD-based active system, the measurements under normal sound incidence are carried out in the impedance tube as shown in Figure 6.8. The tube and the measurement system are similar to what was described in Section 5.2.3. The active system is positioned at the right termination. The actuator used in the experiments is the same as was introduced in Section 4.1 with an active area of $50 \times 50 \text{ mm}^2$ and an interelectrode distance of 6 mm. The actuator is backed by a rectangular enclosure with a $50 \times 50 \text{ mm}^2$ cross-section and depth such that the enclosure wall is located 25 mm from the actuator centre. The hardware used to control the CD actuator is depicted at the right in

6.8. PCB130D20 ICP 1/4" microphone senses the total sound pressure in front of the actuator at a 10 mm distance from its centre. The control transfer function $\theta(s)$ from Equation (6.9) with $Z_{tg} = \rho c$ is discretised and implemented on a real-time platform Speedgoat IO-334 which runs at 50 kHz frequency. As previously, it calculates u_{AC} component reduced by a factor of 1000 for the output, which is further summed with a constant voltage and amplified. Geometrical and discharge parameters needed for the definition of the control transfer function are the same as in the numerical model and listed in Table 6.1.

6.5.2 Time delay of control system

The control system consists of two main parts: the controller and the high voltage amplifier. Both of them introduce some latency to the control loop. The estimation of the total delay is essential to be able to relate the obtained experimental data and the numerical prediction. Thus, the time delay brought to the loop by the controller and high voltage amplifier is estimated by measuring the frequency response. The response is recorded with Brüel&Kjaer Pulse multichannel analyser.

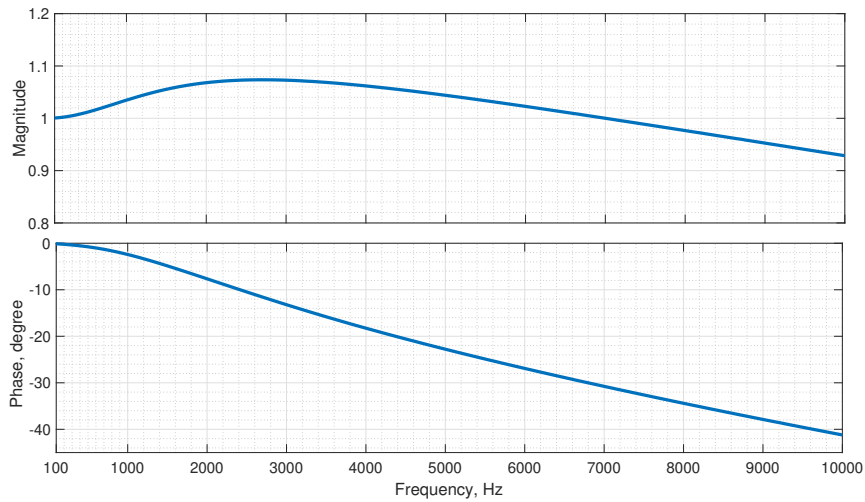


Figure 6.9: Frequency response of the high voltage amplifier TREK 615-10 loaded with the CD actuator introduced in Section 4.1. The signal is recorded from the embedded voltage probe, so the voltage magnitude is reduced by a factor of 1000.

Figure 6.9 shows the frequency response of the high voltage amplifier in the frequency range up to 10000 Hz. Since it may depend on the load, the CD actuator is connected during the measurement. The magnitude is reduced by a factor of 1000. We can see that, in the frequency range of interest (up to 2 kHz), the gain deviates from unity by 7% maximum. The phase response presents a linear roll-off starting from 1000 Hz. It corresponds to a constant time

delay of the signal with a value of approximately $14 \mu\text{s}$. However, the slope is different below 1000 Hz. The absorption coefficient map in Figure 6.7 indicates that below this frequency, the value of the time delay should not noticeably impact the sound absorption quality, as it varies from 0.98 to 1 in the 0-80 μs delay range. Therefore, to take care of the high frequency performance, we can estimate the latency of the amplifier as $14 \mu\text{s}$.

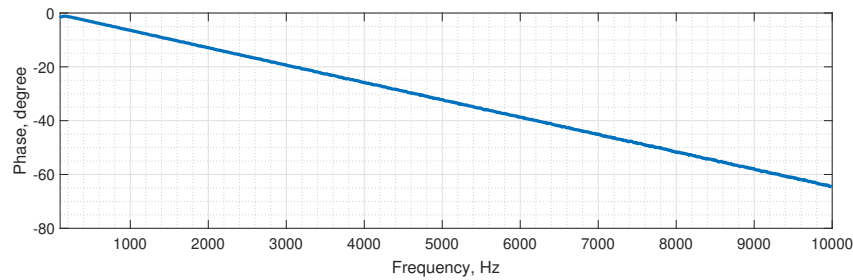


Figure 6.10: Phase difference between the measured response of the controller, which runs the discretised version of the transfer function (6.9) with a sampling frequency of 50 kHz, and the transfer function (6.9).

The latency of the controller is also estimated. First, the frequency response of the controller is recorded when it runs the discretised transfer function from Equation (6.9) at the sampling frequency of 50 kHz. Then, we compare the recorded data with the same $\theta(s)$. The difference in phase is shown in Figure 6.10. It reasonably demonstrates a linear change in phase over the whole frequency range of interest. The time delay of $18 \mu\text{s}$ is calculated from the slope of the line. This value includes the latency of ADC, processing, and DAC and appeared to be slightly smaller than the $20 \mu\text{s}$ period of acquisition.

Finally, the cumulative time delay of the control system for the CD actuator equals approximately $32 \mu\text{s}$. It corresponds to a nominal delay that can be achieved with the given hardware and control settings. The delay is slightly shorter for frequencies below 1000 Hz due to the response of the high voltage amplifier. Since the controller runs at 50 kHz, the system delay can be increased with $20 \mu\text{s}$ step if the output is held by one sampling period. With one period hold, the total system delay can be advantageously used as it closely matches the optimal value for broadband sound absorption.

6.6 Broadband sound absorption

Figure 6.11 presents the achieved acoustic impedance and the sound absorption coefficient for the CD-based system in a passive case and two active cases with different time delays in the controller. The corresponding numerical results are superimposed over the experimental data. When the control is off, the dynamics is governed only by the termination impedance and leads to a negligibly small sound absorption constant over the considered frequency range. It can be seen that approximation of the termination impedance by a constant real

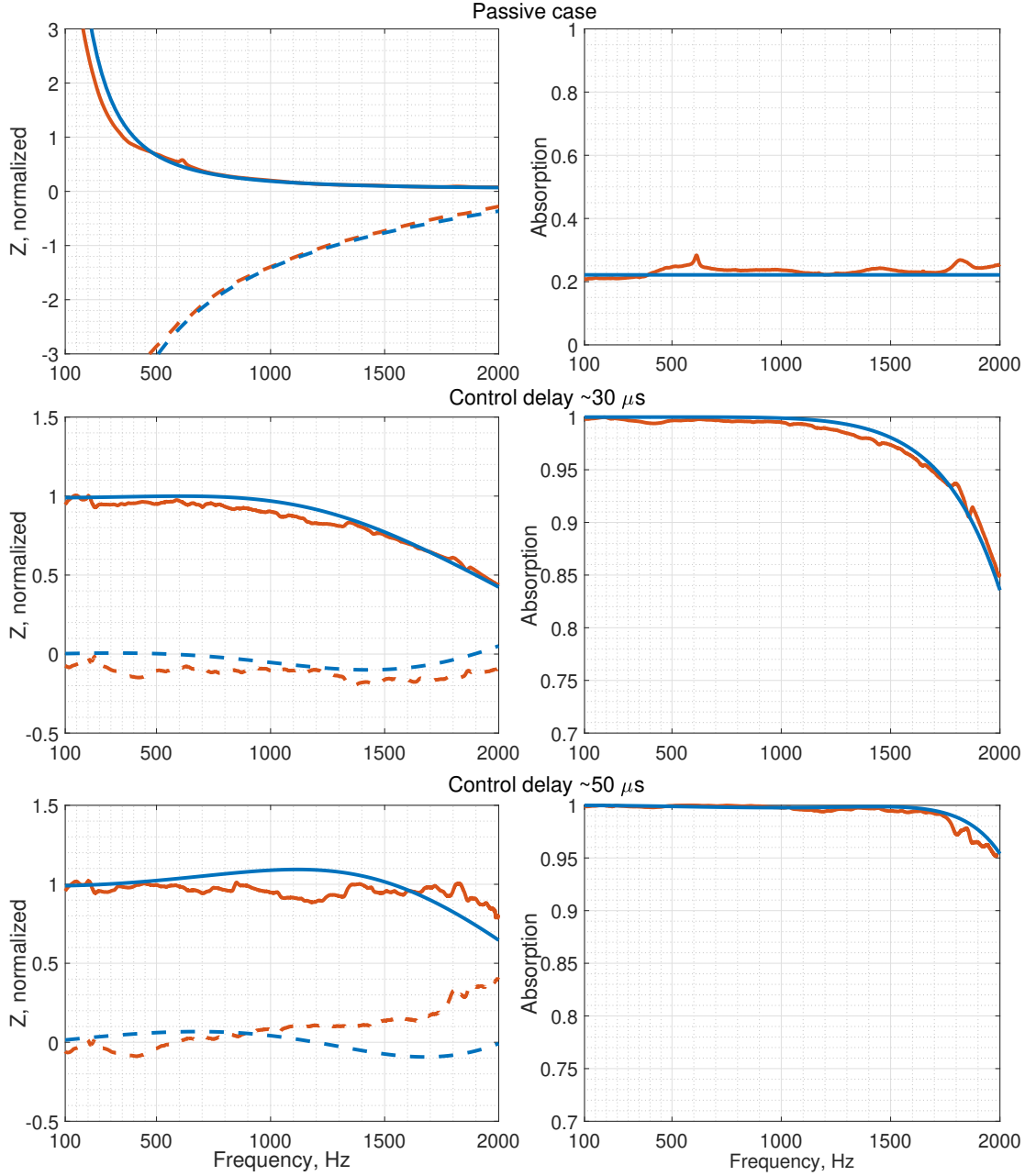


Figure 6.11: Experimentally achieved performance of the CD-based active sound absorber in the duct with $Z_{tg} = \rho c$ and comparison with a numerical model. Top row - passive operation of the absorber; middle row - active operation with control time delay $\approx 30 \mu s$; bottom row - active operation with control time delay $\approx 50 \mu s$. Blue lines - numerical simulation, red lines - measurements. Transfer function (6.9) is implemented. On impedance graphs: solid line - real part of impedance, dashed line - imaginary part of impedance.

value Z_L in the model provides a reasonable agreement with the experimental data. It is important to have a good match in Z_L , as it is included in the control transfer function and

influences the magnitude of the voltage applied to the CD. Two other cases target perfect sound absorption but with different delays in the control loop. It should be noted that the absorption values depicted on the axis in the active case start from 0.7 for better visualisation of the details. The first active measurement corresponds to the case when no additional time delay was added to the control transfer function. The value of $32 \mu s$ is estimated in the previous section as the cumulative hardware delay between the signal entering the controller and the output of the high voltage amplifier. As expected, we obtained almost purely real impedance close to ρc at lower frequencies, but its magnitude reduces towards 2000 Hz. The absorption coefficient remains equal to 1 up to 1000 Hz but gradually decreases to 0.85 by 2000 Hz. This measurement appears to be in good agreement with the results of numerical simulations.

As observed in the previous section, high frequency absorption can be further improved by including additional time delay in the controller. In this sense, the second active case corresponds to the control setting with a delay of one sampling period. It brings the total system delay to $\approx 52 \mu s$, which is close to the optimal value estimated in numerical simulations. As a result, the sound absorption is considerably improved above 1 kHz, extending the bandwidth of perfect absorption. The value falls to only 95% at 2000 Hz. Although the experimentally achieved impedance differs from the modelled one in the high frequency range, the trend of lifting the resistance higher to ρc is still preserved. Adding $20 \mu s$ more to the total delay was already not beneficial for the absorbing performance of the active system and is not reported.

We have witnessed again that the corona discharge actuator can provide a genuinely broadband sound absorption under normal incidence by imposing the target impedance equal to characteristic air impedance. The bandwidth could be extended further below 100 Hz because the transfer function has an asymptotically constant magnitude towards low frequencies. However, the 1/4" control microphones used in the experiment do not have a zero phase response at low frequencies, which diminishes the efficiency. Another aspect is the sound pressure level. The sound pressure did not exceed 1 Pa in the measurements. Now, with the analytical transfer function, it can be understood that the present prototype should output voltage $u_{AC} = 750 \text{ V/Pa}$ to be able to target total absorption at low frequencies (see Figure 6.3). Therefore, high sound pressure levels cannot be absorbed in the present configuration (u_{AC} should be much lower than U_{DC}). This limitation will be discussed in the conclusions. Nevertheless, to the author's knowledge, the CD actuator outperforms in bandwidth all real-time impedance control systems based on conventional transducers.

6.7 Targeting different resistances

The optimal target impedance for sound absorption depends on the application. For example, efficient low frequency sound absorption in a room of medium size requires the resistive impedance with the values equal to fractions of ρc [16, 137]. Alternatively, damping the noise in ducts in a wall-mounted configuration may demand the resistance to be higher than ρc [91].

Therefore, here we target resistive impedances, which are different from the characteristic impedance of the air.

The measurements of acoustic impedance were performed for the targets $Z_{tg} = 0.5\rho c$ and $Z_{tg} = 2\rho c$. Figure 6.12 (left) represents the Bode plots of analytical transfer functions from Equation (6.7) with corresponding targets (original) compared with the control transfer functions $\theta(s)$ from Equation (6.9) without time delay. As can be seen, the change in target resistance significantly impacts the low frequency magnitude of θ . To achieve lower impedance, higher voltage amplitude should be generated by the actuator. It can be understood as the active system should create a stronger control action in order to change its passive impedance at the actuator position, which in the low frequency limit converges to Z_L (see Equation (6.5)). Thus, the tests were carried out at a low sound pressure level so that the voltage swing on the CD actuator does not exceed 10% of U_{DC} . In contrast to the case with $Z_{tg} = \rho c$ (Figure 6.3), a significant magnitude mismatch can be observed in the high frequency range between the original analytical and control functions for $Z_{tg} = 2\rho c$ (19% compared to 6%). The presence of time delay in the controller can improve the phase dynamics (though the optimal delay values are different for different targets), but the magnitude mismatch will still impact the achieved impedance in the high frequency range.

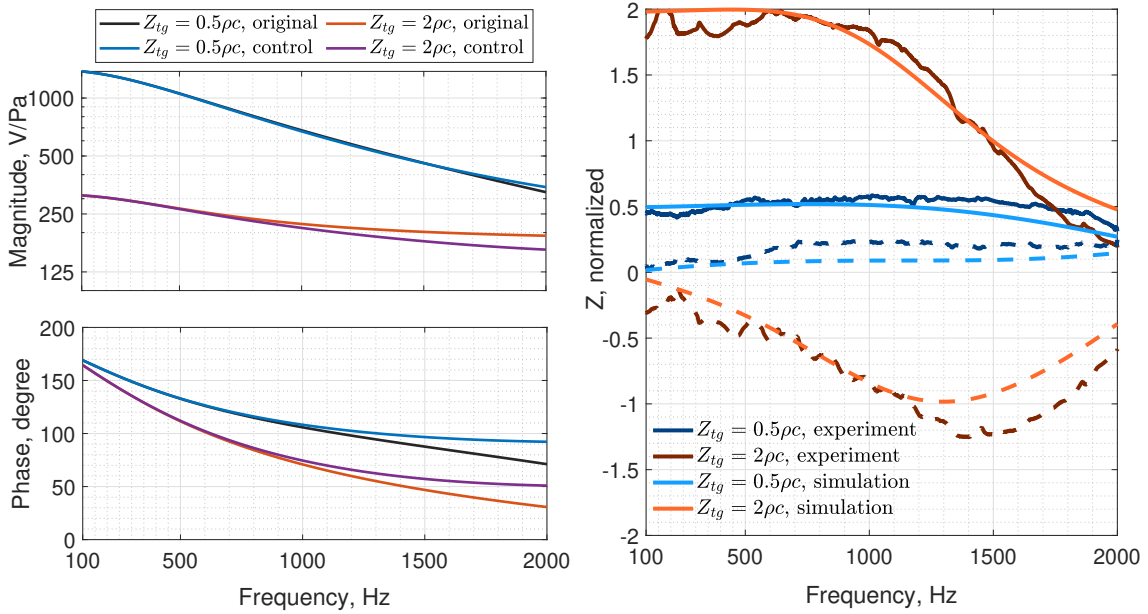


Figure 6.12: Left: bode plots of transfer functions $\theta(\omega)$ (6.7) and $\theta(s)$ (6.9) with $Z_{tg} = 0.5\rho c$ and $Z_{tg} = 2\rho c$ without time delay. Right: achieved acoustic impedances for the corresponding control cases with $Z_{tg} = 0.5\rho c$ and $Z_{tg} = 2\rho c$, $30 \mu s$ delay is set in the simulation. On the impedance graph: solid line - real part of impedance, dashed line - imaginary part of impedance.

The right panel of Figure 6.12 shows the achieved acoustic impedances for the control cases

with $Z_{tg} = 0.5\rho c$ and $Z_{tg} = 2\rho c$. The measurements are compared to the numerical simulation, which includes the time delay of $30 \mu s$ (nominal time delay of the control system). The experimental data is satisfactorily consistent with the numerical simulations. The resulting impedance resembles the target only in the low frequency range for the case with $Z_{tg} = 2\rho c$. The magnitude and slight phase mismatch, as discussed above, could impact the performance. Target impedance $Z_{tg} = 0.5\rho c$ is achieved with higher accuracy, although the imaginary part of impedance deviates from zero.

The active system was tested with higher targets than $2\rho c$. The gradual decrease of performance towards lower frequencies was observed if the simplified formulation of transfer function $\theta(s)$ from Equation (6.9) is implemented on the controller. On the other side, the resistances, which are considerably lower than $0.5\rho c$, were not achieved. This requires too high AC voltage output from the corona discharge actuator or the operation at reduced magnitudes of the acoustic signal. To improve the high frequency behaviour, the control transfer function could be estimated from the analytical Equation (6.7) differently, for example, by direct fitting with a finite order rational function. One of these examples is shown in the next section.

6.8 Acoustic mirror with various levels of reflection under normal incidence

We observed in the previous section that the passive behaviour of the CD transducer is close to the hard wall. The reflection is defined by the rigidity of the enclosure. With active control, it can be turned into a perfect broadband absorber. Alternatively, any transitional configuration that absorbs incident acoustic energy only partially can be imagined.

6.8.1 Target impedance to control magnitude and phase of reflection

The amount of absorbed and reflected energy can be controlled by implementing various target impedances in the control law. For example, increasing target resistance from ρc towards Z_L should change the absorption coefficient from 1 to 0. However, any complex frequency-dependent impedance can be implemented that keeps the transfer function stable. Moreover, phase of the reflected signal can be also potentially controlled. Here, we implement a different target which can lead to partial constant magnitude of reflection and variable phase. We employ passive acoustic impedance from Equation (6.5) and modify it in the following way:

$$Z_{tg} = Z_c \frac{\beta Z_L + j Z_c \tan(k(L + x_o + \Delta L))}{Z_c + j \beta Z_L \tan(k(L + x_o + \Delta L))}, \quad (6.11)$$

where β is a dimensionless scaling factor of the termination impedance Z_L , and the parameter

ΔL acts as an additional virtual depth of the rear termination. If $\beta = 1$ and $\Delta L = 0$, the target impedance equals the passive Z_{ac} and no active control is required. However, as β changes, the target imitates the presence of the termination behind the CD actuator with the impedance equal to βZ_L . Lowering the value of β leads to the softening of the virtual termination, thus, to higher sound absorption. When $\beta = Z_c / Z_L$, target equals again to characteristic air impedance yielding full absorption. This configuration resembles an acoustic mirror with an adjustable reflection coefficient. When the parameter ΔL differs from zero, the sound wave reflects with a delay that corresponds to an additional propagation distance of length $2\Delta L$. Therefore, along with varying the magnitude of sound reflection, it is possible to change the phase mimicking longer termination behind the CD.

6.8.2 Experimental results

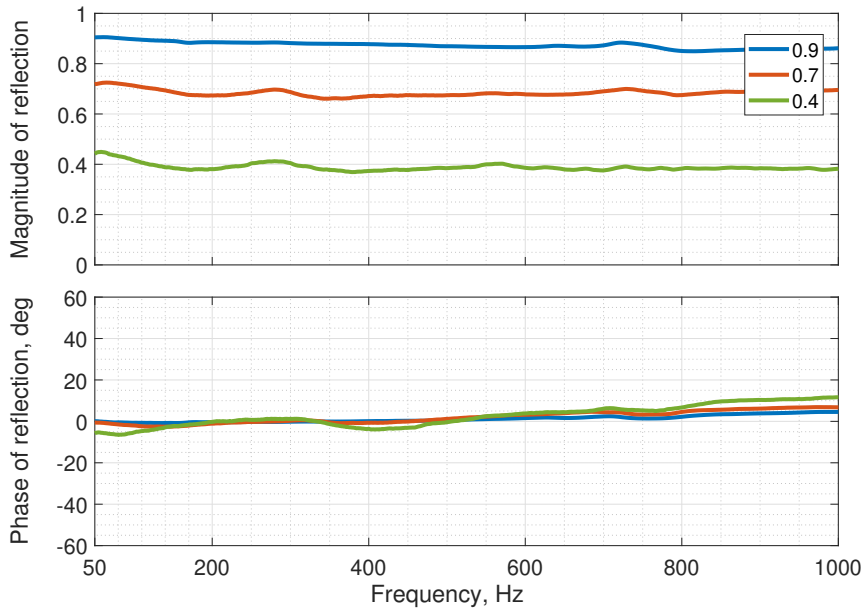


Figure 6.13: Demonstration of a tunable various levels of sound reflection with the CD actuator. By varying the target impedance after Equation (6.11), reflection coefficient of 40, 70, 90 percent is achieved.

This time, the control transfer function was obtained in a different way. The analytical function $\theta(\omega)$ was fitted by a third order rational function using Pade approximation. The obtained function has stable poles. It was discretised with the sampling frequency of 50 kHz and implemented in a controller.

Figure 6.13 shows that the CD-based active device can operate as a tunable mirror with adjustable sound reflection coefficient working over a wide frequency range by varying parameter β and keeping $\Delta L = 0$. The coefficient β was chosen in order to obtain 40, 70, 90 % reflection in magnitude. A different type of microphone was used for control and measurements (PCB

378B02), which allowed extending the control to the low frequency range.

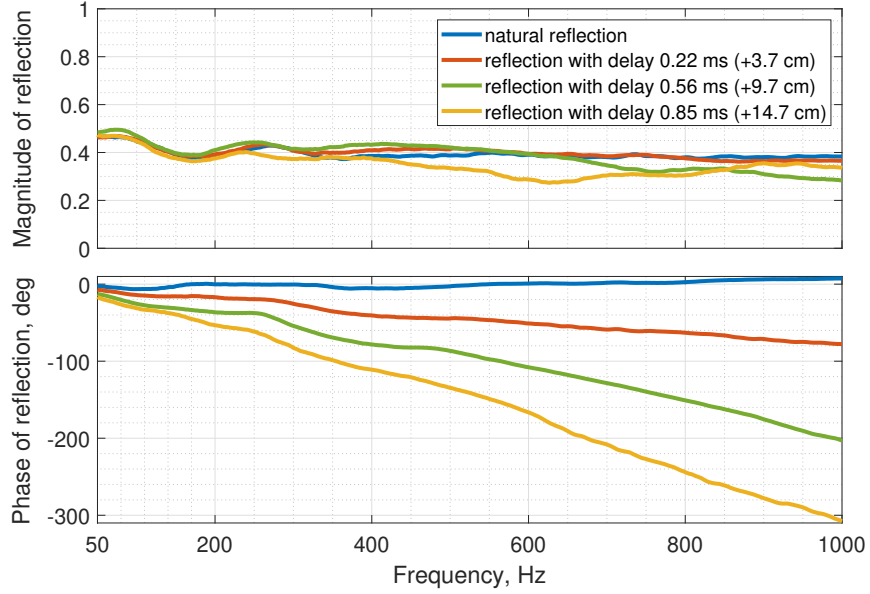


Figure 6.14: At a fixed reflection level, the linear roll-off of the reflection phase is controlled, artificially introducing a constant reflection time delay. Delays of 0.22, 0.56, 0.85 ms correspond to virtual elongations of the device by 3.7, 9.7, 14.7 cm, respectively.

Figure 6.14 illustrates the case, where the reflection magnitude remains the same but the phase changes linearly with different slopes. This is achieved by changing ΔL and constant value of β in Equation (6.11). The magnitude of reflection is fixed at 40 %, and ΔL equals to 3.7, 9.7, 14.7 centimeters, which corresponds to reflection delays of 0.22, 0.56, 0.85 ms (initial targets were 5, 10, 15 cm, but exact values are not achieved due to final order transfer function approximation and control delays). These values are consistent with the measured slopes of the linear reflection phases.

6.9 Conclusions

This chapter completes the study of the corona discharge actuator as the electroacoustic transducer for active control. It presents a novel control architecture to achieve a broadband acoustic impedance control which can be adjusted to absorb sound in various conditions. It can also find a broad range of applications as a building block for acoustic metamaterials. The technique relies on the integration of the physical model of the CD actuator in the control function. The core of the control consists in the accurate estimation of the heat and force acoustic sources, which are proportional to the applied AC voltage in the linear approximation. In this sense, we can calculate which signal should be fed to the CD actuator in order to bring the acoustic impedance to the desired one. Due to the small thickness of the transducer, the low frequency approximation can be used, still providing enough precision to control

impedance up to approximately 2 kHz. The approach allows using a single microphone sensor for the impedance control, which makes the system even more compact than in the case of the feedback control because the particle velocity estimation is substituted by the model of the transducer.

The derived analytical transfer function cannot be directly implemented on hardware because it cannot be expressed as a rational polynomial function. One approximation is proposed in this chapter, which matches well the original function in the case of sound absorption under normal incidence if the time delay is accounted for. However, one must say that various realisations are possible. The only requirement is to keep the open-loop function stable. Thus, the implementation can potentially change depending on the hardware and target impedance.

Although the system is considered here as an open loop, the evident coupling between the actuator and the microphone exists, which also depends on the environment where the system is placed (duct, room, etc.). Moreover, the obtained transfer function is not zero at high frequencies above the range considered in the current work (Figure B.8), which might lead to the reinjection of energy. A thorough assessment of the active system stability can help explore the limitation of the described technique. Depending on the target impedance, the magnitude of the transfer function can lead to overly high voltages applied to the actuator. As a result, this reduces the sound pressure levels at which the absorber can operate. In the conducted experiments, the level did not exceed 1 Pa. The size and geometry of the actuator should be studied in more detail in order to increase the levels that could be tolerated for practical applications.

Nevertheless, the achieved bandwidth of control surpasses all existing techniques, which are based on conventional electrodynamic loudspeakers. The very distinct feature of the CD actuator that was exploited during the transfer function derivation is that it acts as a sound source but is still transparent for external sound. Thus, it does not break the continuity in the acoustic medium, which is the case with any membrane transducer type. Instead, it adds pressure and velocity to the already existing acoustic field. This property may be exploited in the applications where acoustic transparency is needed in the passive regime, for example, in non-Hermitian acoustics [138]. To highlight once more, the perfect broadband absorption was achieved in this chapter with the initially almost lossless actuator.

Conclusions

The work presented in this thesis intended to push the active noise reduction and specifically active sound absorption techniques closer to realistic industrial applications by proposing an alternative electroacoustic transducer to the conventional ones used for control. Despite extensive academic research and great industrial interest, still only few concrete examples can be found, which adopted this technology on the market. Some of the reasons behind this lie in the fact that the conventional transducers are not robust, lightweight, or compact enough, or are likely to restrict the bandwidth of control. A scientific intuition and thorough state-of-the-art analysis led us to considering a plasma-based technology. The control of air bulk with an electrical field allows abandoning the moving parts of conventional transducers, which typically limit the performance. Therefore, a dedicated to active sound control transducer was developed, which operates on the principle of a corona discharge. Although number of works investigated such discharge for sound reproduction purposes, no research was devoted to active sound control. We have been able to demonstrate that the developed actuator can be used for broadband sound absorption. The flexibility in design of this transducer, and the first results obtained in the presented work, open up a new research venue for active sound control, where a CD actuator deserves a decent place among the spectrum of other electroacoustic transducers. Here the main contributions of this thesis are outlined:

- Corona discharge-based electroacoustic transducer suitable for active sound control has been developed
- Analytical and numerical model for design, characterisation, and control has been devised
- Feedback impedance control strategies have been customised for the CD actuator resulting in broadband sound absorption under normal and grazing incidence
- Model-based feedforward approach for the CD actuator has been worked out leading to compact, broadband, reconfigurable sound control solution
- Experimental validation in laboratory conditions, including impedance tube and flow duct facility

The contributions in more detail, discussion on the current limitations, and further work are

presented below.

Contributions

Corona discharge for sound control

The specific requirements on the transducers needed for active noise reduction have been identified. Plasma-based technology has been proposed as a potential solution to mitigate some of the limitations of conventional transducers. We have analysed the known gas discharge types and focused our consideration to the dielectric barrier discharge and corona discharge. Preliminary tests have shown that a corona discharge is a more suitable basis for designing an actuator for active control due to its higher linearity. The CD-based actuator was designed in a wire-to-mesh geometry, where the high voltage electrode is composed of an array of wire segments, and the grounded electrode is a perforated metallic plate. The actuator behaves as a surface-distributed source, so the acoustic impedance can be precisely controlled. The size is limited to $50 \times 50 \text{ mm}^2$ in this work, but can be easily extended to much larger surface. Moreover, it is not restricted to a rectangular shape, but the wires can be arranged for any particular need. The frame can be fabricated out of any dielectric. Collector can be made out of any material, which surface is conducting. Thus, instead of manufacturing it from heavy metals or alloys, lighter materials can be used. For example, plastics or composites can be coated in a conducting shell. For most of the applications the high voltage part is enclosed. The enclosure can be integrated with the system, where the transducer should be placed. Thus, the high voltage wires are protected by the enclosure and the rigid collector. This makes the construction simple, lightweight, and mechanically robust. At low frequencies the actuator behaves as an ideal combination of a monopolar and dipolar acoustic sources. The harmonic distortion has been shown to evolve linearly with the magnitude of applied alternating voltage.

Electroacoustic modelling of CD actuator

Two models of the CD electroacoustic operation have been proposed. The first analytical model requires a measurement of the actuator's voltage-current characteristics to set up the model parameters. After the calibration, it can provide a low frequency estimation of the sound sources in the actuator. From this we have been able to estimate the low frequency radiation and distortion of the actuator without experimental measurements. The estimation of sources has been integrated in the control strategy described in the last chapter. The second numerical model has been developed for a more precise and independent modelling of the actuator. With this model, we have analysed the distributions of electrical field, current, charge, and consequently the heat and force source distributions. Based on this, several assumptions made in analytical model, and regarding the location of the sound sources have been validated. The simulation is capable of estimating the acoustic radiation at higher

frequencies. Importantly, we propose to employ this numerical model for designing the actuator from scratch, as it does not rely on experiment and can incorporate geometrical details of the actuator under development. The correctness of the models has been verified through the direct comparison with experimental measurements. Although the numerical model exhibited small discrepancies with the experiment, it does not diminish its usefulness.

Feedback impedance control with CD actuator

Hybrid passive-active and direct pressure-velocity feedback impedance control strategies have been implemented to absorb sound with the CD actuator. Since hybrid absorption relies on pressure minimisation behind a porous layer, and the realised impedance is defined by the properties of this layer, the strategy is fairly straightforward to implement. Its successful operation has been demonstrated. It has been shown that the airflow created by the offset voltage in the actuator does not perturb the sensors placed close to collector grid, and that broadband performance can be achieved. As only a real impedance can be realised with this method, a direct impedance control strategy can be more advantageous. For that, we have first investigated two methods of particle velocity estimation directly in the air, since the CD actuator has no moving element. This control method has also presented a broadband sound absorption under normal incidence. An active acoustic liner prototype was developed based on these two strategies to absorb sound waves in a duct under grazing incidence, with and without mean flow. Although its operation was limited in terms of the sound pressure level of external noise and low frequency performance in the presence of the mean flow, the achieved bandwidth is very competitive to the liner prototypes proposed in the literature and can be tuned digitally. With the pressure-velocity feedback we have been able to digitally reconfigure the noise attenuation from broadband to a specific frequency band.

Model-based impedance control

An alternative feedforward impedance control method has been developed. Instead of measuring all acoustic quantities with sensors and feeding them back in a loop, a physical model of the CD is used to estimate the transducer dynamics. The model of the CD actuator and the target impedance are embedded in a functional relationship between the input measurement of sound pressure in front of the actuator and the electrical voltage applied to the electrodes. Since the obtained analytical formula should be represented as a rational polynomial of the Laplace variable s to be implemented on a real-time control platform, it has been shown that the final performance at high frequencies significantly depends on the quality of approximation. Finally, the CD-based sound absorption system has been obtained, which operates with a single microphone. The achieved impedance and absorption coefficient meet target values over a broad frequency range. Targeting different resistances has been performed with some success. Frequency dependent impedance to tune the system to different magnitude and phase of sound reflection was demonstrated.

Current limitations and suggestions for improvement

Feedback and feedforward model-based approach comparison

In different scenarios, feedback or feedforward model-based control of a CD actuator may be preferred.

All studied control methods allow achieving a broadband sound absorption under normal incidence. In the thesis, the frequency range from 100 to 2000 Hz was considered, limited at the lower bound by the control microphones and closely placed termination at the rear of the device. There is theoretically no constraint imposed by the CD actuator. However, the low frequency particle velocity estimation is complicated with a pair of closely spaced microphones because the pressure difference approaches a noise limit. A greater spacing should be used, increasing the size of the setup, or a resistive layer between the sensors, which limits the lowest achievable resistance. On the other hand, we demonstrated the control down to 20 Hz with a single microphone in the case of a feedforward model-based approach (see Figure ??). Therefore, the latter strategy allows controlling low frequency sound more easily than pressure-velocity impedance control. Hybrid absorption, alternatively, should not experience any issues to minimise the pressure behind a porous layer.

A feedforward model-based approach appeared to be more compact compared to feedback ones. Since it does not require a second sensor or a porous layer, the target impedance is realised closer to the collector grid. It could be more advantageous for grazing incidence absorption because it is essential to realise a target impedance at the plane closest to the duct wall. Unfortunately, it was not assessed because the tests in the flow duct were conducted before the approach was developed.

The impedance control with a feedforward approach presents a more stable operation than pressure-velocity feedback. To achieve a higher proportional gain in the control loop, a 10 mm melamine layer is placed at the back, that introduces a little additional absorption and increases stability at high frequencies. Therefore, passive absorption was already higher for this method than a feedforward control. The hybrid technique was always stable because after the adaptation, FIR filters coefficients were fixed and did not change during the experiment. The stability of the pressure-velocity feedback control could be improved by increasing the quality of velocity estimation and introducing a more complex control than a proportional one only.

If the environmental conditions, such as static pressure, humidity, or temperature, vary significantly, the feedback type of control may appear more suitable. Indeed, voltage-current characteristics might change, and some model parameters such as ion mobility depend on these conditions. If the environment where the system is placed does not considerably change during operation, a model-based approach could be chosen due to other advantages mentioned above. Finally, a solution that employs a model-based feedforward approach, and reestimates the parameters periodically, could be investigated.

Sound pressure level

As observed throughout this thesis, the CD actuator could absorb sounds at low frequencies with pressure magnitudes around 1 Pa, but not much higher. From the Bode plot of the control transfer function in Chapter 6, we could observe that the magnitude of θ at low frequencies was close to 750 V/Pa to target full absorption. It means that to cope with higher sound pressure levels, a higher dynamic range in voltage should be available. First, the actuator can be designed for higher voltages. Consequently, a greater span of u_{AC} can be used. Second, the electrodes can be designed differently in order to bring the actuator closer to the theoretical limits of electrical breakdown because it happens considerably earlier in the experiment. For example, the collector electrode can be composed of an array of cylinders whose surface is smoother than a perforated plate. Finally, an absolutely alternative, more efficient approach to ionise the air could be imagined since the core idea is to control the air with an electrical field and corona discharge is just one realisation.

High voltage amplifier

To operate the CD actuator, a high voltage amplifier is needed. This element can represent an obstacle to the wide application of CD-based active control. The first difficulty consists in designing an amplifier capable of simultaneously applying constant high voltage U_{DC} and alternating voltage u_{AC} . Currently available amplifiers are intended for research purposes, so they are heavy (in the range of 10 kg), bulky (full rack amplifier), and costly, limiting the application of a CD-based absorber as a lightweight, compact, cost-efficient solution. If multiple channels are needed to control an array of transducers, the problem deteriorates further. Alternatively, the emitter wires of the CD could be powered with the DC voltage only, and the AC component could be applied separately to the collector electrode. However, in this case, the sensors placed close to the collector are less protected because of exposure to voltages up to 1 kV and possible electromagnetic interference from a discharge. Therefore, applying the whole signal to the emitter wires and keeping the collector grounded is more preferable. We believe that such an amplification system is not present on the market yet because of the absence of industrial demand. In the case of the successful development of CD-based sound absorbing systems, the amplification would become more affordable and practically suitable.

We have developed a simple amplification scheme adapted for a corona discharge actuator. The description and the test of the prototype are presented in Appendix A.

Early arcing

Air becomes conductive if the electrical field magnitude exceeds 3 MV/m. When the electrical field in the drift region of corona discharge approaches this value, the actuator shorts in an electrical arc. In practice, such transition occurs for considerably lower electrical fields. As

a result, the voltage range of stable corona discharge is narrower, which limits the maximal transducer's power. One of the most important reasons for early arcing is the geometry of the electrodes and the quality of their surface. Few modifications can be made in order to shift the transition to the arc. The perforated plate, used in this thesis as the collector electrode, can be replaced by an array of conducting cylinders. In Figures 3.5 and B.3 showing the electrical field distribution, one can notice that the electric field at the collector edges is increased. This field at high voltages creates local corona discharges, which do not participate in the sound manipulation but reduce the stability of the discharge. A larger radius of curvature of cylinders can suppress this effect and can allow operating on a broader voltage range. Another drawback observed during the experimental campaign consists in surface arcing. Since a surface arc propagates easier than a volumetric one, the frame separating the electrodes can be modified. It can be designed in such a way that the shortest path along its surface between the electrodes is longer than the air separation of the electrodes, thus, reducing the possibility of a surface arc. Therefore, we suggested several improvements to the actuator's geometry to extend its dynamic voltage range.

Ozone generation

While generating positive ions, the discharge also produces other species in the air, including ozone. Ozone is toxic and is considered to be harmful to humans during extended exposure. Although ozone generation by the CD actuators does not pose any problems in the applications, such as aircraft noise reduction, interior sound absorption requires the removal of hazardous gas. Activated carbon filters are known for the efficient decomposition of ozone into oxygen. Such a filter represents a porous layer with a constant but not high flow resistance [139]. Thus, it can be either advantageously used, for example, in a hybrid absorption method, as a part of a resistive layer, or taken into account, when designing any impedance control implementation. Moreover, the combination of corona discharge sound absorber with air purification can be considered.

Further work

Sound absorber design

The main venue of further research is directed to address the current limitations of the developed system and to raise confidence in its industrial applicability. Simulation and validation of the CD-based sound absorption concept were performed only in the 1D case in this thesis. The application of the absorbers in 3D environment would require the design of larger-sized actuators, within a multichannel control system. First, the ways to increase the sound pressure level at which the absorber can operate should be investigated. This includes further geometry optimisation and suppression of early arcing. From a control perspective, possible deviation of the model parameters after long operation of the feedforward-based absorber

and its influence on control stability should be investigated. The stability margins can be studied in more detail for feedback techniques.

CD as an active acoustic metamaterial

CD actuator can be used as a building block in future generations of acoustic metamaterials and realise non-reciprocal, non-Hermitian and topological systems with new functionalities and large bandwidth, bringing them closer to real applications. A unique feature of the CD actuator is its sound transparency in the passive regime. In contrast to membrane transducers, it does not need to be controlled to maintain transmission if installed transversely in a duct [138]. Additionally, we emphasise again that the shape of the electrodes and the active area can be customised without any impact on the frequency response in the low and medium ranges. This may find promising applications in complex source design, imaging, large metasurfaces and acoustic arrays, especially when a nonconventional shape of the active unit cell is required.

A Simple high voltage amplifier

The proposed design of a high voltage amplifier resembles the configuration of a typical class A audio amplifier with the additional feedback circuit. The actuator is biased with a circuit that generates constant high voltage, and the AC amplified component is added with the help of a high voltage vacuum tube. The block scheme is illustrated in Figure A.1.

The DC amplification circuit comprises a DC power supply, a switched-mode circuit connected to and fed by the DC power supply, a flyback transformer connected to the output of the switched-mode circuit, and a rectifier after the transformer. Switched-mode circuit generates a fast alternating signal, which further feeds the transformer. The transformer is wound amplifies the input alternating voltage by the factor of 1000. The signal is further rectified by the rectifier, which is composed of high voltage diodes and capacitors. Since rectification is never ideal, a high-frequency component from the oscillator circuit remains in the voltage output of the rectifier. To eliminate any acoustic noise caused by this, the switched-mode circuit operates at a relatively high frequency, chosen sufficiently greater than the audible range, for instance, around 40 kHz. The amplified high DC voltage is connected to the CD emitter wires via a load resistor.

The input low voltage alternating signal (controller output, for example) should be also amplified. This part is based on vacuum tubes. This solution is used because the transistors are either expensive or unavailable for this voltage range. Several tubes can be connected in parallel in order to increase the power. The cathode of the vacuum tube is heated by a low voltage DC or AC source, shown as heater in Figure A.1. A constant anode-cathode electrical current is induced by connecting the high DC voltage from the flyback transformer output to the anode of the vacuum tube, while its cathode is grounded. The modulation of the current is created by connecting the input signal to a control grid electrode of the vacuum tube. The high voltage modulation is done by pushing the current through a load resistor. The output high AC voltage component equals to the product of the load resistance and the amplitude of anode current change. The high DC voltage component feeding the CD actuator equals to the difference of DC voltage supply (12 kV in the example) and the constant voltage drop in the load resistor. Thus, both amplification factor of AC signal and bias voltage depend on

the choice of the load resistor. To eliminate this dependence and make the amplifier load independent, the feedback circuit is added.

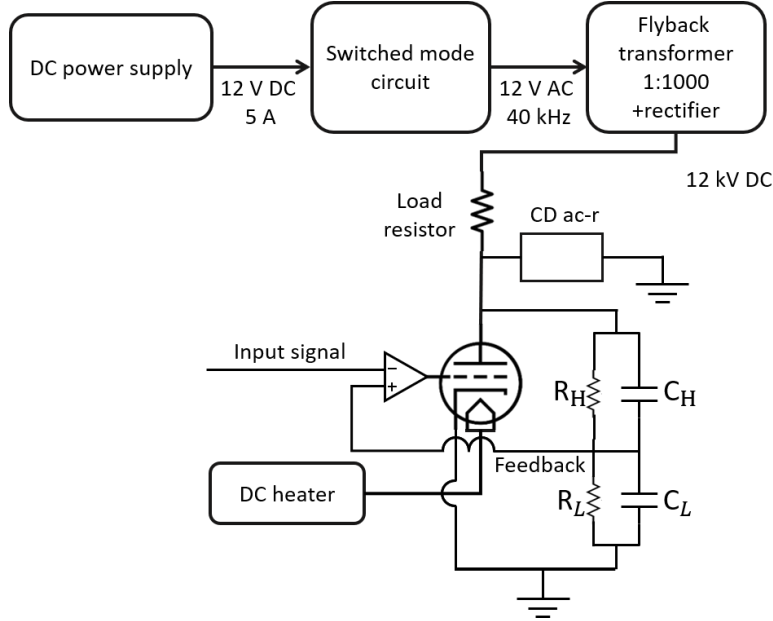


Figure A.1: Block scheme of the high voltage amplifier for a corona discharge (single amplification channel is illustrated).

Feedback is added from the output of the vacuum tube (anode) via the voltage divider to the vacuum tube input. The voltage divider contains resistors and capacitors R_H , R_L , C_H , C_L . Any of the resistors or capacitors can be represented by series or parallel combination of the components in order to obtain a needed resistance or capacitance. The magnitude of DC voltage at the feedback line compared to the voltage at the output of the tube is then $R_L / (R_H + R_L) \approx R_L / R_H$ if $R_H \gg R_L$. The magnitude of AC voltage at the feedback line compared to the voltage at the output of the tube is then $C_H / (C_H + C_L) \approx C_H / C_L$, if $C_L \gg C_H$. For instance, if $R_H = 100 \text{ MOhm}$, $R_L = 100 \text{ KOhm}$, $C_H = 3 \text{ pF}$, $C_L = 3 \text{ nF}$, the divider ratio is close to 1000:1 in the whole frequency spectrum. The divider ratio fixes the amplification gain of the amplifier, which is not dependent on the load resistor anymore. The feedback signal is connected to the non-inverting input of an operational amplifier. The output of the operational amplifier is connected to the control grid of the tube. If the control signal containing bias DC signal and AC signal feeds the inverting input of the operational amplifier, the resulting voltage on the tube output and therefore on emitter electrode of the transducer is amplified by the divider ratio. Finally, addition of the feedback path forces the output of the amplifier to follow the input multiplied by the divider ratio.

The amplifier was assembled according to the described schematic. The photo of its two channel version is shown in Figure A.2. The amplifier has common low voltage DC supplies for both channels. Two high voltage tetrodes 6E15P are connected in parallel in each channel. Finally, the prototype is rather simple, light, and compact. It can be further optimized by

creating custom components instead of assembling from available on the market. Figure A.3

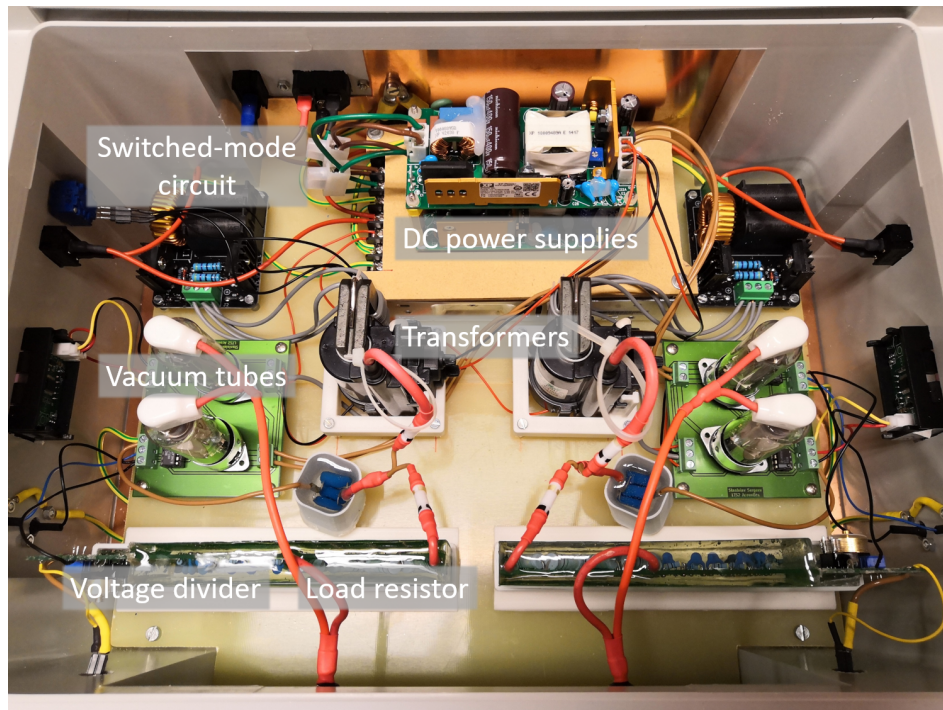


Figure A.2: Photo of two channel high voltage amplifier for a corona discharge actuator.

demonstrates frequency response of one channel of the amplifier, when it powers the 5×5 cm² prototype. Due to the feedback, the amplification factor is kept 1000 precisely. Both magnitude and phase responses are flat. At higher frequencies the response can be low-passed. The frequency of a low-pass is defined by the combination of the load resistor and capacitance of the CD actuator. Nevertheless, this amplifier allows amplifying the signal without noticeable delay in the audible frequency range, which provides more flexibility in a control design.

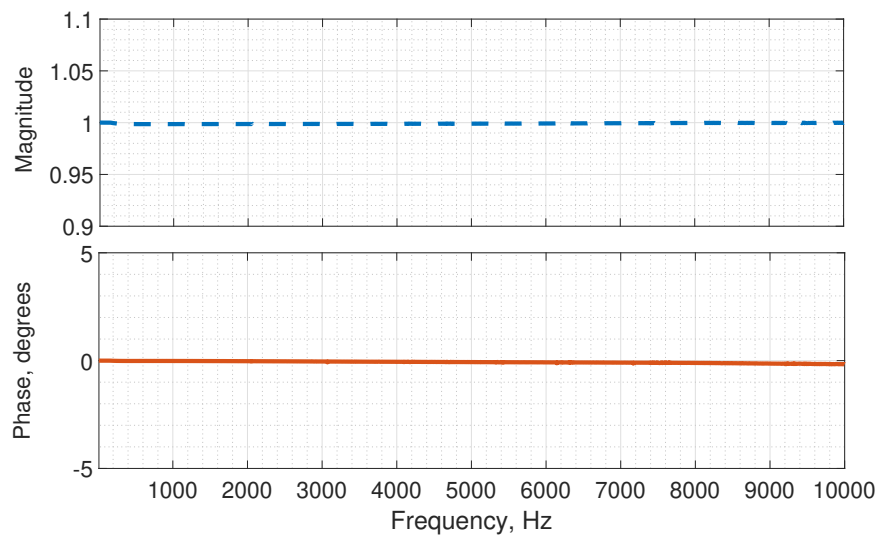


Figure A.3: Frequency response of the amplifier from Figure A.2, when it is connected to the CD actuator.

B Additional figures and data

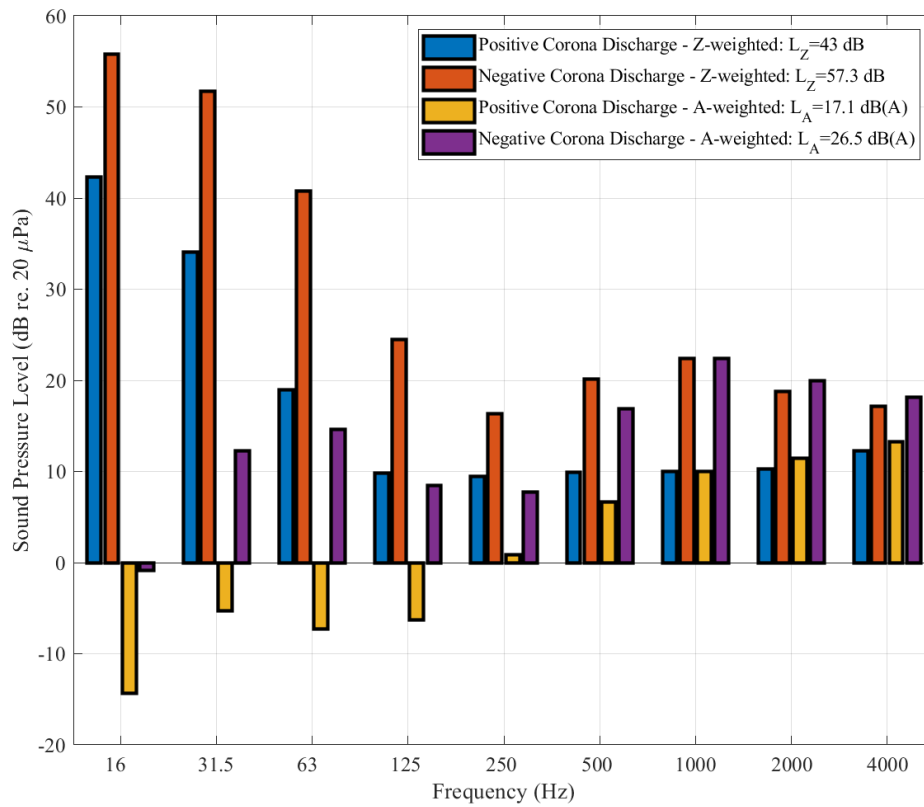


Figure B.1: A- and Z- weighted noise levels over octave bands produced by a positive and negative corona discharges. Constant voltage level $U_{DC} = \pm 8.2$ kV is applied. Microphone is placed at 1 m in front of the actuator.

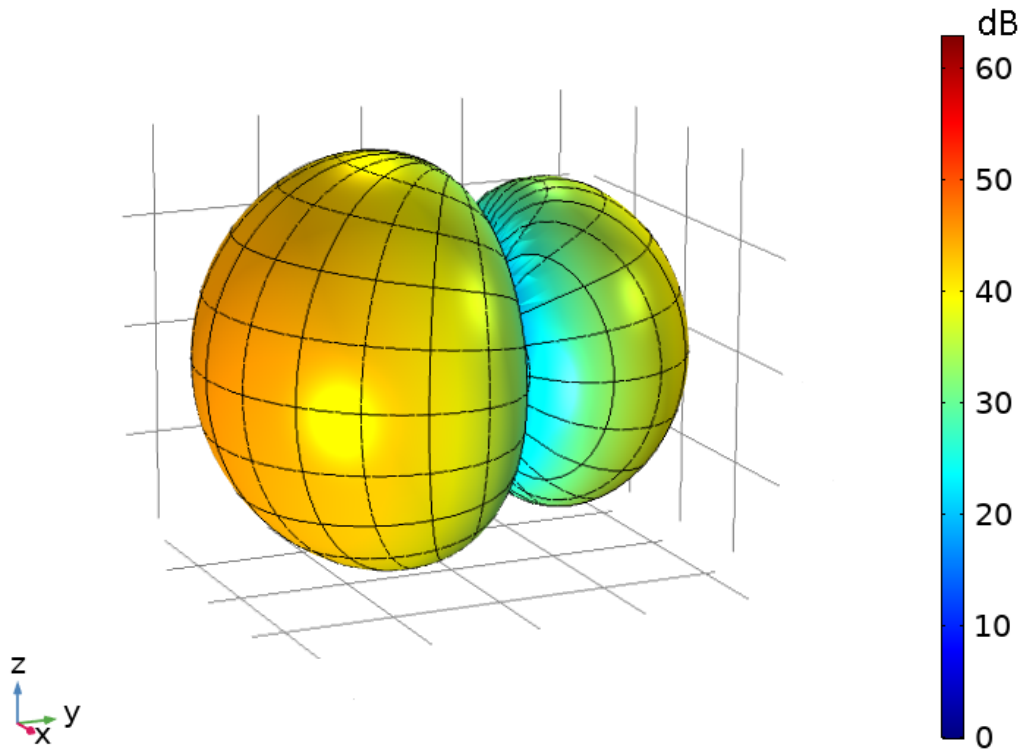


Figure B.2: Three dimensional directivity of the corona discharge actuator at 1000 Hz. $U_{DC} = 8.2$ kV, $u_{AC} = 300$ Vrms.

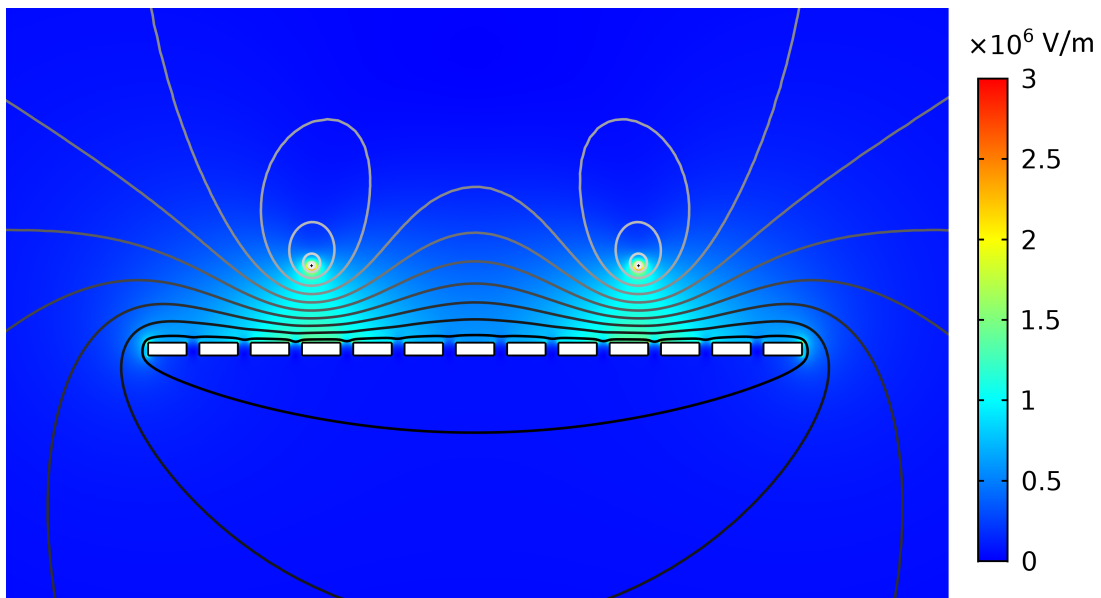


Figure B.3: Electric field magnitude with equipotential lines of the CD actuator, where the emitter electrode is composed of two wires. A constant voltage of $U_{DC} = 8.2$ kV is applied.

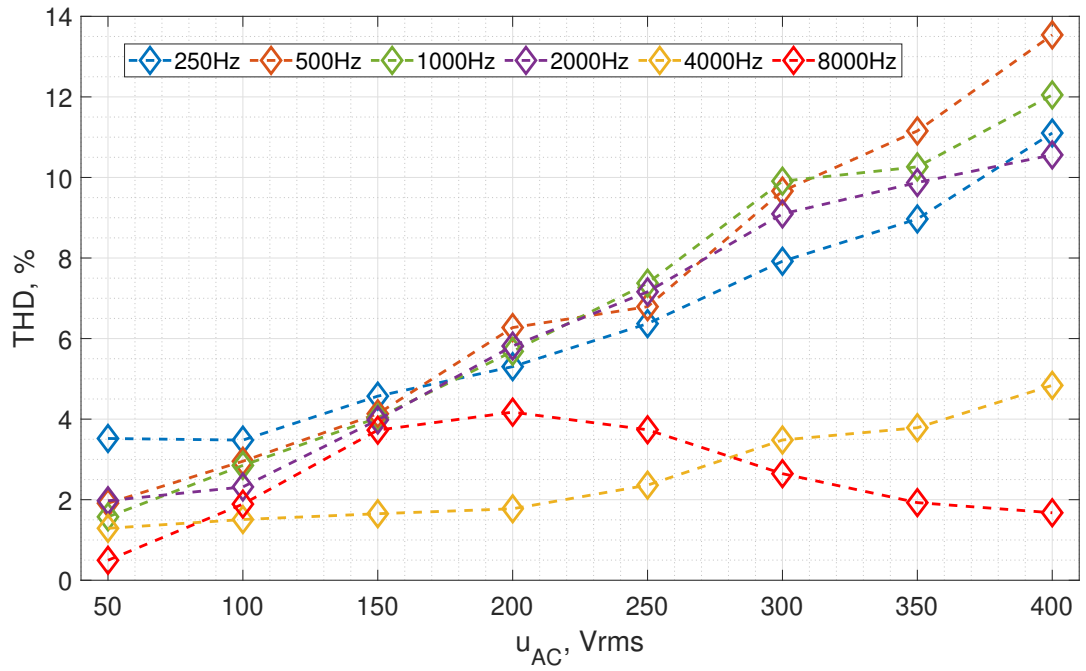


Figure B.4: Total harmonic distortion in percents of the CD actuator at frequencies 250, 500, 1000, 2000, 4000, 8000 Hz. The actuator is biased with $U_{DC} = -8.2$ kV.

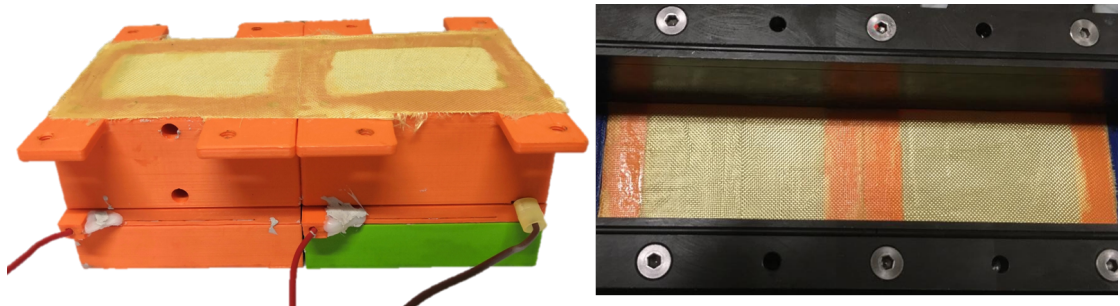


Figure B.5: Test section with the plasma-based liner prototype mounted on a side wall. Left - two active cells comprising the liner (one is partially disassembled for illustrative purpose). Right - view from the duct inside, top cover is removed. The liner is assembled for the pressure-velocity feedback configuration.

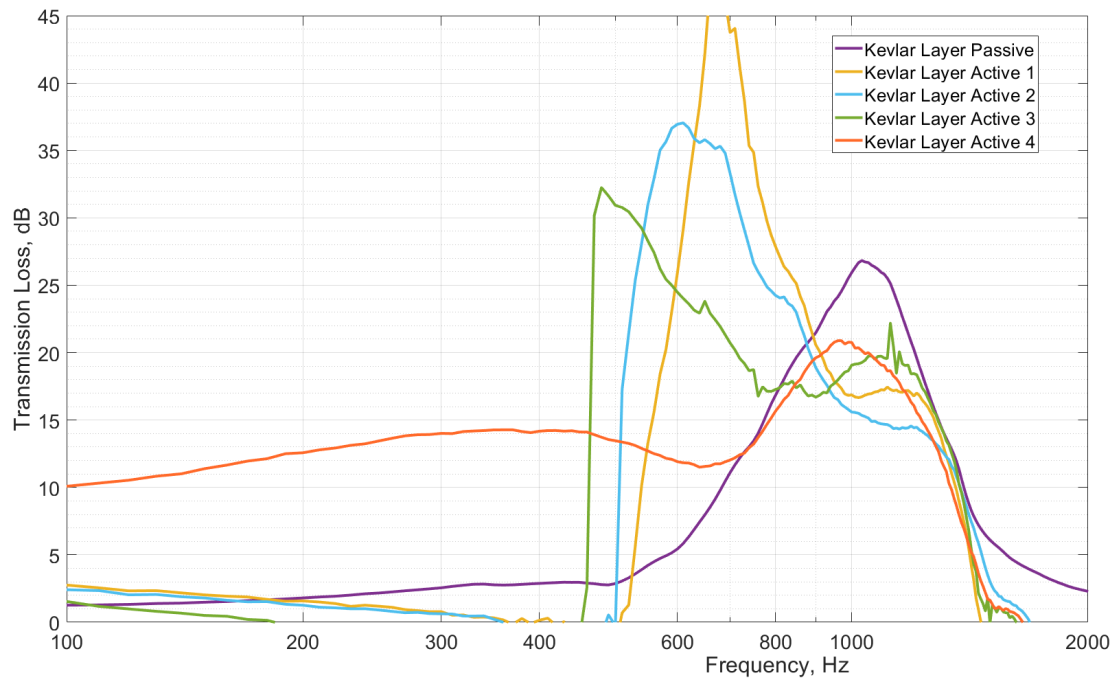


Figure B.6: Transmission loss measurement with active impedance control method. No mean flow, sound pressure level of acoustic signal is 90 dB. Only $TL+$ curves are illustrated.

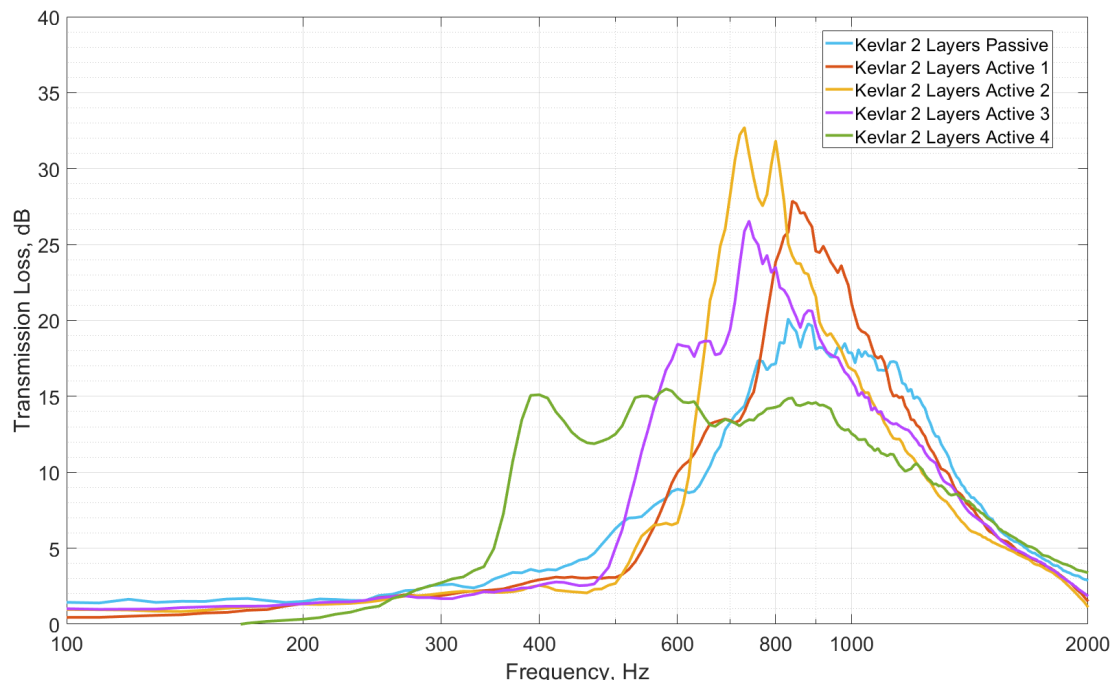


Figure B.7: Transmission loss measurement with active impedance control method. Mean flow with $M=0.03$, sound pressure level of acoustic signal is 95 dB. Only $TL+$ curves are illustrated

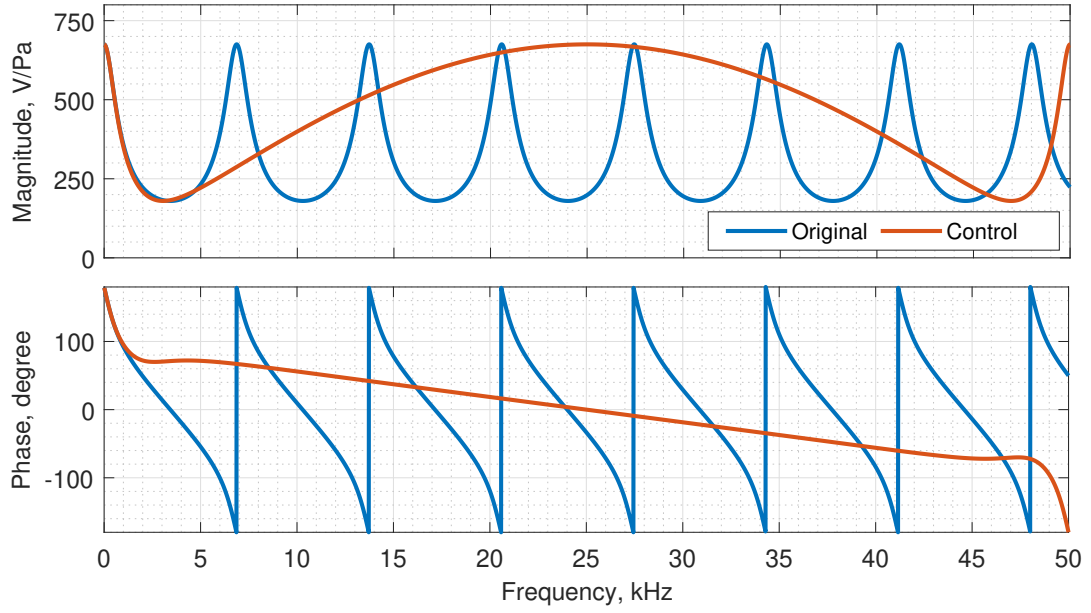


Figure B.8: Bode plots of transfer functions $\theta(\omega)$ from (6.7) and $\theta(s)$ from (6.9) with target impedance $Z_{tg} = \rho c$. The response is shown in the frequency range 10-50000 Hz.

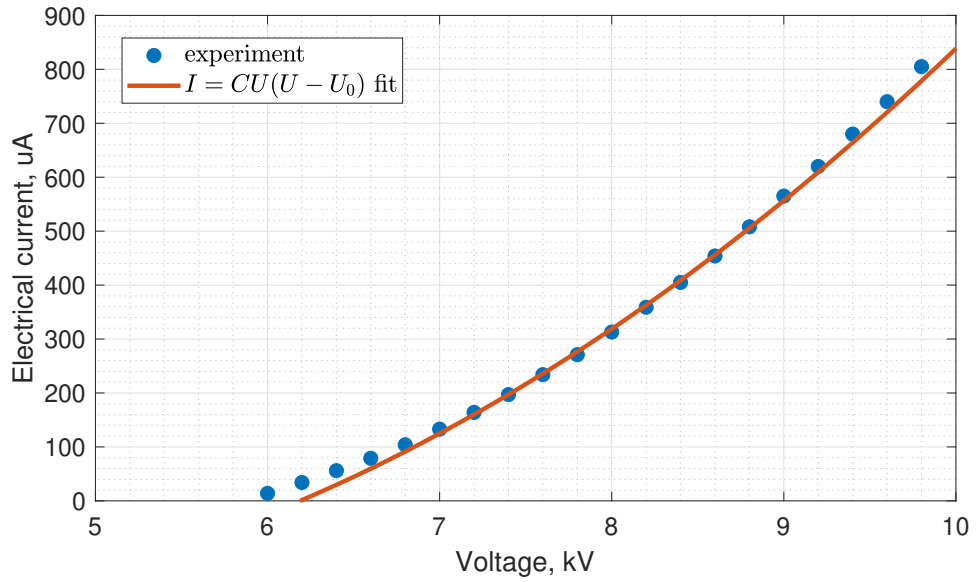


Figure B.9: Voltage-current characteristics of the corona discharge actuator measured for Chapter 6. Blue dots - measurements; red curve - least mean square fit of experimental data with formula $I = CU(U - U_0)$, $C = 2.31e - 11 \text{ A/V}^2$, $U_0 = 6190 \text{ V}$.

Bibliography

- [1] World Health Organization et al. *Burden of disease from environmental noise: Quantification of healthy life years lost in Europe*. World Health Organization. Regional Office for Europe, 2011.
- [2] Anke Huss, Adrian Spoerri, Matthias Egger, and Martin Röösli. “Aircraft noise, air pollution, and mortality from myocardial infarction”. In: *Epidemiology* (2010), pp. 829–836.
- [3] Antonio Filippone. “Aircraft noise prediction”. In: *Progress in Aerospace Sciences* 68 (2014), pp. 27–63.
- [4] Matthew Marino, Obaid Siddique, and Roberto Sabatini. “Benefits of the blended wing body aircraft compared to current airliners”. In: *First International Symposium on Sustainable Aviation*. 2015.
- [5] XuQiang Ma and ZhengTao Su. “Development of acoustic liner in aero engine: a review”. In: *Science China Technological Sciences* (2020), pp. 1–14.
- [6] Xia Hua, Alan Thomas, and Kurt Shultis. “Recent progress in battery electric vehicle noise, vibration, and harshness”. In: *Science Progress* 104.1 (2021), p. 00368504211005224.
- [7] Harry F Olson and Everett G May. “Electronic sound absorber”. In: *The Journal of the Acoustical Society of America* 25.6 (1953), pp. 1130–1136.
- [8] P.A. Nelson and S.J. Elliott. *Active Control of Sound*. v. 3. Elsevier Science, 1992. ISBN: 9780125154253.
- [9] Sen M Kuo and Dennis R Morgan. “Active noise control: a tutorial review”. In: *Proceedings of the IEEE* 87.6 (1999), pp. 943–973.
- [10] Jean Claude Carmona and Victor M Alvarado. “Active noise control of a duct using robust control theory”. In: *IEEE Transactions on control systems technology* 8.6 (2000), pp. 930–938.
- [11] Huiyuan Sun, Thushara D Abhayapala, and Prasanga N Samarasinghe. “A realistic multiple circular array system for active noise control over 3D space”. In: *IEEE/ACM Transactions on Audio, Speech, and Language Processing* 28 (2020), pp. 3041–3052.
- [12] Jean Allard and Noureddine Atalla. *Propagation of sound in porous media: modelling sound absorbing materials 2e*. John Wiley & Sons, 2009.

-
- [13] Steven A. Cummer, Johan Christensen, and Andrea Alù. “Controlling sound with acoustic metamaterials”. In: *Nature Reviews Materials* 1.16001 (2016). ISSN: 20588437.
 - [14] D. Guicking and E. Lorenz. “An Active Sound Absorber With Porous Plate”. In: *Journal of Vibration, Acoustics, Stress, and Reliability in Design* 106.3 (July 1984), pp. 389–392. ISSN: 0739-3717.
 - [15] Romain Boulandet. “Tunable Electroacoustic Resonators through Active Impedance Control of Loudspeakers”. In: (2012), p. 220.
 - [16] Etienne Thierry Jean-Luc Rivet. “Room Modal Equalisation with Electroacoustic Absorbers”. In: (2016), p. 203.
 - [17] Mario Rossi. *Acoustics and electroacoustics*. Artech House Publishers, 1988.
 - [18] Eric Moreau. “Airflow control by non-thermal plasma actuators”. In: *Journal of physics D: applied physics* 40.3 (2007), p. 605.
 - [19] Trevor Cox and Peter d’Antonio. *Acoustic absorbers and diffusers: theory, design and application*. Crc Press, 2016.
 - [20] Soon-Hong Park. “Acoustic properties of micro-perforated panel absorbers backed by Helmholtz resonators for the improvement of low-frequency sound absorption”. In: *Journal of Sound and Vibration* 332.20 (2013), pp. 4895–4911.
 - [21] Sibio Huang, Xinsheng Fang, Xu Wang, Badreddine Assouar, Qian Cheng, and Yong Li. “Acoustic perfect absorbers via Helmholtz resonators with embedded apertures”. In: *The Journal of the Acoustical Society of America* 145.1 (2019), pp. 254–262.
 - [22] Dan Zhao and Aimee S Morgans. “Tuned passive control of combustion instabilities using multiple Helmholtz resonators”. In: *Journal of sound and vibration* 320.4-5 (2009), pp. 744–757.
 - [23] A Doria. “Control of acoustic vibrations of an enclosure by means of multiple resonators”. In: *Journal of Sound and Vibration* 181.4 (1995), pp. 673–685.
 - [24] W Frommhold, HV Fuchs, and S Sheng. “Acoustic performance of membrane absorbers”. In: *Journal of Sound and Vibration* 170.5 (1994), pp. 621–636.
 - [25] Martin Dannemann, Michael Kucher, Eckart Kunze, Niels Modler, Karsten Knobloch, Lars Enghardt, Ennes Sarradj, and Klaus Höschler. “Experimental study of advanced helmholtz resonator liners with increased acoustic performance by utilising material damping effects”. In: *Applied Sciences* 8.10 (2018), p. 1923.
 - [26] Ahmed Abbad, Nouredine Atalla, Morvan Ouisse, and Olivier Doutres. “Numerical and experimental investigations on the acoustic performances of membraned Helmholtz resonators embedded in a porous matrix”. In: *Journal of Sound and Vibration* 459 (2019), p. 114873.
 - [27] “Dark acoustic metamaterials as super absorbers for low-frequency sound”. In: *Nature Communications* 3 (2012). ISSN: 20411723.

BIBLIOGRAPHY

- [28] Guancong Ma, Min Yang, Songwen Xiao, Zhiyu Yang, and Ping Sheng. “Acoustic meta-surface with hybrid resonances”. In: *Nature Materials* 13.9 (2014), pp. 873–878. ISSN: 14764660.
- [29] V. Romero-García, G. Theocharis, O. Richoux, A. Merkel, V. Tournat, and V. Pagneux. “Perfect and broadband acoustic absorption by critically coupled sub-wavelength resonators”. In: *Scientific Reports* 6.January (2016), pp. 6–13. ISSN: 20452322.
- [30] Yong Li and Badreddine M. Assouar. “Acoustic metasurface-based perfect absorber with deep subwavelength thickness”. In: *Applied Physics Letters* 108.6 (2016). ISSN: 00036951.
- [31] Yves Aurégan. “Ultra-thin low frequency perfect sound absorber with high ratio of active area”. In: *Applied Physics Letters* 113.20 (2018). ISSN: 00036951.
- [32] Badreddine Assouar, Bin Liang, Ying Wu, Yong Li, Jian Chun Cheng, and Yun Jing. “Acoustic metasurfaces”. In: *Nature Reviews Materials* 3.12 (2018), pp. 460–472. ISSN: 20588437.
- [33] Yufan Tang, Shuwei Ren, Han Meng, Fengxian Xin, Lixi Huang, Tianning Chen, Chuanzeng Zhang, and Tian Jian Lu. “Hybrid acoustic metamaterial as super absorber for broad-band low-frequency sound”. In: *Scientific Reports* 7.1 (2017), pp. 1–11.
- [34] Nesbitt W Hagood and Andreas Von Flotow. “Damping of structural vibrations with piezoelectric materials and passive electrical networks”. In: *Journal of sound and vibration* 146.2 (1991), pp. 243–268.
- [35] Andrew J Fleming, Dominik Niederberger, SO Reza Moheimani, and Manfred Morari. “Control of resonant acoustic sound fields by electrical shunting of a loudspeaker”. In: *IEEE transactions on control systems technology* 15.4 (2007), pp. 689–703.
- [36] Xin Li, Zhigang Cao, Zihao Li, and Bilong Liu. “Sound absorption of a shunt loudspeaker on a perforated plate”. In: *Applied Acoustics* 193 (2022), p. 108776.
- [37] Min Yang, Shuyu Chen, Caixing Fu, and Ping Sheng. “Optimal sound-absorbing structures”. In: *Materials Horizons* 4.4 (2017), pp. 673–680. ISSN: 20516355.
- [38] Theodoros T Koutserimpas, Etienne Rivet, Hervé Lissek, and Romain Fleury. “Active acoustic resonators with reconfigurable resonance frequency, absorption, and bandwidth”. In: *Physical Review Applied* 12.5 (2019), p. 054064.
- [39] Chaoeng Bao, Paul Sas, and Hendrik Van Brussel. “Adaptive active control of noise in 3-D reverberant enclosures”. In: *Journal of sound and vibration* 161.3 (1993), pp. 501–514.
- [40] Iman Tabatabaei Ardekani and Waleed H Abdulla. “Active noise control in three dimensions”. In: *IEEE Transactions on control systems technology* 22.6 (2014), pp. 2150–2159.
- [41] C Pinhède, D Habault, E Friot, and Ph Herzog. “Active control of the field scattered by the rigid wall of a semi-anechoic room—Simulations and full-scale off-line experiment”. In: *Journal of Sound and Vibration* 506 (2021), p. 116134.

-
- [42] Romain Boulandet and H Lissek. "Optimization of electroacoustic absorbers by means of designed experiments". In: *Applied acoustics* 71.9 (2010), pp. 830–842.
 - [43] Jiancheng Tao, Ruixiang Jing, and Xiaojun Qiu. "Sound absorption of a finite micro-perforated panel backed by a shunted loudspeaker". In: *The Journal of the Acoustical Society of America* 135.1 (2014), pp. 231–238.
 - [44] Hervé Lissek, Romain Boulandet, and Romain Fleury. "Electroacoustic absorbers: bridging the gap between shunt loudspeakers and active sound absorption". In: *The Journal of the Acoustical Society of America* 129.5 (2011), pp. 2968–2978.
 - [45] Etienne Rivet, Sami Karkar, and Hervé Lissek. "Broadband low-frequency electroacoustic absorbers through hybrid sensor-/shunt-based impedance control". In: *IEEE Transactions on Control Systems Technology* 25.1 (2016), pp. 63–72.
 - [46] Xinxin Guo, Maxime Volery, and Hervé Lissek. "PID-like active impedance control for electroacoustic resonators to design tunable single-degree-of-freedom sound absorbers". In: *Journal of Sound and Vibration* 525 (2022), p. 116784.
 - [47] Maxime Volery, Xinxin Guo, and Herve Lissek. "Robust direct acoustic impedance control using two microphones for mixed feedforward-feedback controller". In: (2021).
 - [48] XH Duan, HQ Wang, ZB Li, LK Zhu, R Chen, DY Kong, and Z Zhao. "Sound absorption of a flexible micro-perforated panel absorber based on PVDF piezoelectric film". In: *Applied Acoustics* 88 (2015), pp. 84–89.
 - [49] Limin Gu, Chunyu Zhao, Kaiqi Wang, Senlei Li, Xiaole Wang, and Zhenyu Huang. "Asymmetric sound absorption achieved by double-layer piezoelectric metamaterials with tunable shunt circuit". In: *Applied Physics Letters* 119.13 (2021), p. 131903.
 - [50] So Klein. "Un nouveau transducteur électroacoustique: l'ionophone". In: *Acta Acustica united with Acustica* 4.1 (1954), pp. 77–79.
 - [51] MK Lim. "A corona-type point source for model studies in acoustics". In: *Applied Acoustics* 14.4 (1981), pp. 245–252.
 - [52] S Nijdam, E Takahashi, J Teunissen, and U Ebert. "Streamer discharges can move perpendicularly to the electric field". In: *New Journal of Physics* 16.10 (2014), p. 103038.
 - [53] Fedor K Popov and Mikhail N Shneider. "Sound produced by an oscillating arc in a high-pressure gas". In: *Journal of Applied Physics* 122.5 (2017), p. 053303.
 - [54] VR Soloviev and VM Krivtsov. "Surface barrier discharge modelling for aerodynamic applications". In: *Journal of Physics D: Applied Physics* 42.12 (2009), p. 125208.
 - [55] Luc Leger, Eric Moreau, and Gérard Touchard. "Control of low velocity airflow along a flat plate with a DC electrical discharge". In: *Conference Record of the 2001 IEEE Industry Applications Conference. 36th IAS Annual Meeting (Cat. No. 01CH37248)*. Vol. 3. IEEE. 2001, pp. 1536–1543.
 - [56] A Berendt, J Podliński, and J Mizeraczyk. "Innovative dbd plasma actuators for airflow control". In: *30th ICPIG*. Citeseer. 2011, pp–28.

BIBLIOGRAPHY

- [57] Nicolas Benard and Eric Moreau. “Electrical and mechanical characteristics of surface AC dielectric barrier discharge plasma actuators applied to airflow control”. In: *Experiments in Fluids* 55.11 (2014), pp. 1–43.
- [58] Thomas C Corke, Martiqua L Post, and Dmitriy M Orlov. “Single dielectric barrier discharge plasma enhanced aerodynamics: physics, modeling and applications”. In: *Experiments in Fluids* 46.1 (2009), pp. 1–26.
- [59] Philip Peschke. “Experimental Investigation of Pulsed DBD Plasma Actuators for Aerodynamic Flow Control”. In: (2014).
- [60] Flint O Thomas, Alexey Kozlov, and Thomas C Corke. “Plasma actuators for cylinder flow control and noise reduction”. In: *AIAA journal* 46.8 (2008), pp. 1921–1931.
- [61] VF Kopiev, PN Kazansky, VA Kopiev, IA Moralev, and M Yu Zaytsev. “HF DBD plasma actuators for reduction of cylinder noise in flow”. In: *Journal of Physics D: Applied Physics* 50.47 (2017), p. 475204.
- [62] Laith Ayad Al-Sadawi. “Vortex shedding-induced noise reduction using (DBD) plasma actuator”. PhD thesis. Brunel University London, 2018.
- [63] Xun Huang and Xin Zhang. “Streamwise and spanwise plasma actuators for flow-induced cavity noise control”. In: *Physics of fluids* 20.3 (2008), p. 037101.
- [64] Chul Kim, Kwang-Chul Noh, Sang-Yoon Kim, and Jungho Hwang. “Electric propulsion using an alternating positive/negative corona discharge configuration composed of wire emitters and wire collector arrays in air”. In: *Applied Physics Letters* 99.11 (2011), p. 111503.
- [65] Haofeng Xu, Yiou He, and Steven RH Barrett. “A dielectric barrier discharge ion source increases thrust and efficiency of electroaerodynamic propulsion”. In: *Applied Physics Letters* 114.25 (2019), p. 254105.
- [66] B Komeili, JS Chang, GD Harvel, CY Ching, and D Brocilo. “Flow characteristics of wire-rod type electrohydrodynamic gas pump under negative corona operations”. In: *Journal of Electrostatics* 66.5-6 (2008), pp. 342–353.
- [67] Daniel S Drew, Nathan O Lambert, Craig B Schindler, and Kristofer SJ Pister. “Toward controlled flight of the ionocraft: a flying microrobot using electrohydrodynamic thrust with onboard sensing and no moving parts”. In: *IEEE Robotics and Automation Letters* 3.4 (2018), pp. 2807–2813.
- [68] Hari Krishna Hari Prasad, Ravi Sankar Vaddi, Yogesh M Chukewad, Elma Dedic, Igor Novosselov, and Sawyer B Fuller. “A laser-microfabricated electrohydrodynamic thruster for centimeter-scale aerial robots”. In: *PloS one* 15.4 (2020), e0231362.
- [69] Haofeng Xu, Yiou He, Kieran L Strobel, Christopher K Gilmore, Sean P Kelley, Cooper C Hennick, Thomas Sebastian, Mark R Woolston, David J Perreault, and Steven RH Barrett. “Flight of an aeroplane with solid-state propulsion”. In: *Nature* 563.7732 (2018), pp. 532–535.

-
- [70] Kiichiro Matsuzawa. "Sound sources with corona discharges". In: *The Journal of the Acoustical Society of America* 54.2 (1973), pp. 494–498.
- [71] Francois Bastien. "Acoustics and gas discharges: applications to loudspeakers". In: *Journal of Physics D: Applied Physics* 20.12 (1987), p. 1547.
- [72] Ph Béquin, Kaëlig Castor, Ph Herzog, and Valérie Montembault. "Modeling plasma loudspeakers". In: *The Journal of the Acoustical Society of America* 121.4 (2007), pp. 1960–1970.
- [73] VF Kopiev, M Yu Zaitsev, VA Kopiev, NN Ostrikov, and GA Faranosov. "Application of corona discharge acoustic characteristics to determine its properties". In: *Acoustical Physics* 62.4 (2016), pp. 429–435.
- [74] N Benard and E Moreau. "Capabilities of the dielectric barrier discharge plasma actuator for multi-frequency excitations". In: *Journal of Physics D: Applied Physics* 43.14 (2010), p. 145201.
- [75] Sammie Chan, Xin Zhang, and Steve Gabriel. "Attenuation of low-speed flow-induced cavity tones using plasma actuators". In: *AIAA journal* 45.7 (2007), pp. 1525–1538.
- [76] Yuri P Raizer. *Gas discharge physics*. Springer, 1991.
- [77] A Yu Starikovskii, AA Nikipelov, MM Nudnova, and DV Roupasov. "SDBD plasma actuator with nanosecond pulse-periodic discharge". In: *Plasma Sources Science and Technology* 18.3 (2009), p. 034015.
- [78] James M Williamson, Darryl D Trump, Peter Bletzinger, and Biswa N Ganguly. "Comparison of high-voltage ac and pulsed operation of a surface dielectric barrier discharge". In: *Journal of Physics D: Applied Physics* 39.20 (2006), p. 4400.
- [79] MR Bouazza, K Yanallah, F Pontiga, and JH Chen. "A simplified formulation of wire-plate corona discharge in air: Application to the ion wind simulation". In: *Journal of Electrostatics* 92 (2018), pp. 54–65.
- [80] Deanna Lacoste, David Pai, and Christophe Laux. "Ion wind effects in a positive DC corona discharge in atmospheric pressure air". In: *42nd AIAA Aerospace Sciences Meeting and Exhibit*. 2004, p. 354.
- [81] Matthew Rickard, Derek Dunn-Rankin, Felix Weinberg, and Fred Carleton. "Maximizing ion-driven gas flows". In: *Journal of Electrostatics* 64.6 (2006), pp. 368–376.
- [82] Thijs Defraeye and A Martynenko. "Electrohydrodynamic drying of food: New insights from conjugate modeling". In: *Journal of cleaner production* 198 (2018), pp. 269–284.
- [83] Eric Moreau, Pierre Audier, Thomas Orriere, and Nicolas Benard. "Electrohydrodynamic gas flow in a positive corona discharge". In: *Journal of Applied Physics* 125.13 (2019), p. 133303.
- [84] GW Trichel. "The mechanism of the negative point to plane corona near onset". In: *Physical Review* 54.12 (1938), p. 1078.

BIBLIOGRAPHY

- [85] R Morrow. “The theory of positive glow corona”. In: *Journal of Physics D: Applied Physics* 30.22 (1997), p. 3099.
- [86] John Sealy Townsend. *Electricity in gases*. Oxford University Press, 1915.
- [87] GF Leal Ferreira, ON Oliveira Jr, and JA Giacometti. “Point-to-plane corona: current-voltage characteristics for positive and negative polarity with evidence of an electronic component”. In: *Journal of applied physics* 59.9 (1986), pp. 3045–3049.
- [88] Xiangbo Meng, Hui Zhang, and Jingxu Jesse Zhu. “A general empirical formula of current–voltage characteristics for point-to-plane geometry corona discharges”. In: *Journal of Physics D: Applied Physics* 41.6 (2008), p. 065209.
- [89] Hakim Ait Said, Hamou Nouri, and Youcef Zebboudj. “Analysis of current-voltage characteristics in the wires-to-planes geometry during corona discharge”. In: *The European Physical Journal-Applied Physics* 67.3 (2014).
- [90] Marie-Annick Galland, Benoit Mazeaud, and Nadine Sellen. “Hybrid passive/active absorbers for flow ducts”. In: *Applied acoustics* 66.6 (2005), pp. 691–708.
- [91] Romain Boulandet, Hervé Lissek, Sami Karkar, Manuel Collet, Gaël Matten, Morvan Ouisse, and Marc Versaevel. “Duct modes damping through an adjustable electroacoustic liner under grazing incidence”. In: *Journal of Sound and Vibration* 426 (2018), pp. 19–33.
- [92] Georgy Faranosov, Oleg P Bychkov, Victor Kopiev, Vladimir A Kopiev, Ivan Moralev, and Pavel Kazansky. “Plasma-based active closed-loop control of instability waves in unexcited turbulent jet. Part 1. Free jet.” In: *25th AIAA/CEAS Aeroacoustics Conference*. 2019, p. 2557.
- [93] Nels E Jewell-Larsen, Sergey V Karpov, Igor A Krichtafovitch, Vivi Jayanty, Chih-Peng Hsu, and Alexander V Mamishev. “Modeling of corona-induced electrohydrodynamic flow with COMSOL multiphysics”. In: *Proceedings ESA Annual Meeting on Electrostatics, Minneapolis, Minnesota*. Citeseer. 2008, pp. 17–19.
- [94] Ph Béquin, V Montembault, and Ph Herzog. “Modelling of negative point-to-plane corona loudspeaker”. In: *The European Physical Journal-Applied Physics* 15.1 (2001), pp. 57–67.
- [95] Uno Ingard. “Acoustic wave generation and amplification in a plasma”. In: *Physical Review* 145.1 (1966), p. 41.
- [96] Bo Zhang, Jinliang He, and Yiming Ji. “Dependence of the average mobility of ions in air with pressure and humidity”. In: *IEEE Transactions on Dielectrics and Electrical Insulation* 24.2 (2017), pp. 923–929.
- [97] M Campbell, JA Cosgrove, CA Greated, S Jack, and D Rockliff. “Review of LDA and PIV applied to the measurement of sound and acoustic streaming”. In: *Optics & laser technology* 32.7-8 (2000), pp. 629–639.

-
- [98] Majid Nabavi, MH Kamran Siddiqui, and Javad Dargahi. "Simultaneous measurement of acoustic and streaming velocities using synchronized PIV technique". In: *Measurement Science and Technology* 18.7 (2007), p. 1811.
 - [99] Bo Zhang, Zhen Li, and Jinliang He. "A numerical model of acoustic wave caused by a single positive corona source". In: *Physics of Plasmas* 24.10 (2017), p. 103521.
 - [100] Kazimierz Adamiak and Pierre Atten. "Simulation of corona discharge in point-plane configuration". In: *Journal of electrostatics* 61.2 (2004), pp. 85–98.
 - [101] Mohammadreza Ghazanchaei, Kazimierz Adamiak, and GS Peter Castle. "Predicted flow characteristics of a wire-nonparallel plate type electrohydrodynamic gas pump using the Finite Element Method". In: *Journal of Electrostatics* 73 (2015), pp. 103–111.
 - [102] NA Kaptsov. *Elektricheskie yavleniya v gazakh i vakuume*. 1947.
 - [103] Frank William Peek. *Dielectric phenomena in high voltage engineering*. McGraw-Hill Book Company, Incorporated, 1920.
 - [104] H Nouri, N Zouzou, E Moreau, L Dascalescu, and Y Zebboudj. "Effect of relative humidity on current-voltage characteristics of an electrostatic precipitator". In: *Journal of Electrostatics* 70.1 (2012), pp. 20–24.
 - [105] Philippe Bequin and Philippe Herzog. "Model of acoustic sources related to negative point-to-plane discharges in ambient air". In: *Acta Acustica united with Acustica* 83.2 (1997), pp. 359–366.
 - [106] Richard H Small. "Closed-box loudspeaker systems-part 1: analysis". In: *Journal of the Audio Engineering Society* 20.10 (1972), pp. 798–808.
 - [107] Kaëlig Castor. "Caractérisation des sources acoustiques associées aux décharges couronnes négatives". PhD thesis. Le Mans, 2001.
 - [108] C.M. Harris. *Handbook of Acoustical Measurements and Noise Control*. McGraw-Hill handbooks. McGraw-Hill, 1991. ISBN: 9780070268685.
 - [109] Robert L Clark and Daniel G Cole. "Active damping of enclosed sound fields through direct rate feedback control". In: *The Journal of the Acoustical Society of America* 97.3 (1995), pp. 1710–1716.
 - [110] Lam Bhan and Gan Woon-Seng. "Active acoustic windows: Towards a quieter home". In: *IEEE Potentials* 35.1 (2016), pp. 11–18.
 - [111] Meysam Sharifzadeh Mirshekarloo, Chin Yaw Tan, Xiang Yu, Lei Zhang, Shuting Chen, Kui Yao, Fangsen Cui, Sai Murugan Pandit, Shyh Hao Chong, and Sze Tiong Tan. "Transparent piezoelectric film speakers for windows with active noise mitigation function". In: *Applied Acoustics* 137 (2018), pp. 90–97.
 - [112] D. Guicking and K. Karcher. "Active Impedance Control for One-Dimensional Sound". In: *Journal of Vibration, Acoustics, Stress, and Reliability in Design* 106.3 (July 1984), pp. 393–396. ISSN: 0739-3717.

BIBLIOGRAPHY

- [113] F Orduña-Bustamante and PA Nelson. “An adaptive controller for the active absorption of sound”. In: *The Journal of the Acoustical Society of America* 91.5 (1992), pp. 2740–2747.
- [114] Marc Furstoss, Denis Thenail, and Marie-Annick Galland. “Surface impedance control for sound absorption: direct and hybrid passive/active strategies”. In: *Journal of sound and vibration* 203.2 (1997), pp. 219–236.
- [115] R Boulandet and H Lissek. “Toward broadband electroacoustic resonators through optimized feedback control strategies”. In: *Journal of Sound and Vibration* 333.20 (2014), pp. 4810–4825.
- [116] Denis Thenail, Marie-Annick Galland, and Michel Sunyach. “Active enhancement of the absorbent properties of a porous material”. In: *Smart Materials and Structures* 3.1 (1994), p. 18.
- [117] Jing Yuan. “Causal impedance matching for broadband hybrid noise absorption”. In: *The Journal of the Acoustical Society of America* 113.6 (2003), pp. 3226–3232.
- [118] Pedro Cobo and Maria Cuesta. “Hybrid passive-active absorption of a microperforated panel in free field conditions”. In: *the Journal of the Acoustical Society of America* 121.6 (2007), EL251–EL255.
- [119] A Nasiri. “The Use of Plasma Actuators in Narrowband Active Noise Control”. In: *Journal of fusion energy* 30.5 (2011), pp. 394–397.
- [120] S.J. ELLIOTT. “7 - Adaptive Feedback Controllers”. In: *Signal Processing for Active Control*. Ed. by S.J. ELLIOTT. Signal Processing and its Applications. London: Academic Press, 2001, pp. 329–366. ISBN: 978-0-12-237085-4.
- [121] David A Bies, Colin H Hansen, and Carl Q Howard. *Engineering noise control*. CRC press, 2017.
- [122] *Acoustics — Determination of Sound Absorption Coefficient and Impedance in Impedance Tubes—Part 2: Transfer-Function Method*. ISO 10534-2:1998, ISO, Geneva, Switzerland, 1998.
- [123] Giorgio Palma, Huina Mao, Lorenzo Burghignoli, Peter Göransson, and Umberto Iemma. “Acoustic metamaterials in aeronautics”. In: *Applied Sciences* 8.6 (2018), p. 971.
- [124] Dah-You Maa. “Potential of microperforated panel absorber”. In: *the Journal of the Acoustical Society of America* 104.5 (1998), pp. 2861–2866.
- [125] Benjamin S Beck, Noah H Schiller, and Michael G Jones. “Impedance assessment of a dual-resonance acoustic liner”. In: *Applied Acoustics* 93 (2015), pp. 15–22.
- [126] Théo Cavalieri, Jean Boulvert, Gwénaél Gabard, Vicent Romero-Garcia, Marie Escouffaire, Josselin Regnard, and Jean-Philippe Groby. “Graded and anisotropic porous materials for broadband and angular maximal acoustic absorption”. In: *Materials* 13.20 (2020), p. 4605.

- [127] Jingwen Guo, Yi Fang, Ziyang Jiang, and Xin Zhang. “An investigation on noise attenuation by acoustic liner constructed by Helmholtz resonators with extended necks”. In: *The Journal of the Acoustical Society of America* 149.1 (2021), pp. 70–81.
- [128] Benjamin Betgen, Marie-Annick Galland, Estelle Piot, and Frank Simon. “Implementation and non-intrusive characterization of a hybrid active–passive liner with grazing flow”. In: *Applied Acoustics* 73.6-7 (2012), pp. 624–638.
- [129] Kévin Billon, Emanuele De Bono, Matthias Perez, Edouard Salze, Gaël Matten, Martin Gillet, Morvan Ouisse, Maxime Volery, Hervé Lissek, Jacky Mardjono, et al. “Experimental assessment of an active (acoustic) liner prototype in an acoustic flow duct facility”. In: *Health Monitoring of Structural and Biological Systems XV*. Vol. 11593. International Society for Optics and Photonics. 2021, p. 115932L.
- [130] BJ Tester. “The optimization of modal sound attenuation in ducts, in the absence of mean flow”. In: *Journal of Sound and Vibration* 27.4 (1973), pp. 477–513.
- [131] Zhe Zhang, Heiki Tiikoja, Luck Peerlings, and Mats Åbom. “Experimental Analysis on the ‘Exact’ Cremer Impedance in Rectangular Ducts”. In: *SAE technical paper series*. Vol. 2018. June. SAE International. 2018.
- [132] Mats Åbom. “Measurement of the scattering-matrix of acoustical two-ports”. In: *Mechanical systems and signal processing* 5.2 (1991), pp. 89–104.
- [133] Yves Aurégan, Maud Leroux, and Vincent Pagneux. “Measurement of liner impedance with flow by an inverse method”. In: *10th AIAA/CEAS Aeroacoustics Conference*. 2004, p. 2838.
- [134] BJ Tester. “The propagation and attenuation of sound in lined ducts containing uniform or “plug” flow”. In: *Journal of Sound and Vibration* 28.2 (1973), pp. 151–203.
- [135] Xinxin Guo, Maxime Volery, and Herve Lissek. “PID-like active impedance control for electroacoustic resonators to design tunable single-degree-of-freedom sound absorbers”. In: *Journal of Sound and Vibration* 525 (2022), p. 116784. ISSN: 0022-460X.
- [136] K Billon, E De Bono, M Perez, E Salze, G Matten, M Gillet, M Ouisse, M Volery, H Lissek, J Mardjono, et al. “In flow acoustic characterisation of a 2D active liner with local and non local strategies.” In: *Applied Acoustics* 191 (2022), p. 108655.
- [137] Vu Thach Pham. “Sound Field Reconstruction in a room through Sparse Recovery and its application in Room Modal Equalization”. In: (2021), p. 155.
- [138] Etienne Rivet, Andre Brandstötter, Konstantinos G Makris, Hervé Lissek, Stefan Rotter, and Romain Fleury. “Constant-pressure sound waves in non-Hermitian disordered media”. In: *Nature Physics* 14.9 (2018), pp. 942–947.
- [139] Toshiaki Hayashi, Tai Gyu Lee, Melynda Hazelwood, Elizabeth Hedrick, and Pratim Biswas. “Characterization of activated carbon fiber filters for pressure drop, submicrometer particulate collection, and mercury capture”. In: *Journal of the Air & Waste Management Association* 50.6 (2000), pp. 922–929.

Stanislav Sergeev

Rue de la Blancherie 3
1022 Chavannes-près-Renens, Switzerland

+41 78 761 26 99
stanislav.i.sergeev@gmail.com



Strengths:

Acoustical engineering, plasma technologies, signal processing, electrical engineering, technical skills



EDUCATION

PhD in Electrical Engineering, Signal Processing Laboratory LTS2

Expected 09/2022

Swiss Federal Institute of Technology Lausanne (EPFL), Switzerland - epfl.ch
Thesis: "Plasma-based electroacoustic actuator for broadband sound absorption"
Skills: acoustics, signal processing, control systems, Matlab, numerical modelling

Master of Science, Applied Mathematics and Physics

07/2018

Moscow Institute of Physics and Technology, State University (MIPT), Russia - mipt.ru
Skills: acoustics, signal processing, experiment design, Python, 3D prototyping

EXPERIENCE

Doctoral Assistant / PhD Candidate

09/2018 →

LTS2 acoustic group, Swiss Federal Institute of Technology Lausanne (EPFL) - lts2.epfl.ch

Active sound absorber: my objective was to find new approaches to reduce broadband acoustic noise in harsh environments. In a short time frame with restricted budget I developed a pioneering plasma-based sound absorption system that is more robust and reliable than existing concepts.

- Managed the international H2020-project ARTEM as EPFL representative including team meetings, reporting, and dissemination
- Identified the weaknesses of existing noise reduction methods which prevent them from being transferred to industry
- Developed a powerful yet simple analytical sound absorption model of a plasma actuator. It resulted in cost reduction of an absorber unit and an increase in its robustness
- Designed and manufactured a prototype of a sound absorber for aircraft engine as the "innovative liner concept", which proved its performance in the external tests of ARTEM H2020 project
- Patent application filed for the plasma-based active sound absorber concept

Research assistant

2016 – 2018

Schlumberger Moscow Research Center (SMR), Moscow

Characterization of sound produced by a fluid flow in rocks: Investigated the sound properties of a fluid flow in rocks. The devised theory and experimental analysis techniques are planned to be used in the field devices for production surveillance in oil and gas companies.

- Designed the laboratory setup for core acoustic analysis
- Processed, analysed, and interpreted the laboratory data in Python

Research associate student

2016

Laboratory of Pulse Plasma Systems of MIPT, Moscow

Studied the evolution of the dielectric barrier discharge and in particular the dependence of its length on the applied voltage. The obtained results contribute to the designing of alternative more efficient ignition systems in the combustion applications

ADDITIONAL EXPERIENCE

High voltage amplifier for a corona discharge

Designed a low cost audio signal amplifier for a corona discharge actuator based sound absorber in order to upscale the developed prototype and demonstrate feasibility of industrial use. Identified the optimal architecture, selected the components, and built several units. Used Simscape Simulink for simulation and KiCad for PCB layout.

Teaching

Introduced students to the standard acoustic measurement techniques (impedance in Kundt tube, reverberation time), work in acoustic facilities (anechoic, reverberant rooms), basic signal processing methods in Matlab. Assisted in the EPFL classes on Electroacoustics and Audio Engineering, supervised multiple student projects.

PUBLICATIONS AND PATENTS

Journal papers

S. Sergeev, T. Humbert, H. Lissek, and Y. Aurégan. "Corona discharge actuator as an active sound absorber under normal and oblique incidence." *Acta Acustica* 6 (2022): 5. doi.org/10.1051/aacus/2022001

S. Sergeev, H. Lissek, A. Howling, I. Furno, G. Plyushchev, and P. Leyland. "Development of a plasma electroacoustic actuator for active noise control applications." *Journal of Physics D: Applied Physics* 53, no. 49 (2020): 495202.. doi.org/10.1088/1361-6463/abafde

S. Sergeev., and D. Mikhailov. "Investigation parameters for sound induced by fluid displacement in rock samples." *Water Resources Research* 55.5 (2019): 4220-4232. doi.org/10.1029/2018WR024168

S. Sergeev, N. Ryzhikov, and D. Mikhailov. "Laboratory investigation of sound induced by gas flow in porous media." *Journal of Petroleum Science and Engineering* 172 (2019): 654-661. doi.org/10.1016/j.petrol.2018.08.018

Conference papers

S. Sergeev, and H. Lissek. "Feedback impedance control for sound absorption with corona discharge actuator." In *Euronoise 2021*. 2021

H. Lissek, X. Guo, and S. Sergeev. "On the use of Active Electroacoustic Absorbers as a perfect anechoic termination towards the low-frequency range for impedance tube applications." In *Forum Acusticum*, pp. 1297-1297. 2020.

S. Sergeev, and H. Lissek. "Corona discharge actuator for active sound absorption." In *Forum Acusticum*, pp. 1551-1555. 2020.

S. Sergeev, N. Ryzhikov, and D. Mikhailov. "Experimental study of noise induced by single-phase flow in rocks." In *Saint Petersburg 2018*, vol. 2018, no. 1, pp. 1-5. *European Association of Geoscientists & Engineers*, 2018.

Patents

S. Sergeev, H. Lissek, and M. Volery. "Plasma based noise reduction system", EPO Patent Application N° 9971154, 2021 (under review).

ACTIVITIES / LEADERSHIP

Aeromodelling club: Organised and managed MIPT radio control (RC) aeromodelling club aiming at improvement of students' engineering and technical skills and making the RC modelling more affordable with university support

MIPT Increased State Academic Scholarship for achievements in academic and extracurricular performance (top 10% out of 300+ applicants university-wide)

SKILLS

Skills and methods: control engineering (feedforward/feedback systems design, stability analysis, implementation with simulink), acoustical engineering (acoustic design and measurement, noise control, electroacoustics), numerical simulation, signal processing (audio, generic); data analysis; analytical thinking; 3D prototyping

SKILLS (CONT'D)

Software and tools: COMSOL Multiphysics, Simulink, Autodesk Inventor, KiCad, Latex, MS Office, Adobe Premiere Pro

Programming: MATLAB, Python

Languages: Russian (native), English (C1), French (B1), German (A1)

EXTRACURRICULAR

Cycling and mountain biking (check my videos here: bit.ly/2Mlyhby); tennis; studying on Coursera; Arduino; language learning; travelling.

PERSONAL INFORMATION

Citizenship: Russian; Swiss work permit (B); Birth date: 13/06/1994; Driving licence (swiss): B